EFFECT OF ANNEALING TEMPERATURE ON STRUCTURAL, MAGNETIC AND ELASTIC PROPERTIES OF MAGNESIUM NICKEL FERRITE NANOPARTICLES

Thesis submitted in fulfilment for the requirement of the Degree of

DOCTOR OF PHILOSOPHY

By

SHIV KUMAR

Enrolment Number: 186904

Department of Physics and Materials Science
Jaypee University of Information Technology
Waknaghat, District Solan, H.P., India
June 2022

Contents

DECLARATION BY THE SCHOLAR

I hereby declare that the work reported in Ph.D. thesis entitled "**EFFECT OF ANNEALING TEMPERATURE ON STRUCTURAL, MAGNETIC AND ELASTIC PROPERTIES OF MAGNESIUM NICKEL FERRITE NANOPARTICLES"** submitted at **Jaypee University of Information Technology, Waknaghat, Solan (H.P), India** is an authentic record of my work carried out under the supervision of **Dr. Ragini Raj Singh and Prof. (Dr.) P.B. Barman.** I have not submitted this work elsewhere for any other degree or diploma. I am fully responsible for the contents of my Ph.D. Thesis.

CERTIFICATE

This is to certify that the work reported in the Ph. D. thesis entitled, **'EFFECT OF ANNEALING TEMPERATURE ON STRUCTURAL, MAGNETIC AND ELASTIC PROPERTIES OF MAGNESIUM NICKEL FERRITE NANOPARTICLES'**, which is being submitted by **Mr. Shiv Kumar** for the award of the degree of Doctor of Philosophy from the Department of Physics and Materials Science by the Jaypee University of Information Technology, Waknaghat, District Solan, H.P., is the record of candidate's own work carried out by him under our supervision. other degree

or diploma.
 Dated July 26, 2026

Dr. Ragini Raj Singh

Supervisor II,

Associate Professor,

Department of Physics and

Materials Science,

Email: raginirajsingh@gmail.com,

Phone - +91 9625643296

Prof. Partha Bir Barman

Supervisor I,

Professor & Head,

Department of Physics and

Materials Science,

Email: pb.barman@juit.ac.in,

Phone - +91 9418228268

ACKNOWLEDGEMENT

"We don't meet people by accident,

they are meant to cross our path for a reason".

First and foremost I am extremely grateful to my supervisor, **Prof. (Dr.) Partha Bir Barman** for his invaluable advice, continuous support and patience during my Ph.D. study. His immense knowledge and plentiful experience have encouraged me in all the time of my academic research and daily life.

As I look back on my life, I realize that every time I thought to achieve my ultimate goal, I was being rejected from something good, I was actually being re-directed to do something better. My Ph.D. supervisor **Dr. Ragini Raj Singh**, has my heartfelt gratitude for her unwavering support and encouragement throughout my studies. She has also helped me to address various real life concerns and constraints distracting to achieve my desired goal. In my opinion she may be cited as a reference for the best research supervisor and real life conusellor. I will be eternally thankful to her for expert counsel and consistent guidance, without which this project and most desired goal would not have been completed successfully.

I would like to express my gratitude to the JUIT administration, particularly to Hon'ble Vice Chancellor JUIT, **Prof. (Dr.) Rajender Kumar Sharma**, Dean Academic & Research JUIT, **Prof. (Dr.) Ashok Kumar Gupta** for providing me with all financial and administrative support throughout the research work. I also extend my sincere thanks to my DPMC members Prof. (Dr.) Vineet Sharma, Dr. Sanjiv Kumar Tiwari and Dr. Neel Kanth for their valuable suggestions and time to time help during the entire research work. Many thanks to the faculty of Department of Physics and Matrials Science, Prof. (Dr.) Sunil Kumar Khah, Dr. Surajit Kumar Hazra and Dr. Santu Baidya for there valuble and constant support. I would like to thank Prof. (Dr.) Pankaj Sharma, NITTTR Chandigarh and Prof. (Dr.) Rajesh Kumar, CUHP Dharamshala Himachal Pradesh for their support. I would like to give special thanks to Dr. Tiratha Raj Singh to keep admiring during the research work. I would like to thank Mr. Kamlesh Mishra, Mr. Ravendra Kumar Tiwari, Mr Deepak Singh, Mr. Ghan Shyam for their assistance throughout the project.

I would like to express my heartfelt gratitude and indebtedness to my parents, **Late Shri Baldev Dutt** and **Late Smt. Susheela Devi**, my brothers and sisters, for their unwavering support and love throughout my research. I would like to express my heartfelt gratitude to my wife **Smt. Minakshi Sharma** for her unwavering support throughout the years and stood shoulder to shoulder at every moment, which has enabled me to achieve my highest goal. I also show my gratitude to my elder son **Mr. Annanay Sharma** who helped me in compiling my research work during the concluding part of research. I could never forget the encourageous and motivational support towards this research work rendered by younger son

"Don't let small minds to convince you that your dreams are too big"

(Shiv Kumar)

Date: June 26, 2022

ABSTRACT

Projected work demonstrates the aqueous synthesis of MgNi ferrite nanoparticles synthesized using sol-gel method. The nitrates of Mg, Ni and iron were used as precursors and citric acid as fuel in a water based synthesis. The ferrites were annealed at 900°C and 1100°C temperatures for achieving the finest properties from them. To know the structural, morphological, elastic and magnetic properties, the nanoparticles so prepared were characterized using X-ray diffraction technique (XRD), field emission scanning electron microscopy (FESEM), transmission electron microscope (TEM), vibrating sample magnetometer (VSM), FTIR spectroscopy and Raman spectroscopy. The results of XRD, FTIR and Raman spectroscopy patterns are indicative of formation of ferrite nanoparticles and the structural studies confirm the inverse-spinel structure with crystallite size 35-61 nm and 66-94 nm for ferrites annealed at 900°C and 1100°C respectively. The formation of spinel ferrite structure is confirmed by absorption bands corresponds to vibration of tetrahedral site-A and by absorption bands corresponds to the octahedral site-B. Crystallite size calculations were carried out using Williamson-Hall plot. Rietveld refinement was applied to assure the crystal structure and allied parameters. The magnetic analysis of the prepared samples was carried out by VSM indicates that the nanoparticles exhibited superparamagnetic behaviour having high magnetic saturation (M_S) and negligible coercivity (H_C). The estimation of elastic properties through absorption bands reveal improvement when the same precursor is annealed at higher temperatures *i.e.* 1100°C. Uniform deformation model (UDM), uniform stress deformation Stress (USDM) and uniform energy deformation model (UEDM) were first time successfully applied on the MgNi ferrite spinel nano particles SNPs. The elastic properties were studied estimating the elastic constants and compliances and applying them for three deformations. Finally a comparative study was carried out for two sets of samples, which confirms the rise in stability factor when samples annealed at higher temperature.

List of Figures

xii

List of Tables

List of Publications

1. Kumar, S., Singh, R.R. &Barman, P.B. Reitveld Refinement and Derivative Spectroscopy of Nanoparticles of Soft Ferrites (MgNiFe). J Inorg Organomet Polym 31, 528541 (2021). https://doi.org/10.1007/s10904-020-01764-7 [**I.F. 3.57**]

2. Shiv Kumar, P.B. Barman, Ragini Raj Singh, Estimation and association of structural, elastic and magnetic properties of magnesium-nickel-ferrite nanoparticles annealed at different temperatures, Materials Science and Engineering: B, Volume 272, 2021,115362,ISSN 0921-5107, https://doi.org/10.1016/j.mseb.2021.115362. [**I.F. 4.051**]

Conferences/ Seminars/ Workshops Attended

1. Third International Conference on Advanced Materials (ICAM 2019) August 09-11, 2019 at Mahatma Gandhi University, Kottayam, Kerala, India, 2019.

2. 1st National Students Conference on Spectroscopy (NSCoS 2020), jointly organized by SciRox (Science Club), Guru Nanak Dev University, Amritsar and Chemical Research Society of India from 16 - 17 October 2020.

3. National Hands-on Workshop on Characterization Techniques and Nanomaterials Applications from 20-25 January 2020, Chitkara University, Punjab.

4. Online Workshop on Rietveld Refinement Method organized by UGC-DAE Consortium for Scientific Research, Mumbai Centre in association with Indore Centre from 22-24 September 2020.

5. 1st National Students Conference on spectroscopy (NSCoS-2020) jointly organized by GNDU Amritsar and Chemical Society of India.

6. Virtual international conference on Technologies for Environmental Sustainability and Smart Agriculture organized by Centre of Excellence in Sustainable Technologies for Rural Development [CESTRD], Department of Biotechnology and Bioinformatics, Jaypee University of Information Technology during September 18 & 19, 2020.

7. International Webinar Series on Research and Technological Achievements in Biomedical and Healthcare Sector organized by Centre of Excellence in Health Care Technologies and Informatics (CEHTI) Department of Biotechnology and Bioinformatics, JUIT on August04, 2020.

8. International Webinar on Longitudinal Modeling of Alzheimer's Disease (Using Machine Learning Methods) organized by Centre of Excellence in Health Care Technologies and Informatics (CEHTI), Department of Biotechnology and Bioinformatics, JUIT on December 07, 2020.

9. Winter School on Materials Characterization Techniques, Manipal University Jaipur (MUJ), Jaipur, Rajasthan, India, December 26-27, 2020.

10. International Webinar Series on Research and Technological Achievements in Biomedical and Healthcare Sector organized by Centre of Excellence in Health Care Technologies and Informatics (CEHTI) Department of Biotechnology and Bioinformatics, JUIT on January 12, 2021.

CHAPTER 1

INTRODUCTION

The magnetic materials found tremendous applications [1–8] in every aspect of human life like medical [9], civil aviation, surface transport, telecommunication, data storage [10–13], safety services, water purification and navigation, *etc*. The term magnet is first time coined on the name of Magnesia, district of Greek country where the deposit of this magnetic ore material was found (nowadays called magnetite) [14]. The Chinese emperor Huang-Ti, 2600 BC used this material for navigation of military operations and remained very successful. The first literature on magnetism is published by W. Gilbert in 1600 BC. With the advancement in Physics and discovery of electricity, in 1825 Oersted reported that magnetic fields can be produced by means of electric current flowing in conductors. First of all, this property is known to exhibit by iron (Ferrum) and later on it is found to be exhibited by other materials like Nickel, Cobalt, *etc*., at room temperature also. These materials are generally magnetic ceramics and constitute a group of magnetic materials commonly known as ferrites. Ferrite magnetic materials are important because their properties are entirely different from the same material in bulk form. Their properties are different mainly because of particle size at nano scale.

1.1   MAGNETIC NANOPARTICLES

The nanoparticles that can be manipulated, tracked and targeted with the help of magnetic field externally are called as magnetic nanoparticles (MNPs). These MNPs have two components; first magnetic material of elements like iron, cobalt, nickel and second is chemical functionality. These nanoparticles have size in the range of 1-100 nanometres[15, 16]. For magnetic nanoparticles (MNPs) both physical and chemical properties are determined by their synthesis techniques as well as their constituent ingredients. Based on these two factors, they are classified into four categories:
i) Oxides or (Ferrites)
ii) Oxides (Ferrites) with Shell
iii) Metals
iv) Metals with Shell

1.2   FERRITES

Ferrites are the oxides of magnetic elements like Fe, Ni, Mn, *etc*. First of all magnetism is known to exhibit by iron (ferrum) and the later by other materials like Nickel, Cobalt, *etc*.,

at room temperature also. These materials are generally magnetic ceramics and constitutes a group of magnetic materials commonly known as ferrites. Ferrite nanoparticles turns to superparamagnetic as they got particle size below 128 nanometers during their synthesis process which also prevent them from self-agglomeration [16]. When individual superparamagnetic nano particles form beads in form of superparamagnetic clusters in controlled way, the magnetic moments of the magneic material abrupltly rises [17]. Ferrite particles exhibit such behaviour only by the application of external magnetic field. On switching off external magnetic field their remanent magnetization immediately fall to zero and behave like non-magnetic oxide nanoparticles. In present scenario, ferrites are used as reference materials in terms of synthesizing new materials such as hard and soft ferrites depending upon the desired applications [18]. The magnetic properties of ferrites are quantum mechanical in nature which makes them very complicated to comprehend. Ferrites possess good magnetic properties and high d.c. resistivity [19]. There are several methods of synthesizing ferrites and their properties vary with method of their synthesis. Therefore, the choice of method of synthesis predominantly constrained to one's desired output. Ferrites can be classified into three groups based on their commercial usage. Also there is a distinct crystal structure for each class.

1.2.1 GARNET-STRUCTURED SOFT FERRITES

The ferrites which on the application of even little magnetic field, get magnetized and de-magnetized without losing any energy are called as soft ferrites. In this type of ferrites, the magnetization can easily reverse without losing much energy with low hysteresis losses and low eddy current losses. This is due to low coercivity and high resistivity of soft ferrites [20–22]. They also do have high values of permeability and saturation magnetization and are non-conducting in nature.

Cobalt ferrites (CoFe $_2$O$_4$), Manganese zinc ferrite (Mn Zn ferrite) and Nickel Zinc ferrites (Ni Zn ferrite), *etc*., are examples of soft ferrites [23].

Figure 1.1: Use of ferrite cores as transformers and inductors
($https://commons.wikimedia.org/wiki/File : Ferritecores.jpg$)

Structure

Soft ferrites have garnet or spinel structure shown in figure 1.2.
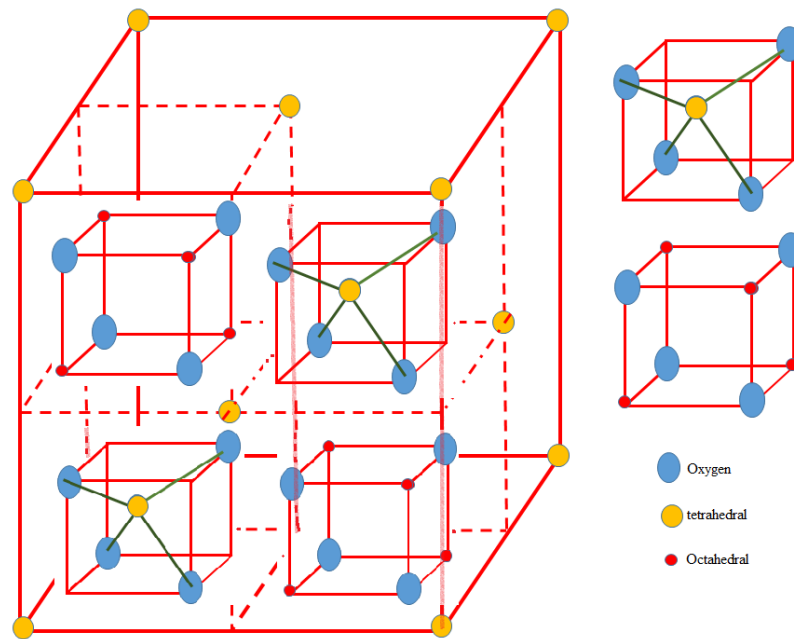
Figure 1.2: Spinel unit cell structure

Applications

These ferrites are used in transfonders or electromagnetic cores. With relatively low losses at high levels of frequencies make soft ferrites most favourable to be used in the cores of RF transformers, inductors and power supplies with switched-mode (SMPS). Cobalt ferrites ($CoFe_2O_4$) is an example of most common soft ferrites. Recently soft ferrites found applications in biomedical field using core-shell nano structures [24–26].

1.2.2   HARD FERRITES WITH MAGNETO PLUMBITE (HEXAGO-NAL) STRUCTURE

Permanent magnets which after magnetization have a strong coercivity and retentivity values are termed as hard ferrites. High coercivity means a high energy value of magneto crystalline anisotropy and is the most important property of hard ferrites. While applying low magnetic field, they do not easily magnetize or demagnetize & require high magnetic field to magnetize or demagnetize. Hexaferrites of barium and strontium ($BaO_6Fe_2O_3$, $SrO_6Fe_2O_3$) are the examples of hard ferrites [23].

Structure

The hard ferrite materials have hexagonal structure shown in figure 1.3 [27].

3
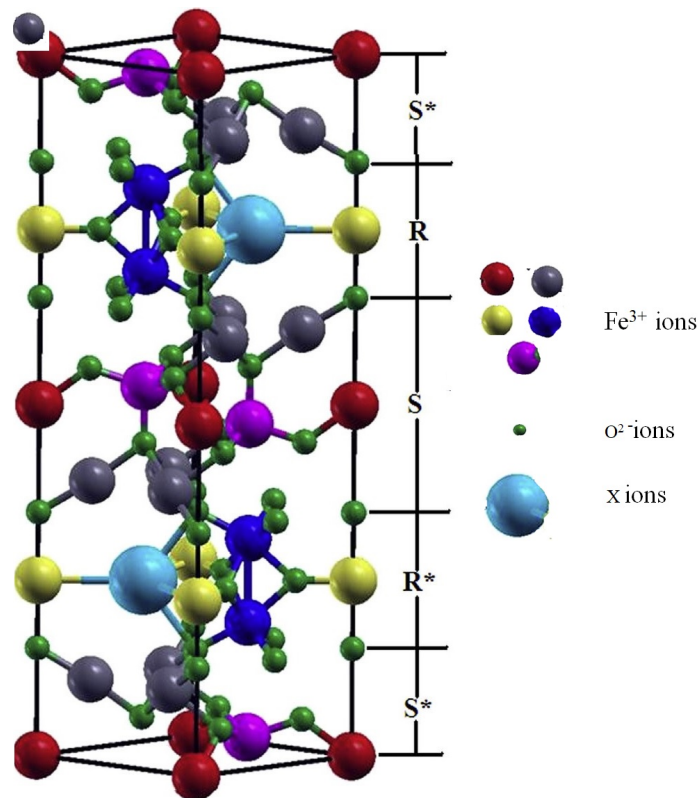
Figure 1.3: Crystal structure of M-Type Hexaferrite 3

Applications

Hard ferrites found applications in electric motors, recording media, magneto-optic media, micro-wave devices, telecommunication, electronic industry and in micro and nano-type systems such as biomarkers, bio diagnostics, and biosensors [28–33].

1.3 CRYSTAL STRUCTURE OF FERRITES

The properties of ferrites predominantly determined by the crystal structure adopted by these materials during their synthesis. The ferrites have an interlocking network of positively charged (Fe^{3+}, M^{2+}) metal ions and negatively charged divalent Oxygen (O^{2-}) ions in their crystal structure [34–36]. On the basis of their crystal structure, ferrite nanoparticles are listed in following four types. a) Spinel ferrites, b) Garnets, c) Orthoferrites and d) Hexagonal ferrites.

1.3.1 SPINEL STRUCTURE

There are two types of metallic ions in spinel ferrite nanomaterials: divalent (site-A) and trivalent (site-B). Spinel ferrite nanomaterials have the structure AB_2X_4, with A and B being

tetrahedrally and octahedrally coordinated cations respectively and X being an anion (either oxide O or fluoride F). The spinel structure is illustrated in figure 1.2.

Depending upon their chemical nature, mainly crystal field stabilization energy (CFSE), these two types of cations may arrange themselves in two ways giving rise to two types of structure known as normal spinel structure and inverse spinel structure. The ferrite nanoparticles (FNPs) with normal spinel structures, have a close-packed collection of anions. In this structure, tetrahedral A-voids and half of the octahedral B-voids are filled by the cations of site-B. Each unit cell contains eight formula units and has a composition *i.e.* $8(AB_2O_4)$ or $A_8B_{16}O_{32}$. The inverse spinel structure is mostly similar to that of spinel structure. Each unit cell has same number of formula units *i.e.* $A_8B_{16}O_{32}$. The only difference between spinel and inverse spinel structure is that half of the B type cations swap positions with A-type cations and the structural formula is therefore is written as $B(AB)O_4$. The AB ions in parentheses are assigned to octahedral sites, whereas the remaining B ions are assigned to tetrahedral sites. There are also mixed spinels, which are hybrid of the normal and inverse spinel types. This spinel structure name is provided after the name of oxide spinel magnesium aluminate ($MgAl_2O_4$) mineral. For example, materials Na_2Wo_4, $FeCr_2O_4$ and Co_3O, *etc*., also have spinel structure and the materials Pb_3O_4, FeO_4 and $NiFe_2O_4$, *etc*., are the examples of inverse spinel structure.

1.3.2 GARNET STRUCTURE
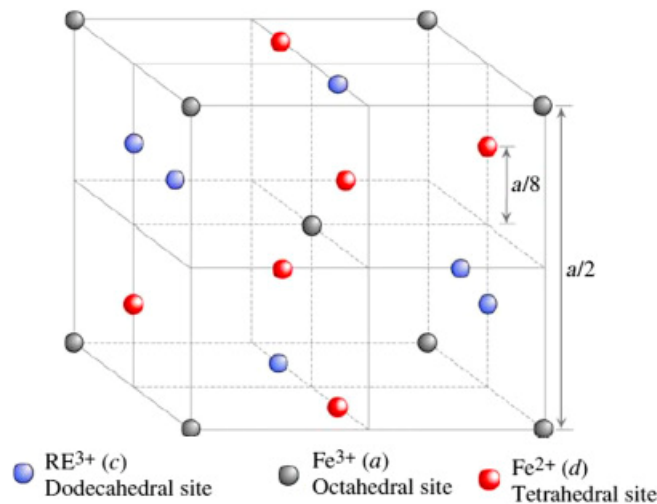
Figure 1.4: Schematic of an octant of the garnet crystal structure (lattice constant (*a*)) showing only cation positions

Garnets are nesosilicates having the general formula $A_3B_2SiO_4$. The fundamental unit of these minerals is the silicon-oxygen tetrahedron. The structure of unit cell of ortho-ferrite is shown in figure 1.4 [37]. Four negatively charged oxygen ions surround the silicon cation

5

(Si^{+4}) having positive charge and got a pyramidal shape. The structure of the Garnets is composed of either one of following type:

i. Octahedral six oxygen ions surrounding trivalent cation,

ii. Tetrahedral six oxygen ions surrounding trivalent cation,

iii. Dodecahedral polyhedral where eight oxygen atoms surrounding trivalent cation [38]. The example of garnet are $Mg_3Al_2Si_3O_{12}$, $Mn_3Al_2Si_3O_{12}$ and $Ca_3Al_2Si_3O_{12}$.

1.3.3 ORTHO-FERRITE STRUCTURE
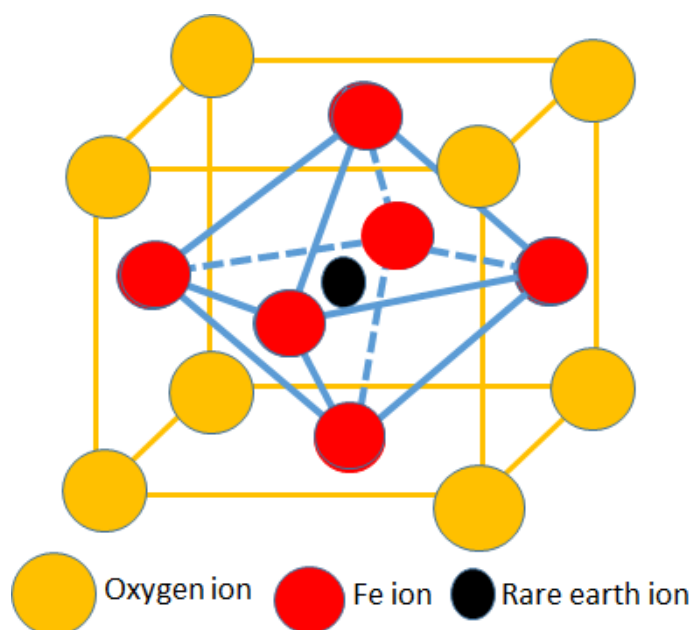
Figure 1.5: Perovskite structure (ABO_3)

Ortho-ferrite materials are nano particles with rare earth metal ion. The structure of unit cell of ortho-ferrite is shown in figure 1.5. Ortho ferrites are weakly ferromagnetic and feature an orthorhombic crystal structure with the space group **Pbnm**.

1.3.4 HEXAFERRITE STRUCTURE

The crystal structure of M-type hexaferrite is composed of a superposition of R and S blocks along the hexagonal c-axis with the structure RSSR*S*S*. R is a three oxygen layer block with composition XFe_6O_{11},where X represents Ba or Sr. S is a two oxygen layer block with composition FeO_8. The '*' means the respective block is turned 180° around the hexagonal. Hexagonal ferrites are divided into six different types *viz*: M, W, Y, X, U and Z [39]. The various six types of hexaferrite, their chemical composition and chemical formula are illstrated in table 1.1. The unit cell structure of XFe_6O_{11} is illustrated in figure 1.3.

Table 1.1: Hexaferrite types with their chemical formula, composition and stacking order

Ferrite Type	Composition	Chemical Formula	Stacking order
M	$Ba_2,Fe_{12}O_{19}$	$BaO.6Fe_2O_3$	RSR*S*
Y	$Ba_2, 2Me_2, 2Fe_{12}O_{22}$	$2BaO.2MeO. 6Fe_2O_3$	TSTST
W	$Ba_2, Me_2, 2Fe_{16}O_{27}$	$BaO.2MeO.8Fe_2O_3$	RSSR*S*S*
Z	$Ba_2, 3Me_2 2Fe_{24}O_{41}$	$3BaO.2MeO.12Fe_2O_3$	RSTSR*S*T*S*
X	$Ba_2, 2Me_2, 2Fe_{28}O_{46}$	$2BaO.2MeO.14Fe_2O_3$	RSR*S*S*
U	$Ba_2, 4Me_2, 2Fe_{36}O_{60}$	$4BaO.2MeO.18Fe_2O_3$	RSR*S*T*S*

1.4 MATERIAL SELECTION (LITERATURE SURVEY)

In case of magnesium doped zinc ferrite ($Mg_x Zn_{1-x}Fe_2O_4$), it is observed that as Mg concentration rises, ferrimagnetic behaviour rises as well [40, 41] for x < 0.5 attributed to cation distribution.

The average crystallite size and lattice constant of Mg doped Ni ferrite ($Ni_{1-x}Mg_xFe_2O_4$, x = 0, 0.1, 0.3, 0.5 & 0.7) produced by co-precipitation method and annealed at 900°C changes as the magnesium concentration increases. The saturation magnetization found to decrease in magnesium doped nickel ferrite besides increase in coercivity [42].

In case of nickel substituted $Mg_{1-x}Ni_xFe_2O_4$ (x=0, 0.1, 0.3, 0.5, 0.7 & 1.0) synthesized using sol-gel technique at 600°C annealing temperature, saturation magnetization, retentivity & coercivity found increasing with increasing nickel contents [43].

The magnesium doped nickel-cadmium ferrite nanoparticles $Mg_xNi_{0.6-x}Cd_{0.4}Fe_2O_4$ (x = 0, 0.1, 0.2, 0.3, 0.4, 0.5 & 0.6) was prepared usin co-precipitation technique without annealing. It is found that with increasing magnesium ions concentration, the values of saturation magnetization decreased while coercivity increased [44].

Nickel Zinc ferrite ($Ni_{0.58}Zn_{0.42}Fe_2O_4$) nano material synthesized using reverse micelle technique annealed at 1200°C found to have the average crystallite size of 8.4 nm. From Mossbaur spectra of these ferrite particles at room temperature, collective magnetic excitations were observed whereas when annealed (bulk) nickel zinc ferrite particles were examined with Mossbauer spectra, ferrimagnetic phase was found [45].

A well-known cobalt ferrite doped with lanthanum ions $CoLa_xFe_{2x}O_4$ (x varies from 0 to 0.2 in steps of 0.05) was synthesized [46] by co-precipitation process. XRD, VSM and impedance techniques are employed to investigate its structural, dielectric and magnetic properties.

The effect of annealing, substitutions of Mg in nickel ferrites or substitution of Ni in magnesium ferrite is visible on these properties [43, 47–50].

The effect of various factors on the properties like saturation magnetization, coercivity, high initial permeability, narrow size distribution, remanent magnetization, *etc.*, by different

methods of synthesis, doping with an element and annealing temperature in Mn-Zn ferrite is studied [51]. The XRD of these Mn-Zn ferrites nano particles confirmed cubic spinels having fd-3n phase group.

In a comparative study, Magnesium ferrite nano material are synthesised via two separate techniques *viz:* sol-gel and co-precipitation method and the difference in their major properties *viz:* structural, magnetic and electric properties were studied [52]. The crystallite size of 9 nm is obtained from the sample prepared by sol-gel method and 12 nm for sample obtained from co-precipitation method. The absorption bands (ν_1) and (ν_2) in the FTIR results for samples obtained from both the techniques are in expected range and also confirms the spinel structure and ferrimagnetic nature with a hysteresis. However, saturation magnetisation value is found to be very low for the prepared by co-precipitation as compared to saturation magnetization value sample prepared by sol-gel technique. In case of permeability, it is found decreasing when the temperature reaches 323 °K for samples prepared with sol-gel process and 363°K for samples prepared with co-precipitation technique [53].

Nickel zinc ferrite was synthesized and a series of magneto-fluorescent core-shell nanostructures was produced. Here the magnetic core is Ni-Zn and the shell is made of cadmium sulphide (CdS) quantum dots. The nanostructures Ni-Zn-ferrites@CdS were prepared in two step method, sol-gel and wet chemical. For the controlled growth of CdS QDs size, 2-mercaptoethanol was employed as stabilizing agent. In this study structural, optical and magnetic properties are studied in all three cases of Ni- Zn core , CdS and Ni-Zn/CdS nano structure [24, 54].

Calcium ferrite $(CaFe_2O_4)$ nano particles were prepared via sol-gel synthesis method taking raw materials as nitrates of calcium and iron along with citric acid chelating agent to avoid agglomeration. The sintering is done at 550°C and used for the purpose of targeted drug delivery [55].

In an interesting study, the sol-gel process was used to make yttrium oxide (Y_2O_3) nanoparticles and were analysed by XRD. The peak broadening of (Y_2O_3) is then studied in details. The study also looked at three stress models: the uniform deformation model (UDM), the uniform stress deformation model (USDM) and the uniform energy density deformation model (UEDM). The W-H graphs extracted from the data of these three models produced some astounding results. From XRD analysis dislocation density was obtained and first time Grifith model was applied to estimate microstructural parameters like internal stresses, internal strains, *etc*., to nano crystalline Y_2O_3 powder [56].

It is observed that the most wanted applications of the ferrites are biomedical applications including cancer treatment, water purification, data & energy storage and elimination of hydrogen from its most abundant source *i.e.* water. The most important application from the health point of view is synthesis of soft ferrites suitable for targeted drug delivery and elimination of oxygen and hydrogen elimination reaction from water.

The most studied soft ferrites are $NiZnFe_2O_4$, $MnZnFe_2O_4$ and $CoFe_2O_4$. The other soft ferrite $MgFe_2O_4$ and $NiFe_2O_4$ are also studied with doping by a number of transition metals and other metal ions.

From the literature survey it was observed that MgNi frrite system is least studied which lie in the category of soft ferrites. The MgNi ferrite system is not studied for its structural stability criteria along with varying stoichiometric concentrations of constituents and the effect of annealing at various temperatures. Therefore the magnesium nickel ferrite material is selected for synthesis and for structural, morphological structure and magnetic characterizations.

1.5 MAGNETISM

A well-known physical phenomenon by virtue of which certain materials exert a force (attractive or repulsive) on other specific materials only. These specific materials may be pure metals, compounds of metals or mixtures of compounds. The iron ores which are natural oxides of iron (hematite or magnetite) are first to exhibit this property. Orbiting electrons in the atoms of specific materials give rise to this magnetism. The various types of magnetism, their applications, other terms associated with the present study may be studied from literature [18, 57–79].

1.6 GENERAL PROPERTIES

The chemical compositions of all ferrites, as well as the procedures used to prepare them, influence their properties. However, by adding a small amount of impurity, differences in the distinct properties and consequently, their applications can be made to span a wide range of applications. The properties of ferrites are listed below and represented in figure 1.6 [80–84].

1. They have a high dielectric constant, which ranges from thousands to tens of thousands at low frequencies and between 10 and 20 at microwave frequencies. This is owing to the oxygen ions' tightly packed shape.

2. The majority of them are black or grey in colour. The nearly equal energies of the 3d and 4s states are responsible for this. This is also due to the fact that in the case of ferrite crystal structure, absorption occurs solely in the visible range, rendering ferrites black.

3. Since they lose oxygen at high temperatures, their melting points are difficult to determine. Van Arkel, on the other hand, used an oxyhydrogen flame to determine their melting points.

4. Ferrites are normally insulators. However, when electric field is applied they behave as semiconductors.

5. Ferrites contain oxide ions which leads to close-packed spatial formation and having strong ionic bond makes them very hard and brittle in nature.

6. Ferrites have gained such high importance only due to their following specific magnetic properties.

i. Ferrites have magnetic anisotropy *i.e.* ferrites get completely magnetized along their preferred axis of magnetization when they are placed in a magnetic field.

ii. Ferrites have two types of hysteresis loops which classify them in two types:

a. Some ferrites have very thin Hysteresis loop having small value of coercivity and large value of saturation magnetization and are paramagnetic in nature.

b. Some ferrites, such as rare earth metal ferrites, feature square hysteresis loops with high coercivity and low saturation magnetization value. These are hard to magnetize or demagnetize and therefore called hard ferrites.
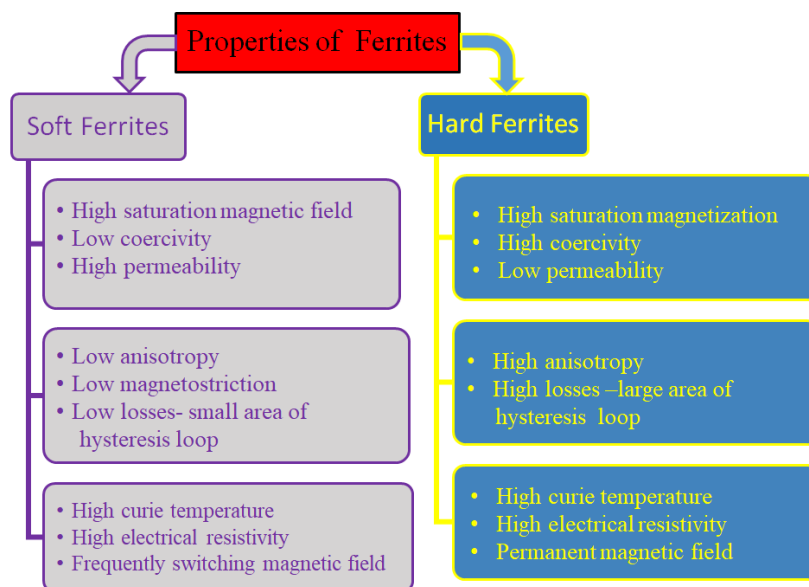
Figure 1.6: Properties of soft and hard ferrites

1.7   SYNTHESIS METHODS

Ferrite nanoparticles (FNPs) are prepared via a number of synthesis methods depending upon material of choice and purpose with desired area of utility [85–94].

Technique	Temperature	Advantages	Disadvantages	Reference
Co-precipitation	20-150°C	Large Scale Production, Traditional method	No control on Size of Particle, Broad Size, Poor Crystallite	[85]
Laser Ablation	-	Purification Not Required	Prolonged Time	[86]
Solvothermal	150-220°C	Simple, Control Over Size	Prolonged Time	[87]
Sonochemical	20-50°C	Quick Processing	Poor Shape Control	[88]
Micro Emulsion	20-80°C	Narrow Size, Desirable Size, Low Temperature	Low Yield , Long Time, Extra Solvent Material Required	[89]
Hydrothermal	100-220°C	Cost Effective Optimum Yield. Scalable	High Pressure and Prolonged Reaction Time	[90]
Sol-Gel	25-200°C	Size and Shape Control	Long Processing Time, Medium Yield	[91, 92]
Ball Milling	-	Chemical Reaction and Heating not Required	No control over Crystallite Size and Shape	[93]
Chemical Vapour Deposition	Arbitrary	Better Growth Rate, Controlled Size, High crystallite	Complex Process, Toxic gases released	[94]
Spray Pyrolysis	-	Narrow Size ,	High Temperature	[95]

Figure 1.7: Properties of soft and hard ferrites

Till date there is no universal method of synthesis of ferrites. The shape, size, morphology and even stability and purity of ferrites depends on their synthesis methods. Ferrites can be prepared by two approaches; first one is known as bottom-up approach where the ions are made to combine together chemically to form the nanoparticles and second approach is called top-down involving pulverization of materials to form nanoparticles. In the first category *i.e.* bottom up category, the synthesis processes are co-precipitation, hydrothermal, solvothermal, sol-gel, sonochemical, vapour deposition, thermal decomposition, microwave-assisted, flame spray pyrolysis, microemulsion and polyol techniques, *etc,*. Out of these processes the most popular processes are co-precipitation, sol-gel, vapour deposition and flame spray pyrolysis. Mechanical milling processes and pulsed laser ablation are notable examples of the second type or top-down synthesis techniques. In the present day, sonochemical, microwave irradiation and polyol methods are used to make a variety of SNPs. Various synthesis methods are now being employed for the creation of ferrite materials, as each of these synthesis methods has its own advantages and disadvantages are shown in figure 1.7 [95–105].

1.8 APPLICATIONS

In the last 10 years, the ferrites found utmost important applications in biotechnology mainly for targeted drug delivery for the treatment of cancer disease. Ferrites are also used in various electronic circuits *viz:* radio, TVs and mobiles in the form of inductors, systems operating on high-frequencies, in power devices and even in electromagnetic interference suppression [40, 106–115]. The major application areas of ferrite are given in figure 1.8 [3, 7, 8, 24, 29, 31, 33, 54, 73, 80, 96, 116–152].

Figure 1.8: Applications of Ferrite nanoparticles

1.9 MOTIVATION OF THE RESEARCH

Motivation of the present work is to use ferrites for targeted drug delivery system. To fulfill this, the ferrites should be following criteria:

(i) superparamagnetic in nature

(ii) in nano range and

(iii) elastically stable material to counter the deforming agents such as various chemicals and pH environments, thermal and EM radiations.

1.10 OBJECTIVES OF THE THESIS

Based on research gaps and motivation following objectives have been chalked out:

Objective 1: MgNi ferrite Nanoparticles Synthesis, Structural and Magnetic Studies at 900°C Annealing Temperature.

Objective 2: MgNi ferrite Nanoparticles Synthesis, Structural and Magnetic Studies at 1100°C Annealing Temperature.

Objective 3: Comparison of Structural, Magnetic and Elastic Properties of MgNi Ferrite Nanoparticles annealed at 900°C & 1100°C Temperatures. The synthesis of SNPs was elaborated and discussed in next chapter. In order to analyse the synthesized ferrite nanoparticles, several characterization tools and techniques have been used to know the properties and discussed in the next chapter. Subsequently in coming chapters each and every objective will be presented and discussed in thoroughly.

1.11 OUTLINE OF THESIS

Chapter 1 In this chapter general introduction of ferrites along with history of magnetism is described. Classification of ferrites on the basis of crystal structures, their magnetic properties, properties of spinel ferrites, various synthesis techniques and their detailed literature survey was carried out.

Chapter 2 This chapter includes experimental techniques used for the preparation of($Mg_xNi_{(1-x)}Fe_2O_4$) ferrites nanoparticles. Various characterization techniques that are used to estimate the structural and magnetic properties are also discussed here.

Chapter 3 This chapter describes Synthesis and characterization of ($Mg_xNi_{(1-x)}Fe_2O_4$) at x= 0.1875, 0.4375, & 0.8125 nanoparticles synthesized using sol-gel technique annealed at temperature 900°C. It also include measurement of structural, elemental and magnetic properties carried out by XRD, FTIR FESEM, HRTEM, RAMAN, EDX and VSM. The effect of Mg concentration on the structural and magnetic properties of MgNi ferrites, has also been discussed.

Chapter 4 This chapter describes Synthesis and characterization of ($Mg_xNi_{(1-x)}Fe_2O_4$) at x= 0.1875, 0.4375, & 0.8125 nanoparticles synthesized using sol-gel technique annealed at temperature 1100°C. Same characterizations were carried out (mentioned in chapter 3) for the samples annealed at 1100°C.

Chapter 5   This chapter include comparison of structural, elastic and magnetic properties of ($Mg_xNi_{(1-x)}Fe_2O_4$) nanoparticles at x= 0.1875, 0.4375, & 0.8125 synthesized via sol-gel technique annealed at $900°C$ and $1100°C$ temperatures. The properties which are compared include measurement of structural, elemental and magnetic properties carried out by XRD, FTIR FESEM, HRTEM, RAMAN, EDX and VSM. The structure parameters are refined with Rietveld refinement and the structural stability based elastic coefficients so calculated are also compared for the synthesized nanoparticles.

Chapter 6   Finally this chapter summarizes and concludes the work, as well as making recommendations for future research.

CHAPTER 2

SYNTHESIS AND CHARACTERIZATION TECHNIQUES

2.1 OVERVIEW

Materials scientist has made great efforts towards the development of new and convenient techniques for synthesis of ferrites nanoparticles. A number of methods comprising both physical as well as chemical methods has been used to synthesis the ferrites nanoparticles. Auto combustion technique [152], ceramic technique [153], polyol technique [154,155], co-precipitation technique [156], hydrothermal technique [157–159], sol-gel technique [160, 161], reverse micelle technique [45], mechanically alloyed technique, *etc.*, are some of the most commonly used methods to prepare the ferrite nanoparticles [162]. Among the different techniques, sol-gel method is the most important technique for preparing ferrites nanoparticles because of their important features such as precursors materials dissolve at atomic or molecular level, low temperature synthesis process, homogeneous reaction distribution, excellent composition control, high purity product formation, better size and control over morphology, cost economy and optimum results in comparison to other complex techniques [163]. This chapter covers the synthesis and experimental methodologies used to prepare magnesium nickel ferrite $Mg_xNi_{1-x}Fe_2O_4$ nanoparticles, x is a atomic fraction o < x < 1 and in present study x= 0.1875, 0.4375 & 0.8125. The preparation of $Mg_xNi_{1-x}Fe_2O_4$ ferrite nanoparticles (FNPs) at two distinct annealing temperatures of 900°C and 1100°C is detailed in this chapter using the sol-gel process. X-ray diffraction (XRD), Field Emission Scanning Electron Microscopy (FESEM), High Resolution Transmission Electron Microscopy (HRTEM), Fourier Transform Infrared Spectroscopy (FTIR) and Raman spectroscopy are used to investigate various properties of the ferrite nano particles. Structural, morphological and magnetic properties of the prepared samples are also investigated. The energy gap of the samples is determined using Ultra Violet Visual Spectroscopy (UV-Vis). The magnetic parameters are determined using Vibrating Sample Magnetometry (VSM). Various formulae used to obtain different parameters required to describe their structural, morphological, elastic and magnetic properties of these synthesized particles are also discussed in this chapter.

2.2   SYNTHESIS

Synthesis of ($Mg_xNi_{1-x}Fe_2O_4$) nanoparticles x = 0.1875, 0.4375 & 0.8125 by sol-gel technique was carried out followed by annealing at 900°C and 1100°C temperatures.

2.2.1   CHEMICAL REQUIRED FOR SYNTHESIS

For the synthesis of $Mg_xNi_{1-x}Fe_2O_4$ nanoparticles, the required chemicals are of Merck 99.9 percent purity. The chemicals are nickel nitrate hexahydrate ($Ni(NO_3)_2.6H_2)O$, Magnesium nitrate hexahydrate ($Mg(NO_3)_2.6H_2O$) and ferric nitrate nanohydrate ($Fe(NO_3)_3.9H_2O$). The citric acid monohydrate $C_6H_8O_7.H_2O$ (Merck, 99.9 percent) was used as a complexing agent. Aqueous ammonia (25 percent) AR-grade (Merck, 99.9 percent) is used to control pH of the solution at desired level of 7.0.

2.2.2   PROCEDURE

Sol is a dispersion or suspension of solid particles in liquid, whereas gel is a continuous three-dimensional network in which solid particles and liquid are disseminated in each other in the sol-gel process [95]. In this process molecular precursors were dissolved in solvent to form sol or colloidal suspension. Thereafter, 3D liquid fill the solid network formed by linkage of colloidal nanoparticles with one another. The formation of gel from sol is possible by virtue of changing the pH of the reaction solution. The various steps included
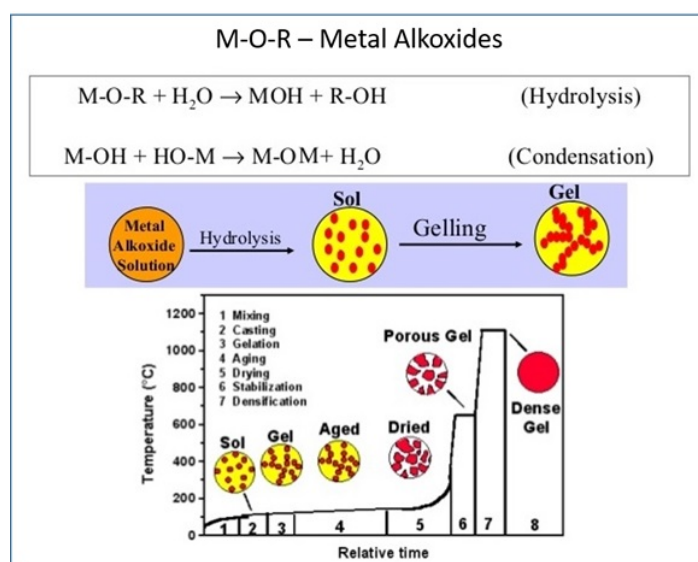
Figure 2.1: Steps included in sol-gel process
(http://www.slideshare.net/tango67/nanomateriales-17839251

in sol-gel process for the formation of nanoparticles are shown in figure 2.1. The two main reaction processes involved in sol-gel process are hydrolysis and condensation. The gel is

dried through evaporation process which creates high density xerogel by collapsing of gel network. Further, high density xerogel is heated at high temperature to remove organic or inorganic component to form the desired nanoparticle material [95].

The Optimized synthesis parameters for the synthesis of MgNi ferrite nanoparticles (SNPs) are given in the figure 2.2. The selected chemicals nickel nitrate hexahydrate ($Ni(NO_3)_2.6H_2O$),
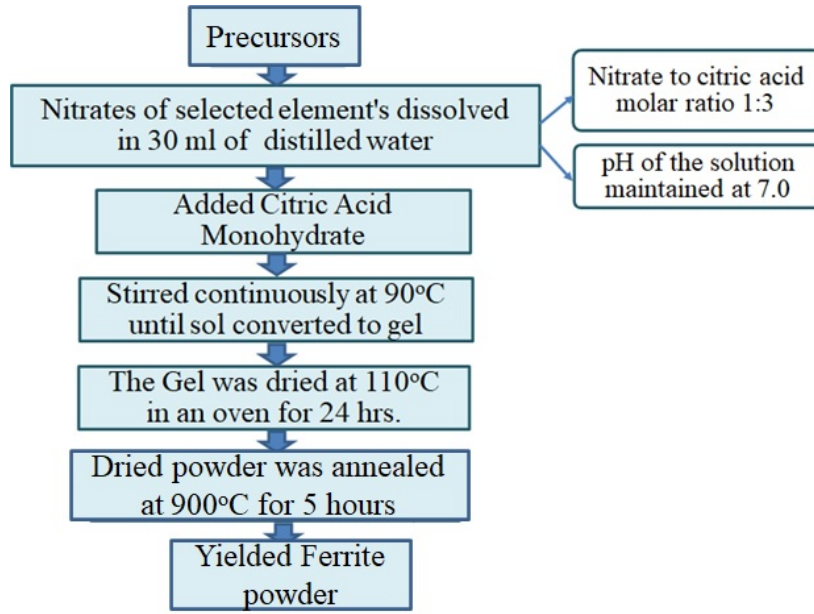
Figure 2.2: Process flow for synthesis of $Mg_xNi_{1-x}Fe_2O_4$ ferrites by sol-gel method

Magnesium nitrate hexahydrate ($Mg(NO_3)_2.6H_2O$) and ferric nitrate nanohydrate ($Fe(NO_3)_3.9H_2O$) were first weighed in stoichiometric amounts and then dissolved in distilled water by continuous stirring for 30 minutes. The citric acid monohydrate $C_6H_8O_7.H_2O$ in appropriate amount dissolved in distilled water and stirred for 30 minute on magnetic stirrer. The two solutions then mixed and immediately aqueous ammonia added drop wise to the mixed solution maintaining pH value of 7.0. The solution was then allowed to swirl continuously for six hours at a temperature of 80°C to 90°C until it turned into a yellowish gel. The gel was placed in an oven to dry for 24 hours maintaining temperature at 110°C. The dried material then mashed to powder using garnet mortar. The desired $Mg_xNi_{1-x}Fe_2O_4$ nanoparticles were then obtained by annealing the powder at 900°C and 1100°C for five hours. The schematic of sol-gel technique is shown in figure 2.3. The following chemical reaction takes place in the synthesis process

$$xMg(NO_3)_2.6H_2O + (1-x)(Ni(NO_3)_2.6H_2O) + 2Fe(NO_3)_3.9H_2O$$
$$+ 9C_6H_8O_7.H_2O + NH_3 \xrightarrow[heat]{\triangle}$$
$$Mg_xNi_{1-x}Fe_2O_4 + 4N_2 \uparrow +54CO_2 \uparrow +49H_2 \uparrow +8H_2O$$
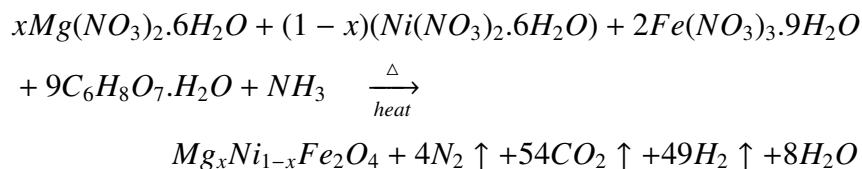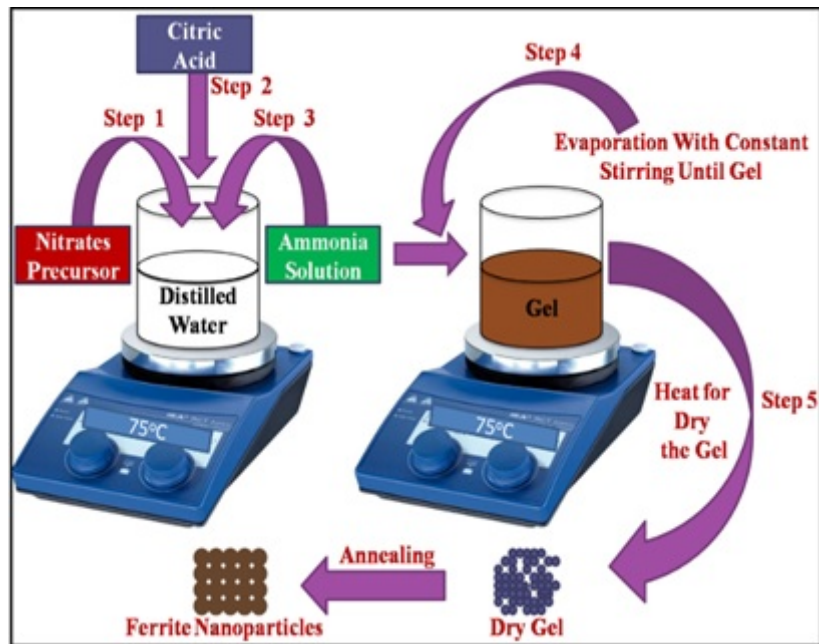
Figure 2.3: Schematic diagram of sol-gel technique

2.3 CHARACTERIZATION TECHNIQUES

The nanoparticle so obtained were characterized using the following techniques:

1. X-Ray Diffraction (XRD)

2. Field Emission Scanning Electron Microscope (FESEM)

3. Energy Dispersive X-Ray Spectroscopy (EDX)

4. High Resolution Transmission Electron Microscopy (HRTEM)

5. Raman Spectroscopy

6. Vibrating Sample Magnetometer (VSM)

7. Fourier Transform Infrared Spectroscopy (FTIR)

8. UV-VIS Spectroscopy

9. Photoluminscence Spectroscopy

2.4 VARIOUS PARAMETERS

2.4.1 THE SCHERERS FORMULA FOR CALCULATING CRYSTAL- LITE SIZE (D)

$$D = A\lambda/\beta\cos\theta \qquad (2.1)$$

where Scherer's constant A = 0.9 for cubic system. The wavelength (λ) of Cuk_α^{-1} X-rays is 1.5402 Å, β is full width at half maximum (FWHM) of a particular peak formed by XRD data at a particular Braggs angle θ [164].

2.4.2 LATTICE PARAMETER AND LATTICE SPACING

The lattice parameters such as lattice constant (a) and lattice spacing (d) of synthesized nanoparticles using miller indices of the plane namely < hkl > are determined by using following relations [164–167].

$$2d\sin\theta = n\lambda \qquad (2.2)$$

$$a = d(h^2 + k^2 + l^2)^{1/2} \qquad (2.3)$$

Strain Stocks-Wilson relation to estimate strain (ϵ) is given by

$$\epsilon = \beta/4\tan\theta \qquad (2.4)$$

where n = 1,2,3,4...... is the order of diffraction peak and β is full width at half maxima (FWHM) of the diffraction peak at angle θ.

2.4.3 CRYSTALLITE SIZE (D)

Williamson-Hall (W-H) relation to calculate crystallite size (D) at different types of strains (ϵ) present in synthesized nanoparticles [167] is given by

$$\beta\cos\theta = A\lambda/D + 4\epsilon\sin\theta \qquad (2.5)$$

where Scherers constant A = 0.9 for cubic system. The wavelength (λ) of Cuk_α^{-1} X-rays is 1.5402 Å, β is full width at half maximum (FWHM) of a particular peak formed by XRD data at a specific Bragg's angle θ [164].

2.4.4 THEORETICAL X-RAY DENSITY (ρ_x)

The theoretical x-ray density (ρ_x) was calculated using the relation[166, 167]

$$\rho_x = \frac{ZM}{N_\alpha V} \qquad (2.6)$$

where Z = 8 molecules per unit cell with volume V, M, and N_α are the molecular weight of one unit formula and Avogadro Number respectively [167].

2.4.5 BULK DENSITY (ρ)

The bulk density (ρ) is determined by the relation [166, 167]

$$\rho = \frac{M_{Sample}}{V_{Sample}} \qquad (2.7)$$

where M_{Sample} is mass and V_{Sample} is the volume of the sample taken for the measurement.

2.4.6 PORE FRACTION (f)

Pore fraction or porosity (f) is calculated by equation[164, 167]

$$f = \frac{(\rho_x - \rho)}{\rho} \qquad (2.8)$$

where ρ is bulk density and ρ_x is theoretical X-ray density.

2.4.7 DISLOCATION DENSITY (δ)

For spinel ferrites, the dislocation density (δ) can be calculated as [166]

$$\delta = \frac{15\epsilon_{RMS}}{a.D} \qquad (2.9)$$

where ϵ_{RMS} denotes the lattice strain, D is the average crystallite size, and *(a)* is the lattice parameter determined from XRD data. The specific surface area (S) can be calculated using the following formula [164–167].

$$S = \frac{6 \times 10^6}{\rho_x . D} \qquad (2.10)$$

where D is the particle's diameter in nm and ρ_x is the particle's density in Kg/m^3 [164–167].

2.4.8 MAGNETO CRYSTALLINE ANISOTROPY (K)

The magneto crystalline anisotropy energy constant (K) is calculated using relation [167, 168]

$$H_c = 0.96K/M_S \tag{2.11}$$

where H_C and M_S denote the samples' coercivity and saturation magnetization, respectively. The experimental magnetic moment M_μ of all prepared samples was determined using formula

$$M_\mu = \left(\frac{M_w \times M_s}{5585} \right) \tag{2.12}$$

where M_w and M_s are the molecular weight and saturation magnetization. Neels two sub lattices model of ferrimagnetism gives the theoretical total magnetic moments (N_μ) per formula unit cell and was estimated using relation

$$N_\mu = M(B) - M(A) \tag{2.13}$$

where M(A) is the sub lattice moments of site-A and M(B) is that of site-B.

2.4.9 CATION DISTRIBUTION FORMULAE

The various formulae used to estimate the cation and ionic distribution are as follows [112, 166, 167, 169]:

Proposed Cation Distribution Formula is given by

$$\left[Fe^{3+} \right]^A \left[Mg_x^{2+} Ni_{1-x}^{2+} Fe^{3+} \right]^B O_4^{2-} \tag{2.14}$$

Theoretical value of Ionic radius(r_A) of tetrahedral site-A

is given by

$$r_A = C_{A(Fe)} r^{(Fe^{3+})} \tag{2.15}$$

Theoretical value of Ionic radius (r_B) of octahedral site-B

is given by

$$r_B = \frac{1}{2} \left[C_{A(Mg)} r^{(Mg^{2+})} + C_{B(Ni)} r(Ni^{2+}) + C_{B(Fe)} r^{(Fe^{3+})} \right] \tag{2.16}$$

where $C_{A(Fe)}$, r $^{(Fe3+)}$, $C_{B(Mg)}$, r $^{(Mg2+)}$, $C_{B(Ni)}$, r $^{(Ni2+)}$, $C_{B(Fe)}$ and r $^{(Fe3+)}$ are the concentration and concerned ionic radii of Fe^{3+} ions at site-A and Mg^{2+}, Ni^{2+}, Fe^{3+} ions at site-A respectively.

2.4.10   OXYGEN PARAMETER (u)

The positional parameter (u) of oxygen ion can be estimated for theoretical as well as experimental values [55, 112, 167]

$$u = \left[(r_A + r_B) \frac{1}{a\sqrt{3}} + \frac{1}{4} \right] \qquad (2.17)$$

2.4.11   INVERSION FACTOR (δ)

Another parameter called inversion parameter (δ) also known as deviation from ideal oxygen positional parameter (u) was determined using relation [55, 112, 167]

$$\delta = u - u_{ideal} \qquad (2.18)$$

where u_{ideal} is the ideal oxygen positional parameters 0.375 Å.

2.4.12   THEORETICAL LATTICE PARAMETER (a)

The theoretical value of the lattice parameter (a) [55, 112] was estimated using the values of ionic radii of tetrahedral (r_A) and octahedral sites (r_B).

$$a = \frac{8}{3\sqrt{3}} [(r_A + R_0) + \sqrt{3}(r_A + R_0)] \qquad (2.19)$$

where R_0 is the ionic radius of O^{2-} and R_0=1.38 Å [170].

2.4.13   MICROSTRUCTURAL PARAMETERS

Formulae for Full width at half maximum (β_D), crystallite strain (ϵ) and average crystallite size (D) are calculated using Scherer's formula given by [55, 112, 167]

$$\beta_D = \frac{A\lambda}{D cos\theta} \qquad (2.20)$$

where for spinel cubic system the shape factor (A) has value of 0.9 [171]. λ is the wavelength of CuK_α^{-1} X-ray radiations, D is the crystallite size and β is the FWHM in radians at half maximum of the diffraction peak at diffraction angle 2θ.

$$\beta = \beta_D + \beta_\epsilon \qquad (2.21)$$

$$\beta_\epsilon = 4\epsilon \tan\theta \qquad (2.22)$$

$$\beta \cos \theta = \frac{A\lambda}{D} + 4\epsilon \sin \theta \tag{2.23}$$

where β_D and β_ϵ are the contributions of size and strain respectively in β. The relation (2.23) is a straight line of the form y= mx + c, where y is $\beta \cos \theta$ and x is $4 \sin \theta$ and the plot is known as the Williamson-Hall plot [8, 43]. The crystallite strain (ϵ) is determined by the slope of the plot and the crystallite size (D) is determined by the intercept.

2.4.14   FORCE CONSTANT

The elastic constants were determined using FTIR spectroscopic methods [9,45,47]. Nanoparticles are spinel cubic crystalline in nature, and is classified into three classes to solve the vibrational problem: continuously bonded, discontinuously bonded, and intermediate [46]. The ions are bonded to their nearest neighbour ions by forces such as ionic, covalent or vander Waals forces. Further the frequency distribution of vibrations are given by Debye or Bornvon Karman treatment of the problem, which is classical mechanical in nature. Based on the geographical configuration of nearest neighbour oxygen atoms, metal ions are positioned in two distinct positions: octahedral (o) and tetrahedral (τ). The lattice disorder would destroy the vibrations' translational invariance, resulting in a spread of infrared-active frequencies, might be caused via isotopic substitution. Unless the mode is solely determined by symmetry requirements, the exact form of normal vibrations is determined by the "potential energy field." Internally, three possible frequencies are inactive, one of which is the zero frequency translation among eight possible frequencies [9]. The internally-inactive vibrations take place because the location of the Fe ions on centers of symmetry and the equivalence of the MO_4 groups. Each oxide-ion is bonded to one tetrahedral ion and three octahedral ions. In normal spinel structure, three octahedral bonds lie along the coordinate axes and provide an isotropic force field. This field would permit oxide-ions to oscillate in any direction with a constant frequency, in the absence of the tetrahedral bonds. On increasing the frequency of vibrations along the τ-o axis (ν_l), vibrations at right angles (ν_s) will change frequency to some extent (when minute bending force constants are assumed). Two low-frequency active modes, (ν_3) and (ν_4) engross metal-ion oscillations in isotropic force fields in octahedral and tetrahedral settings respectively. Because only two infrared bands were accessible in the covered spectral range, the energy field can be estimated using only two potential constants. The classification of these constants with accurate bonds necessitates, definite assumptions for simplification is made (bending force constants must be ignored in the following treatment). This approximation is probably closer in the ionic situation than it is in the molecular case. To derive force constant of tetrahedral site-A (K_τ) and octahedral site-B (K_o), we must apply the equations given below denoting the force constants associated with unit displacement of the τ-O and o-O bonds.

There are two approaches to calculate the force constant. In approach I, the following relationships are employed to compute K_τ and K_o (suggested by Waldron) [9]:

$$K_\tau = 7.62 \times M_1 \times v_\tau^2 \times 10^{-7} \tag{2.24}$$

$$K_o = 7.62 \times M_2 \times v_o^2 \times 10^{-7} \tag{2.25}$$

where M_1, M_2 are the molecular weights of ions at site-A and site-B respectively and v_τ, v_o are corresponding absorption frequencies.

In approach II from classical mechanics we know that for a vibrating object angular frequency (ω) is given by the relation

$$\omega = \sqrt{\frac{K}{\mu}} \tag{2.26}$$

where $\omega = 2\pi vc$, c is the velocity of light, v is the wave number, K is force constant and μ is reduced mass.

By applying this concept in the present case, the equivalent force constants for the two absorption frequencies at site-A and site-B are as follows:

$$K_\tau = 4\pi c^2 v_\tau^2 \mu_\tau \tag{2.27}$$

$$K_o = 4\pi c^2 v_o^2 \mu_o \tag{2.28}$$

The reduced masses of ions at site-A and site-B are μ_τ and μ_o, respectively. The cation distribution formula was used to determine both μ_τ and μ_o respectively. In the present study, both the above methods are used to investigate the elastic properties of the synthesized SNPs annealed at 900°C. However, the results from the two methods are nearly of the same order and the more accurate results are obtained with the second formula [112, 167]. Therefore the second formula *i.e.* equation 2.27 & equation 2.28 are employed in the present research work to carry out elastic properties.

2.4.15   ELASTIC CONSTANTS AND ELASTIC COMPLIANCES

To know the structural stability or stiffness of crystalline materials, elastic constants are essential parameters and we apply Hook's law directly to the single crystal in the form of stress-strain relation given by

$$\sigma_{ij} = C_{ij}\epsilon_{ij} \tag{2.29}$$

where σ_{ij} is component of stress, ϵ_{ij} is component of strain and C_{ij} represents the elastic constants in ij plane. In fact, the cubical crystals are anisotropic in nature and have different values of C_{ij} in different crystallographic directions. In actual practice there are six types of stresses applied on the crystalline materials *viz:* normal stress, shear stress, thermal stress, *etc.* This gives rise to six types of strains *i.e.* normal strain, shearing strain, *etc.*, to form a stiffness of the order of 6x6 matrix. Thus there are a total of 36 stiffness constants C_{ij}. The elastic flexibility matrix S_{ij} is the inverse matrix of the elastic stiffness C_{ij}

$$S_{ij} = C_{ij}^{-1} \tag{2.30}$$

In case of cubical crystals due to 3-D symmetry only three elastic stiffness constants are necessary *viz:* C_{11}, C_{12} and C_{44} and three elastic compliances S_{11}, S_{12} and S_{44} [56, 167].

The following equations are used to compute the elastic stiffness constants C_{11}, C_{12}, and C_{44}

$$Stiffness\ constant \qquad (C_{11}) = \frac{K_{av}}{a_0} \tag{2.31}$$

where $K_{av} = (K_o + K_\tau)/2$ is the simple average of the K_τ and K_o force constants at the tetrahedral and octahedral sites respectively with a_0 being the lattice constant.

$$Stiffness\ constant \qquad (C_{12}) = C_{11}\frac{\sigma}{1-\sigma} \tag{2.32}$$

$$Stiffness\ constant \qquad (C_{44}) = A\frac{C_{11}-C_{12}}{2} \tag{2.33}$$

here A is anisotropic constant of spinel cubic structure having the value of 0.9 and σ denotes the poison's ratio given by

$$\sigma = 0.324(1 - 1.043f) \tag{2.34}$$

where f is pore fraction.

The elastic compliances are denoted as S_{11}, S_{12} & S_{44} and are formulated from corresponding elastic constants C_{11}, C_{12} & C_{44} and given by the following relations [172, 173]:

$$S_{11} = \frac{C_{11} + C_{12}}{(C_{11} + 2C_{12})(C_{11} - C_{12})} \tag{2.35}$$

$$S_{12} = \frac{-C_{12}}{(C_{11} + 2C_{12})(C_{11} - C_{12})} \tag{2.36}$$

$$S_{44} = \frac{1}{C_{44}} \tag{2.37}$$

2.4.16 ELASTIC MODULII

The estimation of other elastic moduli is done using the following relations [56, 80, 167]

Youngs modulus (Y)

$$(Y) = \frac{(C_{11} - C_{12})(C_{11} + 2C_{12})}{(C_{11} + C_{12})} \tag{2.38}$$

Modulus of rigidity (G)

$$(G) = \frac{Y}{2(\sigma + 1)} \tag{2.39}$$

Bulk modulus (B)

$$(B) = \frac{1}{3}(C_{11} + C_{12}) \tag{2.40}$$

WAVE VELOCITY

The following equations are used to estimate the values of longitudinal wave velocity V_L and transverse wave velocity V_τ

Longitudinal wave velocity (V_L) is given by

$$(V_L) = \sqrt{\frac{C_{11}}{\rho_x}} \tag{2.41}$$

Transverse (shear) wave velocity ($V\tau$) is given by

$$(V_\tau) = \sqrt{\frac{G_0}{\rho_x}} \tag{2.42}$$

G_0 shown in the above equation is the modulus of rigidity calculated at zero pore fraction [9, 42] and is given by

$$\frac{1}{G_0} = \frac{1}{G}\left[1 - \frac{15f(1 - \sigma)}{7 - 5\sigma}\right] \tag{2.43}$$

DEBYE TEMPERATURE (θ_D)

By Anderson relation [174]

$$\theta_D = V_m \frac{h}{K_B}\left(\frac{3N_\alpha}{4\pi V_A}\right) \tag{2.44}$$

V_A is denoted as the atomic volume and is expressed as

$$V_A = (M/\rho_x)/q \tag{2.45}$$

and V_m is the mean velocity calculated using the formula

$$(V_m) = \left[\frac{1}{3}\left(\frac{2}{V_L^3} + \frac{1}{V_\tau^3}\right)\right]^{-\frac{1}{3}} \tag{2.46}$$

N_α is Avogadro's number, q is denoted for the numbers of atoms in each each formula unit and M is molecular weight of each formula unit.

The Debye temperature θ_D estimated by Waldron is given by

$$\theta_D = \frac{hcv_{av}}{k_B} \tag{2.47}$$

where $v_{av} = \frac{v_\tau + v_o}{2}$, v_τ and v_o refer to frequency of tetrahedral and octahedral sites respectively. h, K_B and c are the Plank's constant, Boltzmanns constant and velocity of light respectively.

ANISOTROPIC STRAIN (ϵ_{hkl})

In the Uniform Stress Deformation Model (USDM) [175], the anisotropic strain may be expressed as

$$\epsilon_{hkl} = \frac{\sigma}{Y_{hkl}} \tag{2.48}$$

where σ denotes uniform deformation stress and Y_{hkl} is the measure of youngs modulus of elasticity in the crystallographic direction <hkl> which gives modified Williamson-Hall equation as

$$\beta_{hkl}\cos\theta = \frac{A\lambda}{D} + \frac{4\sigma\sin\theta}{Y_{hkl}} \tag{2.49}$$

Y_{hkl} is Youngs modulus of elasticity and its formula for cubic system is as follows:

$$\frac{1}{Y_{hkl}} = S_{11} - 2\left(S_{11} - S_{12} - \frac{1}{2}S_{44}\right)\left(\frac{h^2k^2 + k^2l^2 + l^2h^2}{h^2 + k^2 + l^2}\right) \tag{2.50}$$

Energy Density (u)

Hooke's law gives below the Energy density (u) assuming uniform energy deformation model (UEDM) [56, 173]

$$u = \epsilon_{hkl}^2 \frac{Y_{hkl}}{2} \tag{2.51}$$

Using above relation, the modified W-H equation incorporating UEDM can be expressed as

$$\beta_{hkl} \cos \theta = \frac{A\lambda}{D} + 4 \sin \theta \left(\frac{2u}{Y_{hkl}} \right)^{\frac{1}{2}} \tag{2.52}$$

The relation between uniform deformation stress (σ) & uniform energy density (u) can be obtained from equations (2.48) & (2.51) as

$$u = \frac{\sigma_{hkl}^2}{2Y_{hkl}} \tag{2.53}$$

Dislocations in a crystal are estimated by the following relation

$$\rho = (\rho_D \cdot \rho_s)^{\frac{1}{2}} \tag{2.54}$$

here $\rho_s = C(\epsilon^2/b^2)$, C represents material constant and its value for FCC cubic crystal structure is 16.1 with Burgers vector (b) along easy axis, b denotes modulus of the Burgers vector given by $|b| = a/\sqrt{2}$ where a is the lattice constant [176].

2.4.17   GRIFFITHS MODEL

According to Griffith's model, a strained crack tip produces inhomogeneous strain and stress fields, which can be inferred as the deformation field formed by super-dislocations with Burgers vector (b) [173]. The following correlation is developed based on some simple assumptions:

$$\rho_0 = \frac{G}{2(1 - \sigma)} \rho b D \tag{2.55}$$

where ρ_o being the stress in the parallel direction of b. Also G, D and σ are the shear modulus, crystallite size and Poisson's ratio respectively.

2.4.18   LAPLACE MODEL

This model gives the measure of hydrostatic pressure (P) (also known as Laplace pressure) generated on the surface of synthesized nanoparticle by the intrinsic surface stress expressed by the formula [7, 52]:

$$P = 2\Gamma_s/r \tag{2.56}$$

with r as radius of particle and Γ_s is the surface stress acting on the surface of synthesized nanoparticle .

2.4.19 LAPLACE PRESSURE (P)

P gives the relation between surface elastic strain and surface elastic modulus as [177]:

$$P = \left(\frac{Y}{1 - 2\sigma}\right)\frac{a - a_o}{a} \tag{2.57}$$

where Y being the Youngs modulus, σ is Poissons coefficient and factor (a-a_o)/a gives the volumetric strain.

The surface stress (Γ_s) which produces some surface energy (γ) along with surface strain (ϵ_s) mentioned in following relation [175, 177]:

$$\gamma = \frac{1}{2\Gamma_s\epsilon_s} \tag{2.58}$$

The surface strain ϵ_s is related to surface stress Γ_s and is given by

$$\Gamma_s = \frac{Y_s\epsilon_s}{d_a} \tag{2.59}$$

Y_s gives the surface elastic modulus *i.e.* for surface

$$Y_s = \frac{2Y}{3} \tag{2.60}$$

d_a being the atomic density in a normal direction to the given surface and is expressed by

$$\frac{1}{d_a} = 2r_a \tag{2.61}$$

here $2r_a$ is the particle size and its value for FCC structure is given by

$$r_a = \frac{a}{2\sqrt{2}} \tag{2.62}$$

From equations (2.58, 2.59, 2.60, 2.61 & 2.62) relation for surface energy (γ) can be derived as follows:

$$\gamma = 0.265 \cdot Y\left(\frac{r}{1 - 2\nu}\right)^2 \frac{(a - a_o)^2}{(a)^3} \tag{2.63}$$

CHAPTER 3

MgNi FERRITE NANOPARTICLES SYNTHESIS, STRUCTURAL AND MAGNETIC STUDIES AT 900°C ANNEALING TEMPERATURE

3.1 INTRODUCTION

SNPs are very important materials for human support. Their specific structural, magnetic, electrical and optical properties make them technologically favourable for mankind. They have a general formula MFe_2O_4, M being one or more divalent metal cations such as Fe^{2+}, Zn^{2+}, Ni^{2+}, Co^{2+}, *etc*. These SNPs maintained their importance continuously since last two decades by establishing themselves as suitable candidates for related research due to their amazing magnetic properties, high resistivity and operating on a considerable wide range of frequencies (from hundred Hz to GHz) [177, 178]. The properties of SNPs strongly depend upon the methods of synthesis, selection of material compositions and annealing temperatures [179]. In the present research work, MgNi ferrite nanoparticles were prepared via sol-gel technique [47]. The various important applications of MgNi ferrite nanoparticles include switching devices, sensors to detect gases, microwave devices, memory devices, electric devices and targeted drug delivery, etc. [55, 169, 180, 181]. This material has also find its application in rechargeable batteries in the form of anode material [175]. The XRD analysis is undertaken to estimate the measure of various structural properties *viz*: angular position of diffraction peaks (2θ), lattice spacing (d), particle size (D), X-Ray density (ρ_x) and lattice constant (*a*), *etc*. Fourier transforms infrared (FTIR) spectroscopy is used to observe ferrite formation and locating various functional groups present in the synthesized materials [56, 170, 182]. Vibrating sample magnetometer (VSM) is used for magnetic characterization. [50, 183, 184] and to calculate various magnetic parameters *viz:* magnetic saturation M_S, remnant field M_R, coercive force H_C, value of magnetic moment μ_B, anisotropy constant K and squareness ratio. Topology and morphology of the prepared samples were studied using FESEM, HRTEM and Raman spectroscopy. The optical properties are studied with UV-Vis spectroscopy. The synthesis of such ferrites is also significant because of their continuous use to provide an alternate to conventional energy sources, primarily fossil fuels, *etc*. In the coming decades, renewable energy sources such as hydrogen and oxygen will be critical in safeguarding the future of coming generations. Water, which is abundant on the

planet is the primary source of hydrogen and oxygen. Electro catalysis is needed for water splitting. Iron is usually one among the most cost-effective, abundant and most suitable material for developing oxygen evolution reaction (OER) electro-catalysts. Iron diselenide ($FeSe_2$) noncrystalline plates have been found to be good for OER catalytic performance in recent studies [185]. NiFe mixed oxides have a much stronger OER operation than pure Ni electrodes or other mixed binary oxides [186]. The micro/nanostructure electrodes made of metalorganic super molecular electro catalysts and mixed organic electrocatalysts can show excellent performance in OER as well as hydrogen evaluation reaction (HER) operations [53]. Related OER or HER behaviours can be investigated in oxides of metals (Mg-Ni-Fe). Hierarchical hollow nano tubes (HHNTs) of Cobalt Vanadium phosphide and Nickel Iron Vanadium Layered Double Hydroxide were also discovered to exhibit great selectivity and durability as electrocatalysts for the Nitrogen Reduction Reaction (NRR) to ammonia (NH_3) synthesis [187].

3.2 EXPERIMENTAL DETAILS

3.2.1 SYNTHESIS

The proposed material in the present study *i.e.* $Mg_xNi_{1-x}Fe_2O_4$ (x=0.1875, 0.4375 & 0.8125) was synthesized via aqueous sol-gel route [26]. The synthesis procedure was already discussed in details in chapter 2 section 2.2 and the annealing is done at 900°C [112, 167].

3.2.2 CHARACTERIZATIONS

Using an X-ray diffractometer (Panalytical's X'pert Pro), the structural parameters of the prepared nanoparticles were studied using CuK_α radiations of wavelength 1.5402 Å in the angular range of 10° to 80°. Field emission scanning electron microscopy (FESEM) from Hitachi SU8010, Japan, and high resolution transmission electron microscopy (HRTEM) from FP 5022/22-Tecnai G2 20 S-TWIN, FEI company USA and Raman spectroscopy from Lab RAM HR evolution were used to examine the morphology and topology of the prepared samples. The samples were analyzed using FTIR from Perkin Elmer-Spectrum RX-IFTIR to validate the spinel structures of nanoparticles and functional groups presnt in the SNPs. The magnetic characteristics of the produced ferrites were assessed using VSM from Lake Shore, Model-7410 Series (VSM) at room temperature. UV-Vis spectroscopy was used to investigate the sample's optical characteristics.

3.3 RESULTS AND DISCUSSIONS

3.3.1 X-RAY DIFFRACTION
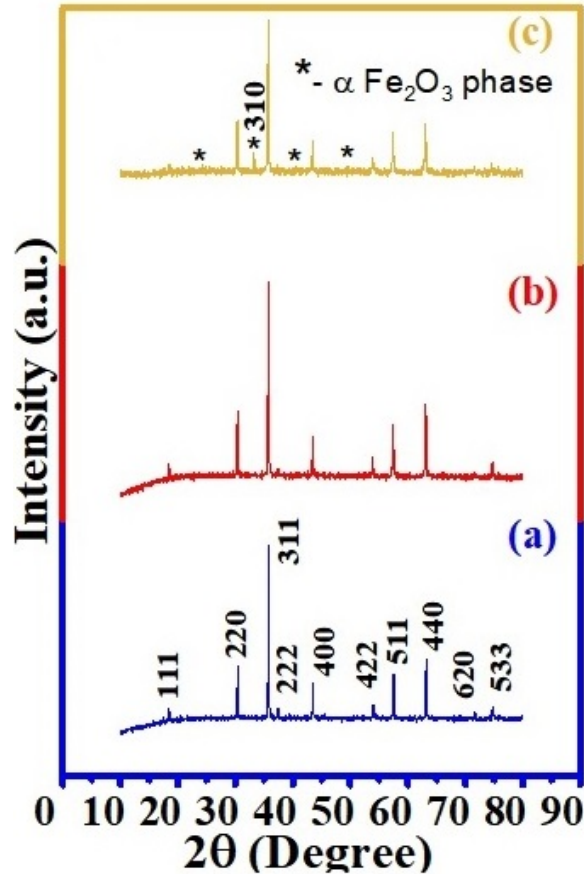
Figure 3.1: XRD Spectra of $Mg_xNi_{1-x}Fe_2O_4$ ferrite SNPs annealed at 900°C, x=(a) 0.1875, (b) 0.4375 & (c) 0.8125

Figure 3.1 shows the X-ray diffraction patterns of ferrite powders of magnesium nickel ferrites $Mg_xNi_{1-x}Fe_2O_4$. The results of X-Ray diffraction indicate that the synthesized materials has a single phase spinel structure [188]. The (hkl) planes reflect various peaks and clearly exhibit crystalline state of the synthesized samples (confirmed with JCPDS card numbers 10-325 and 74-2081) [42]. The lattice constant (a) in each case was calculated using equation 2.3. The XRD patterns of these samples predict that lines and peak positions belongs to spinel structure single phase [180, 189] and cubic symmetry upto 0.4375 atomic percent of Mg^{2+} ions. At higher concentration of Mg^{2+} an additional peak (310) obtained in the XRD spectra visible in figure 3.1. On matching with JCPDS data it is found that the peak belongs to less magnetic α-hematite phase [190].

Using Williamson-Hall analysis of XRD data of all three samples, the obtained W-H plots are shown in figure 3.2. It is observed from the figure that all the three compositions
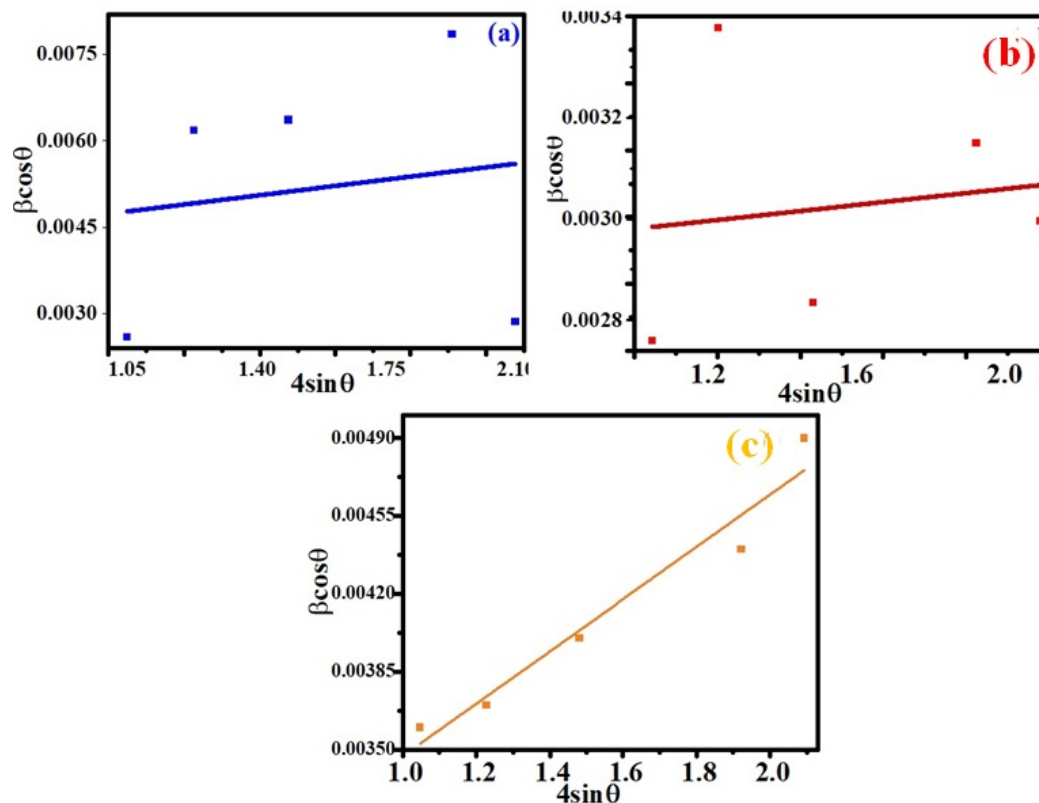
Figure 3.2: W-H plots of $Mg_xNi_{1-x}Fe_2O_4$ ferrite SNPs annealed at 900°C, x=(a) 0.1875, (b) 0.4375 & (c) 0.8125

have positive slope which indicate that the synthesized particles has positive lattice strains leading the lattices to expand. The various lattice parameters *viz:* prominent peak intensity, lattice parameter (*a*), strain (ϵ), crystallite size (D) and lattice spacing (d) are shown for the three synthesized compositions in table 3.1. It is clear from the table 3.1 that with the increasing Mg^{2+} ion composition, lattice parameter and crystallite size both increases. This is due to Mg^{2+} ions having comparatively large size than the replaced Ni^{2+} ions at site-B [112,191].

Table 3.1: Prominent peak (311) intensity, crystallite size (D), lattice spacing (d), lattice parameter (a) and strain (ϵ) of MgNi ferrite SNPs annealed at 900°C

x(Mol.Frac.)	Prominent Peak Intensity (a.u.)	Crystallite Size D (nm)	Lattice Spacing d (Å)	Lattice parameter *a* (Å)	Strain (ϵ)
(a) 0.1875	6269	35	2.505	8.31	0.00129
(b) 0.4375	6324	48	2.508	8.33	0.00117
(c) 0.8125	6549	61	2.511	8.34	0.00103

The variation of crystallite size (D), lattice parameter (a) & strain (ϵ) in $Mg_xNi_{1-x}Fe_2O_4$ nano particles with Mg^{2+} ions composition is shown in figure 3.3.
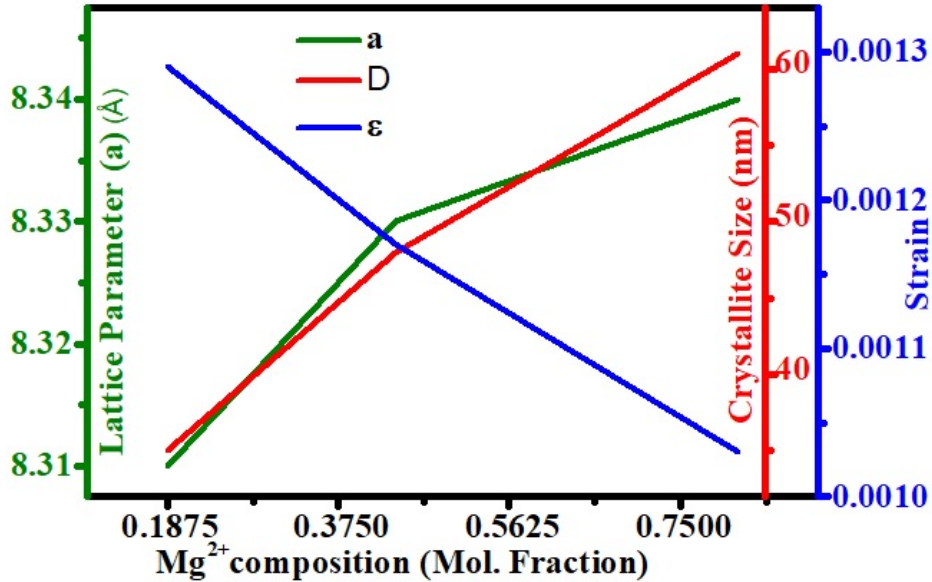
Figure 3.3: Variation of crystallite size (D), lattice parameter(a) & strain (ϵ) in MgNi ferrite SNPs annealed at 900°C with Mg^{2+} ions composition

MgNi ferrite has an inverse spinel structure. In this ferrite the Mg^{2+}, Ni^{2+} and Fe^{3+} ions occupy octahedral site-B whereas remaining Fe^{3+} ions occupy both tetrahedral site-A and octahedral site-B [191]. It is observed that particle size D of prepared nanoparticles increases with Mg^{2+} concentration from 35 to 60 nm. The cation distribution over tetrahedral site-A and octahedral site-B of different sizes has been used to explain the variation in D with increasing Mg^{2+} ions. The increase in particle size D with Mg^{2+} ions is attributed to the replacement of smaller Ni^{2+} (ionic radii = 0.69) ions in site-B with bigger Mg^{2+} (ionic radii = 0.72) ions, resulting in unit cell size enlargement [191]. Further, as the Mg^{2+} ions composition increases, more Mg^{2+} ions replace the Ni^{2+} ions in site-B and enlarge volume of more number of unit cells. The impact of variation of Mg^{2+} ions composition on values of structural parameters such as lattice spacing d, [192] lattice parameter (a) [193] are mentioned in table 3.1. These values are calculated using the equation 2.2 and equation 2.3. The Stocks-Wilson equation 2.4 is used to calculate strain (ϵ) present in nanoparticles and presented in table 3.1 [194, 195]. The calculated strain (ϵ) present in nanoparticles decreases with increase in Mg^{2+} ions composition. The crystallite size (D) and strain present in synthesized nanoparticles are determined by applying Williamson-Hall (W-H) method using eqn.(2.5) [190] and the obtained values are mentioned in table 3.1.

3.3.2   FESEM & EDX CHARACTERIZATIONS

The synthesized nanoparticles were characterized using FESEM. Figure 3.4 shows the FE-SEM micrographs and corresponding histograms of three compositions of $Mg_xNi_{1-x}Fe_2O_4$. It is very much clear from the micro-graphs that the prepared samples are closely identical
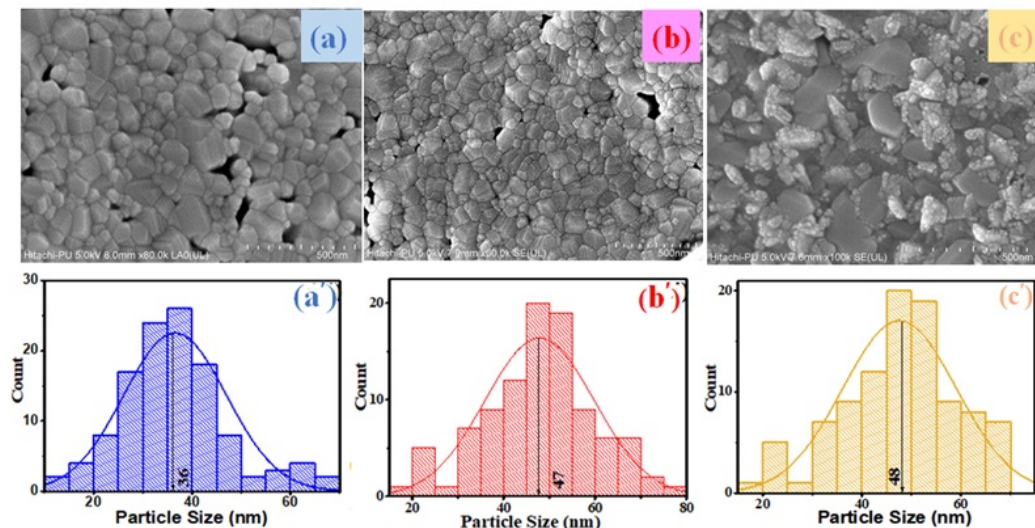
Figure 3.4: FESEM Micrographs of $Mg_xNi_{1-x}Fe_2O_4$ ferrite SNPs annealed at 900°C, x=(a) 0.1875, (b) 0.4375 & (c) 0.8125 SNPs annealed at 900°C and corresponding histograms

in morphology. Their crystallanity increased with Mg^{2+} composition. The particles sizes in each composition is in nano meter range with fairly narrow distribution. However, in synthesized samples some agglomeration of particles is also observed might be due to the magnetic nature of nanoparticles. The EDAX characterization was performed to know the composition of synthesized samples. The EDX spectra of $Mg_xNi_{1-x}Fe_2O_4$ are presented in figure 3.4 and corresponding histograms prepared by measuring the sizes of particles with the help of ImageJ software are presented in figure 3.4. The elemental composition in atomic percentage are tabulated in table 3.2. It is observed that the average particle sizes reported by histograms are in agreement with the crystallite sizes obtained from W-H plots in all the three compositions. Also from EDAX figure 3.5 it was concluded that in all the prepared $Mg_xNi_{1-x}Fe_2O_4$ SNPs all the presursor elements are present in desired atomic percentage. The EDX spectra and corresponding elemental analysis of the synthesized $Mg_xNi_{1-x}Fe_2O_4$ SNPs are presented in figure 3.5.

3.3.3   HRTEM

The synthesized MgNi ferrites SNPs were characterized for HRTEM to study their morphology. HRTEM images along with their corresponding histograms are shown in figure 3.7.

The HRTEM micrographs of all three compositions indicate homogeneous distribution of particles separated by sharp boundaries. Due to mutual magnetic interactions, micrographs for composition x = 0.1875 reveal strongly agglomerated states of nanoparticles
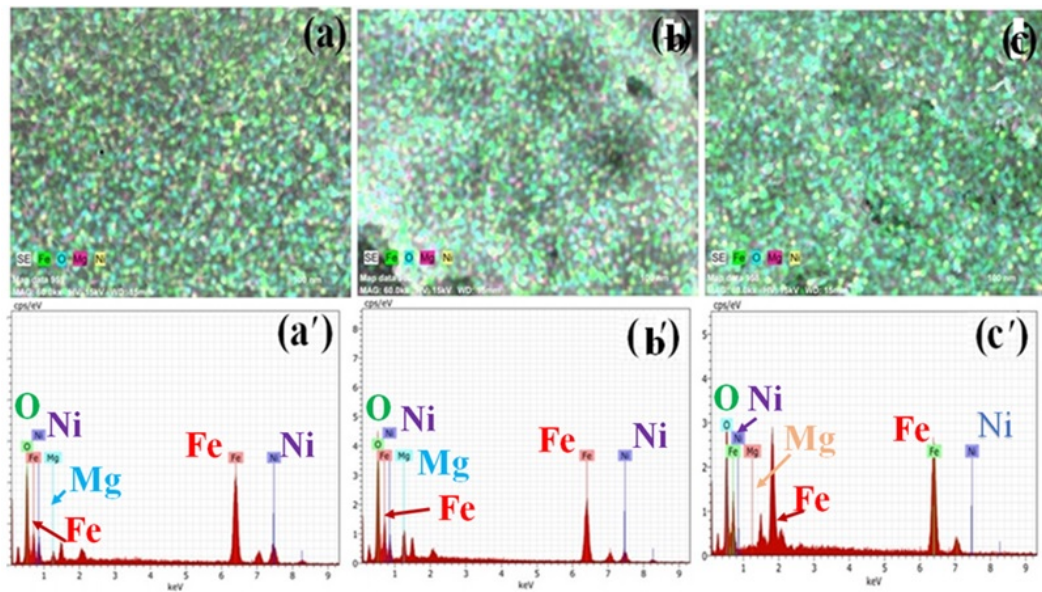
Figure 3.5: EDX spectra and corresponding elemental analysis of $Mg_xNi_{1-x}Fe_2O_4$ SNPs annealed at 900°C, x=(a) 0.1875, (b) 0.4375 & (c) 0.8125 and corresponding elemental mapping
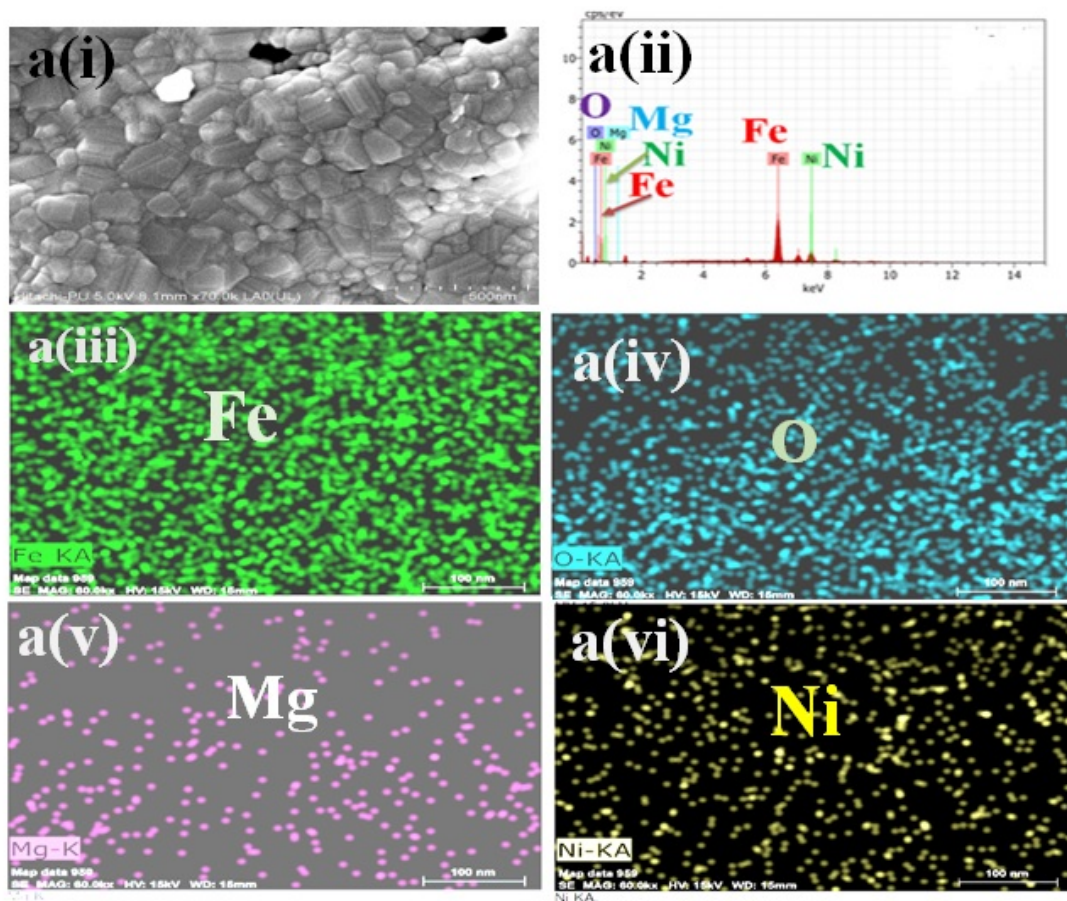
Figure 3.6: EDX spectra and corresponding elemental analysis of MgNi ferrite SNPs annealed at 900°C

Table 3.2: Atomic percentage of elements present in prepared $Mg_xNi_{1-x}Fe_2O_4$ SNPs, x=(a) 0.1875, (b) 0.4375 & (c) 0.8125 annealed at 900°C

(x) (Mol. Frac.)	O (At. Percent)	Fe (At.percent)	Ni (At. percent)	Mg (At.percent)
0.1875	38.3	43.36	16.7	1.65
0.4375	43.71	22.36	6.05	4.72
0.8125	46.46	53.1	0.26	0.18
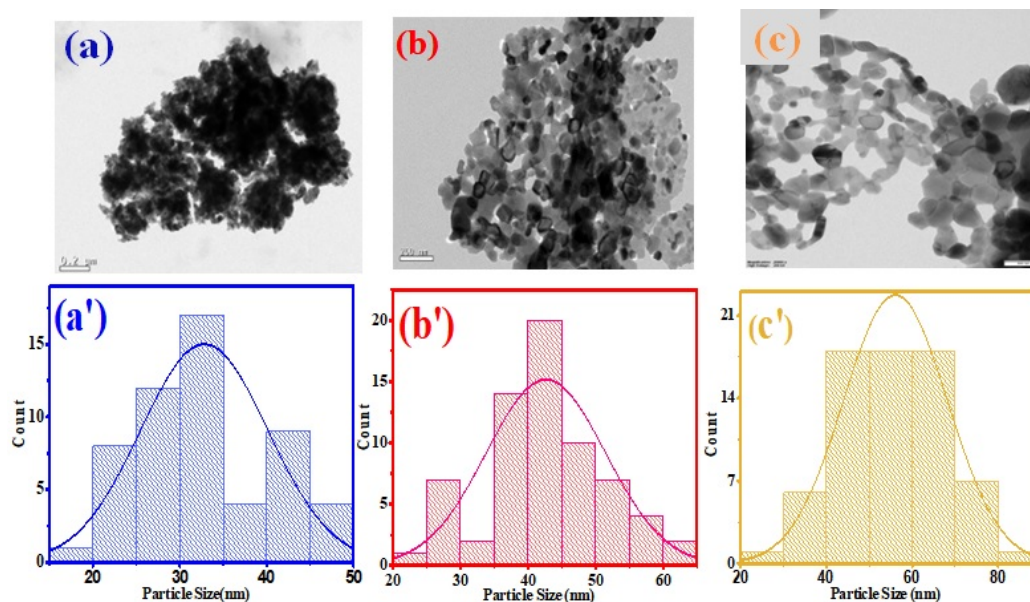
Figure 3.7: HRTEM micrgraph of MgNi ferrite SNPs annealed at 900°C and corresponding histograms

[43]. The particles appeared with uniform grains and free from impurities confirms the crystalline structure of synthesized Mg-Ni nano-ferrites which was also confirmed from their XRD studies [43]. The SAED patterns of $Mg_{0.1875}Ni_{0.8125}Fe_2O_4$ with noncrystalline powders reveal spotty ring patterns of the cubic structure of these SNPs. The measured interplanar spacing (d_{hkl}) from SAED patterns is in accordance with the values obtained from that of XRD analysis summarized in table 3.3.

The high-resolution TEM images in figure 3.7 reveal the details of Mg-Ni ferrites calcined at 900°C with the measured spacing of the lattice fringe of 1.047 nm. Figure 3.8 (iv) corresponds to the <533> plane of $Mg_{0.1875}Ni_{0.8125}Fe_2O_4$ which is in close agreement with the values obtained from results of XRD analysis. The values of lattice spacing related to each ring was measured with ImageJ software and are mentioned in the table 3.3 along with the lattice spacing values obtained from XRD analysis corresponding to each plane for the same sample.

For $Mg_{0.1875} Ni_{0.8125} Fe_2O_4$ samples, annealed at 900°C, diffraction patterns of <111>, <220>, <311>, <400>, <422>, <511>, <440>, <620> and <533> planes were observed by selected area electron diffraction analysis presented in figure 3.8. Therefore, the formation of magnetic $Mg_{0.1875} Ni_{0.8125} Fe_2O_4$ SNPs annealed at 900°C temperature is confirmed.
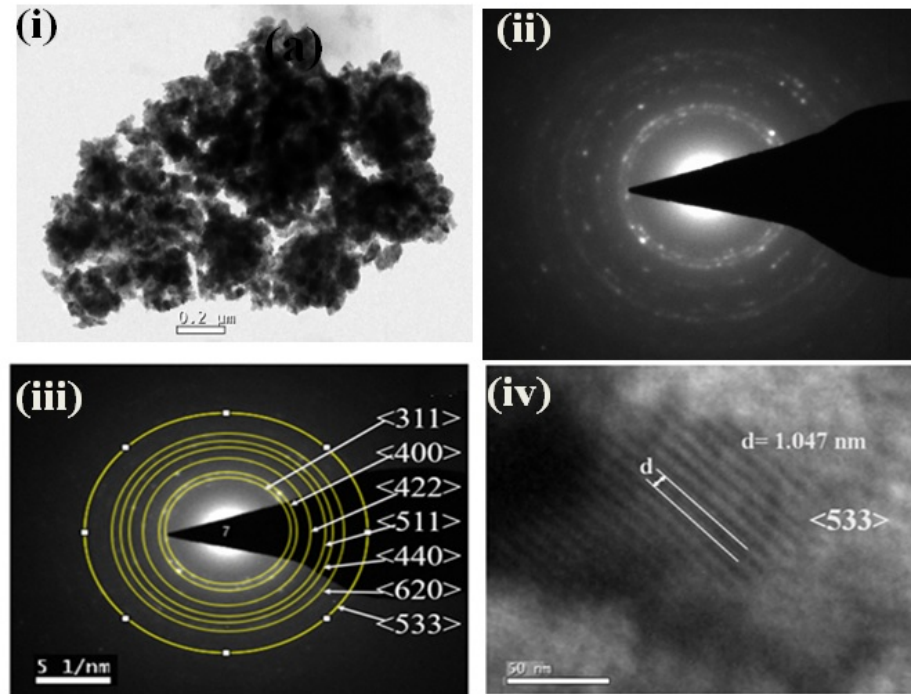
Figure 3.8: (i) HRTEM image, (ii) (SAED) pattern SAED image , (iii) identification of rings and lattice spacing measurement and (iv) lattice spacing calculation for MgNi ferrite SNPs

Table 3.3: Measured interplanar spacing <d_{hkl}> obtained from SAED patterns of MgNi ferrite SNPs annealed at 900°C

Ring	Calculated interplanar spacing (d_{hkl}) HRTEM analysis	Calculated interplanar spacing (d_{hkl}) in XRD analysis	Plane <hkl>
R1	4.978	4.79	111
R2	2.623	2.937	220
R3	2.382	2.505	311
R4	2.195	2.398	222
R5	1.922	2.078	400
R6	1.768	1.697	422
R7	1.604	1.6	511
R8	1.507	1.47	440
R9	1.406	1.315	640
R10	1.319	1.268	533

3.3.4 FTIR SPECTROSCOPY

FTIR plots of $Mg_{0.1875}$ $Ni_{0.8125}$ Fe_2O_4 SNPs are shown in figure 3.9. From the figure 3.9 it is observed that the first two bands in the range 428-435 cm^{-1} and 568-583 cm^{-1} correspond to octahedral and tetrahedral sites respectively, confirming the formation of single phase SNPs. The change in cation-oxygen bond (A-O) lengths can cause change in the band positions of MgNi ferrite [24, 172]. There are four metal-oxide ions bonds (MO_4) in ferrites of which three are octahedral oxide bonds (o-O) and fourth one is tetrahedral oxide bond (τ-O). If there are no tetrahedral connections the three oxide ions vibrate in any direction with constant frequencies in this isotropic zone.

The presence of tetrahedral bonds, on the other hand, significantly increases the frequency of vibrations (v_τ) along the τ-O axis, whereas the frequency of vibration (v_0) changes (may increase or decrease) only if bending force constants occur perpendicular to the τ-O axis [172].

When IR radiation impinge on the ferrite, the τ-O and o-O bonds absorb their distinctive energy radiations and oscillate. There are two types of oscillations they may have;

i) Oscillation along the axis of the metal-oxide bond.

ii) Oscillation in the perpendicular direction of the M-O bond.

The oxide ions travel only along the τ-O axis when vibrations occur along the M-O axis, resulting in linear force constants. However, when oxide ions vibrate perpendicularly to the M-O axis, a bending-like condition occurs, in which the oscillating oxide ion bends the o-O bond about its mean direction, resulting in bending force constants. The isotropic force field environments that surround metal ion complexes at two crytallite sites *i.e.* tetrahedral or octahedral sites, known as v_3 and v_4 modes, oscillate as well. These vibration modes (v_3) and (v_4) were not observed in the current study for any of the three compositions. The
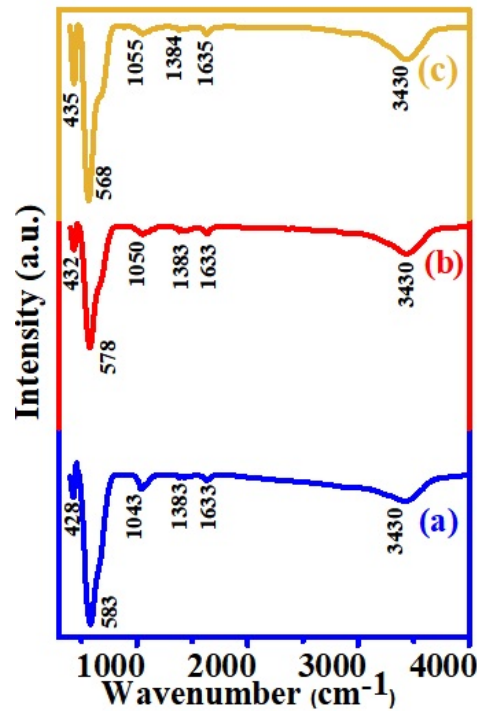
Figure 3.9: FTIR plots of MgNi ferrite SNPs annealed at 900°C

first primary band appears to be splitting in all three compositions in figure 3.9 shown by the FTIR spectrum. The presence of Fe^{2+} ion in ferrites causes John-Teller distortion which causes the splitting. The existence of Mg^{2+}- O^{2-} complexes may explain the high frequency bands around the octahedral site-B [196]. The C=O stretching vibration characteristic peak for the material $Mg_xNi_{1-x}Fe_2O_4$ is located at 1633 cm^{-1} for all three formulations. Water molecules present in band about 3431 cm^{-1} may be due to the stretching of the O-H bond of water molecules which is absorbed by nanoparticles [42, 195, 195, 197]. A band about 1040 -1070 cm^{-1} represents the C-O group vibration modes, while a band around 1350-1500 cm^{-1} represents -CH_3 bending [195].

Table 3.4: Different FTIR band positions in MgNi ferrite SNPs annealed at 900°C

S.N.	Band Position (cm^{-1})	Assignment
1	428-435	Fe-O bond (Octahedral Band)
2	568-583	Mg/Ni/Fe-O bond (Tetrahedral Band)
3	1043-1055	Presence of C-O bond
4	1383-1384	-CH_3 bending
5	1633-1635	Presence of C=O bond
6	3430	Presence of water molecule

3.3.5 RAMAN SPECTROSCOPY

The phonon vibration of crystalline solids are investigated with a sensitive tool known as Raman spectroscopy. The Raman spectra of $Mg_xNi_{1-x}Fe_2O_4$ annealed at 900°C were studied using the Raman spectrometer. Raman spectra of these nano particles in the range of 100-800 cm^{-1} is shown in figure 3.10. The spinel unit cell has 56 atoms, yet the simplest
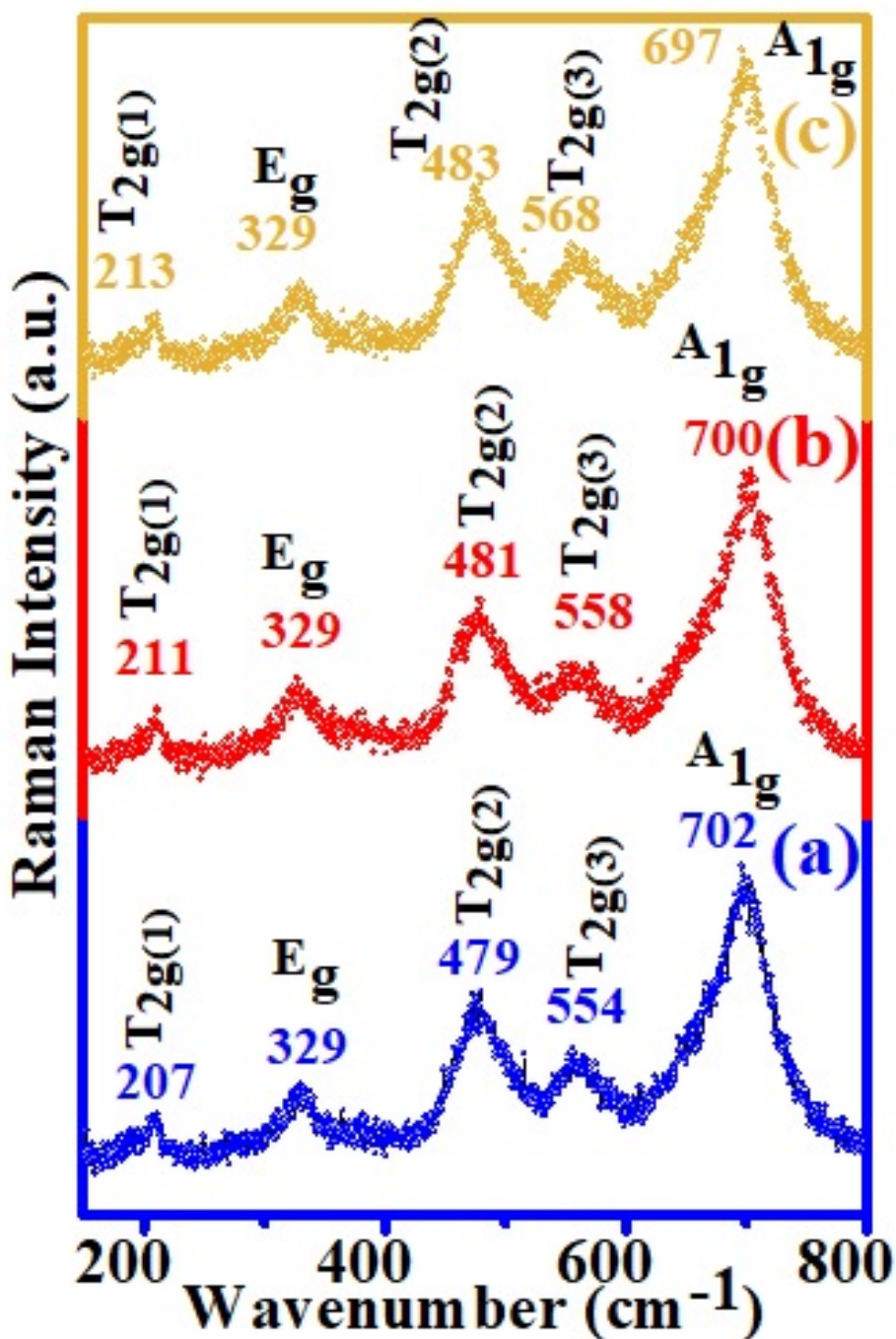
Figure 3.10: Raman spectra of MgNi ferrite SNPs annealed at 900°C

primitive cell only requires 14 atoms. At k = 0, a group theory research predicts 42 vibra-

tional modes in the spinels, 3 acoustic modes and 39 visual modes. In spinel ferrites, only five modes $A_{1g} + E_g + 3T_{2g}$ have been reported. There are three Raman active T_{2g} modes: $T_{2g}(1)$, $T_{2g}(2)$ and $T_{2g}(3)$ with $T_{2g}(1)$ indicating the lowest Raman shift and $T_{2g}(3)$ indicating the Raman symmetry mode at the highest wavenumber.

The A_{1g} mode denotes a symmetric stretch of oxygen atoms along FeO bonds, while the modes E_g and $T_{2g}(3)$ represent symmetric and asymmetric bends of oxygen with respect to Fe, respectively. Mode $T_{2g}(2)$ denotes asymmetric stretching of Fe and O, while mode $T_{2g}(1)$ denotes translational displacement of the entire FeO_4 [198].

Table 3.5 shows the characteristic bands found in the magnesium nickel ferrite, which are in good agreement with the earlier recorded values [198]. The observed band pattern from 207 cm^{-1} to 213 cm^{-1} for sample (a), (b) & (c) annealed at 900°C, signals towards the presence of hematite traces in the said synthesized nanoparticles. Similar Raman spectra with a strong band about 329 cm^{-1} have been published in the literature caused by deal D3d symmetry's strong distortion for nickel SNPs [198]. The various band positions of different Raman modes of $Mg_xNi_{1-x}Fe_2O_4$ annealed at 900°C are placed in table 3.5.

An absorption band found in the range of 100-1000 cm^{-1} usually corresponds to the NiO phase. Higher annealing temperatures result in small rise in NiO traces. The broad band around 479 cm^{-1} for all three samples is attributed to (Fe^{+3}) at site-A and 695 cm^{-1} to (Mg^{2+}, Ni^{2+}, Fe^{3+}) at site-B positions respectively [197].

Table 3.5: The variation of different Raman modes of MgNi ferrite SNPs annealed at 900°C

Assignment	Origin of Mode	Raman Modes (cm^{-1})		
		(a) 0.1875	(b) 0.4375	(c) 0.8125
$T_{2g}(1)$	The symmetric bending of oxygen atom with respect to the metal ion in AO4 unit	207	211	213
E_g	Due to the asymmetric bending of oxygen	329	329	329
$T_{2g}(2)$	Due to asymmetric stretching of (Fe/Ni)O bond	479	481	483
$T_{2g}(3)$	Attributed to the translational movement of the tetrahedron (metal ion at tetrahedral site together with four oxygen atoms)	554	558	568
A_{1g}	Assigned as the symmetric breathing mode of the AO4 unit with spinel lattice (highest frequency)	702	700	697

3.3.6 MAGNETIC CHARACTERIZATION

The magnetic properties of $Mg_xNi_{1-x}Fe_2O_4$ SNPs were carried out using VSM at room temperature as shown in figure 3.11. Table 3.6 shows the values of saturation magnetization (M_S), retentivity (M_R), coercivity (H_c), Bohr's magnetron (μ_B), squareness ratio (M_R/M_S) and anisotropy constant (K).

It is clear from the table 3.6 that the net magnetic moment μ_B and saturation magnetization M_S decreases with the increase in Mg^{2+} ion composition. This decrease is attributed to the inverse spinel structure of MgNi ferrites. When Mg^{2+} composition increases, these ions replace more magnetic Ni^{2+} ions from site-B of the lattice. As the net dipole moment of the lattice = m(B)-m(A), the net dipole moment of the sample decreases [49,170,199,200]. The Mg^{2+}, Ni^{2+}, and Fe^{3+} ions have magnetic moment values of 0, 2 $\sqrt{2}$ and 6 BM respectively. The magnetic moment (μ_B) is determined using equation 2.12 [201].
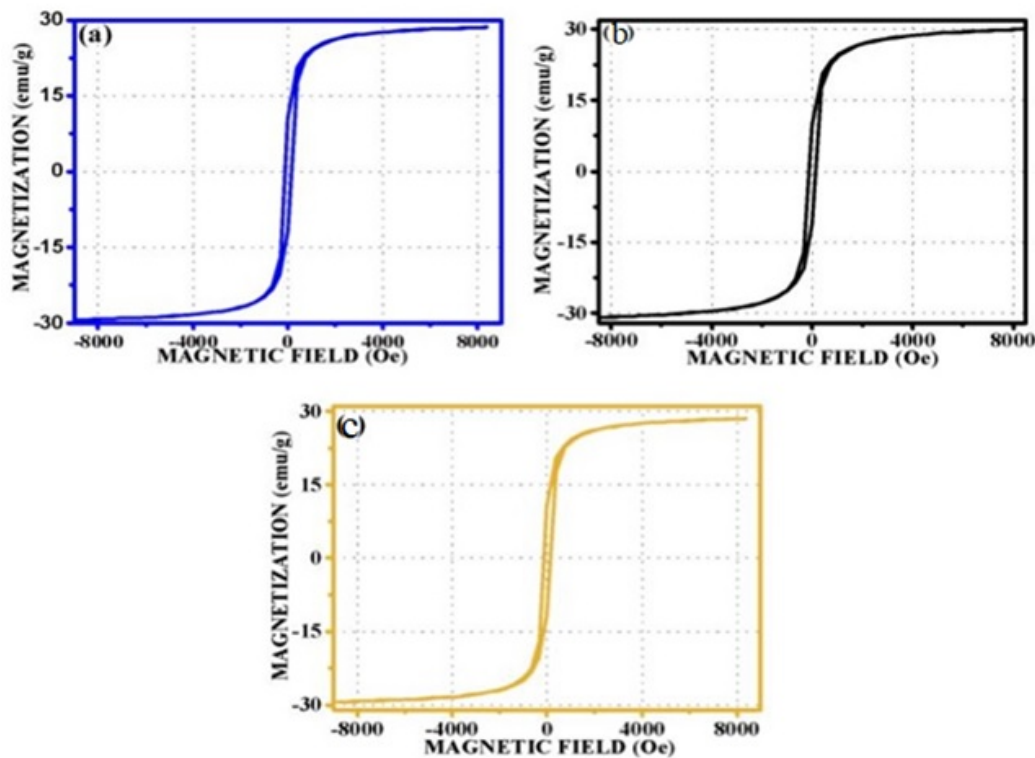
Figure 3.11: Hysteresis loops of MgNi ferrite SNPs annealed at 900°C at room temperature (300K)

It is also found that M_S first decreases from x = 0.1875 to x = 0.4375 with increasing Mg^{2+} composition gradually but drastically decreases beyond x= 0.4375. The drastic decrease in the value of M_S at x = 0.4375 is attributed to secondary hematite phase effect [112]. The secondary hematite phase effect on M_S is described by the spin canting effect. The low M_S value obtained at x = 0.8125 is due to the anti-ferromagnetic hematite phase, which is present in significant numbers in this composition with spinel phase. The presence of hematite phase is confirmed by peaks in XRD spectra denoted by * marks in figure 3.1

44

in chapter 3. When anti-ferromagnetic hematite and ferromagnetic spinel phases interact, dominant spin canting effect occurs which decreases the total magnetic moment. As a result, the M_S value of the material decreases.

Table 3.6: Values of M_S, H_C, M_R, μ_B, M_R/M_S and anisotropy constant K of MgNi ferrites annealed at 900°C

x(mol.frac.)	M_S (emu/g)	μ_B (emu/g)	M_R (emu/g)	Hc(Oe)	M_R/M_S	K (erg/cm3)
0.1875	30.32	1.24	10.80	135	0.3562	4264
0.4375	29.10	1.14	10.11	127	0.3474	3850
0.8125	23.32	0.86	06.65	78	0.2852	1895

The value of coercivity also decreases with increase in Mg^{2+} composition which may be attributed to increase in crystallite size. This is because large crystallite size pave less magnetoresistance to rotate the dipoles in the external applied magnetic field [162]. The value of M_R/M_S lies in the range of 0 to 0.5 indicate the magnetostatic interaction between the prepared nanoparticles. The small values of coercivity of these nanoparticles indicates that these nanoparticles are near the superparamagnetic limit which is the ideal regime for several biomedical applications [202]. The equation 2.11 is used to estimate the rising trend in the magneto crystalline anisotropy energy (K) value of MgNi ferrite [112] and the values are tabulated in table 3.6.

The above findings show that all prepared powder samples are magnetically soft. Due to their very good magnetic properties and chemical stability, they are widely used in industries. Magnetic metal oxide nanoparticles are very important nanomaterials used for the development of EMI shielding with the mechanism of absorption due to their high EM wave absorption properties [203, 204]. Finally, it can be concluded that both the structural as well as magnetic properties of inverse spinel ferrite nanoparticle system directly depend upon compositions of elements at site-B [45].

3.3.7 UV-VIS SPECTROSCOPY

A UV-Vis spectrophotometer (Model: V670 Jasco, International) was used to determine the UV absorption spectrum of synthesized ferrites.

The optical properties of the magnesium nickel ferrite nanoparticles of $Mg_xNi_{1-x}Fe_2O_4$ were studied by UV-Vis spectrophotometer in the wavelength range 200 nm to 800 nm . Figure 3.12 reveals the absence of absorption band edges in the wavelength range 200 nm to 800 nm indicating that the materials do have very high optical band gap. Thus the synthesized nano materials are insulators. The electrical properties of ferrite nanoparticles are indeed related to the variation of their energy band gap. Due to this fact the energy band
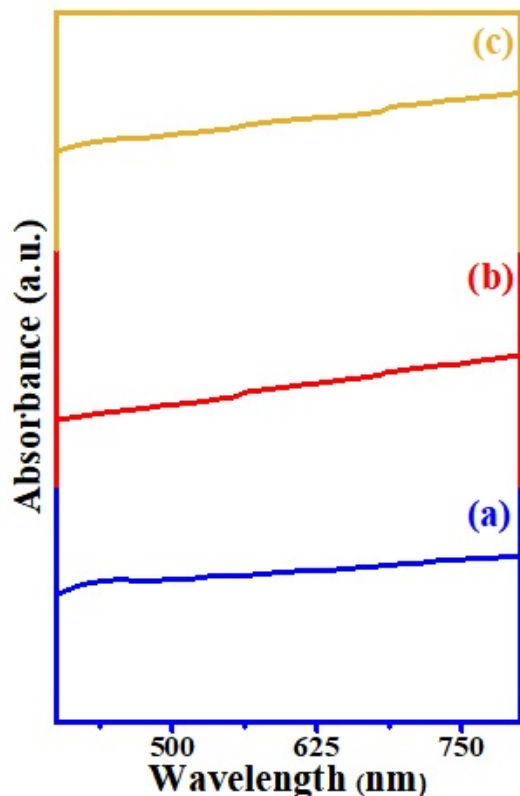
Figure 3.12: UV-Vis spectra of MgNi ferrite SNPs annealed at 900°C

gap in ferrites is comparable to that of semiconductor materials. Thus ferrite nanoparticles significantly can be operated at higher temperatures under normal conditions [43, 49, 201, 205, 206].

3.4 CONCLUSION

The XRD results shows that the $Mg_xNi_{1-x}Fe_2O_4$ are successfully synthesized via sol-gel techniques annealed at 900°C are in nanorange. FESEM results shows that all the synthesized particles have acquired cubical morph logy and all the elements are present during the synthesis. The TEM studies shows that particles are separated by sharp edges and the particle sizes in all three composition (measured with InmageJ software) are in good agreement with the crystallite sizes obtained by XRD analysis. The synthesized particles are of single phase and nano size . FTIR and Raman studies shows the formation of synthesized particles as spinel structure. However, XRD spectra of synthesized particle having higher composition of Mg^{2+} ions, consists of additional peaks belong to α-hematite phase. Crystallite size found increased with the increase in Mg^{2+} ion composition. The saturation magnetization M_S, Retentivity M_R and coercivity H_C, all found to decrease with the increasing Mg^{2+} ion composition. The squareness ratio M_R/M_S indicates that the synthesized particles are super-paramagnetic in nature.

CHAPTER 4

MgNi FERRITES NANOPARTICLES SYNTHESIS, STRUCTURAL AND MAGNETIC STUDIES AT 1100°C ANNEALING TEMPERATURE

4.1 INTRODUCTION

There are enormous methods for the synthesis of SNPs [169] *viz*: solid-state reaction, self-propagating micro-emulsion, co-precipitation, high-temperature mechano-synthesis, sol-gel technique, *etc*. [42, 47, 50, 180, 181]. Their properties are also largely determined by the annealing temperature. The average particle size and lattice constant increases [207] at higher annealing temperature of the material. For all the three synthesized compositions of the $Mg_xNi_{1-x}Fe_2O_4$ (x = 0.1875, 0.4375, & 0.8125), the observed band pattern from the FTIR confirmed their spinel structure [208, 209]. The magnetic behaviour of some ferrite nanoparticles is also observed at different annealing temperature which shows a transition from the paramagnetic to ferromagnetic region in nanoparticles [43]. The material is synthesized via acquous sol-gel technique and annealed at 1100°C in the present study. The obtained powder form of the material annealed at 1100°C were characterized by XRD, FESEM, HRTEM, FTIR, Raman, VSM and UV-Vis spectroscopy to obtain the structural, optical and magnetic properties.

4.2 EXPERIMENTAL DETAILS

4.2.1 SYNTHESIS

The proposed material in the present study *i.e.* $Mg_xNi_{1-x}Fe_2O_4$ (x=0.1875, 0.4375 & 0.8125) was synthesized *via* aqueous sol-gel route [26]. The synthesis procedure has already been discussed in detail in chapter 2 section 2.2.1. The annealing of the material was carried out at 1100°C.

4.2.2 CHARACTERIZATIONS

Using an x-ray diffraction (Panalytical's X'pert Pro), the structural parameters of the prepared nanoparticles were studied using CuK_α radiations of wavelength 1.5402 Å for 10° to 80° angular range.FESEM, Hitachi SU8010, Japan, and HR-TEM, FP 5022/22-Tecnai G2 20 S-TWIN, FEI company of USA and Raman Spectroscopy were used to examine the morphology and topology of the prepared samples. The samples were analysed using FTIR (Perkin Elmer-Spectrum RX-IFTIR) to validate the spinel structures of nanoparticles and funtional groups presnt in the SNPs. The magnetic characteristics of the produced ferrites were assessed using VSM (Lake Shore, Model-7410 Series VSM) at room temperature. UV-Vis spectroscopy was used to investigate the sample's optical characteristics. To determine the atomic structure in the synthesized ferrites, Raman spectroscopy carried out using Lab RAM HR evolution software.

4.3 RESULTS AND DISCUSSIONS

4.3.1 X-RAY DIFFRACTION

Figure 4.1 shows the XRD spectra of magnesium nickel ferrites $Mg_xNi_{1-x}Fe_2O_4$. In these synthesized materials, the presence of various < hkl> planes verifies the formation of single phase cubic spinel crystal structure having f d -3 m space group symmetry [42]. The results are also confirmed by JCPDS card numbers 10-325 and 74-2081 [42, 180, 189].

Various lattice parameters *viz*: prominent peak intensity, crystallite size $D_{(W-H)}$, lattice spacing (d), lattice parameter (*a*) and lattice strain (ϵ) of $Mg_xNi_{1-x}Fe_2O_4$ annealed at 1100°C nanoparticles are given in table 4.1. In MgNi ferrite nanoparticles, [Fe^{3+}] ions prefer tetrahedral site-A in the ferrite lattice [189] while Mg^{2+} and Ni^{2+} ions have preference over octahedral site-B [189].

It is observed from the table 4.1 that the lattice parameter (*a*) and crystallite size (D) of $Mg_xNi_{1-x}Fe_2O_4$ NPs increases with increase in Mg^{2+} ion composition. The peak intensities of $Mg_xNi_{1-x}Fe_2O_4$ nanoparticles is in the order $I_{0.1875} > I_{0.4375} > I_{0.8125}$. In each sample the average crystallite (particle) size was calculated by measuring FWHM only of most significant peaks *viz:* (220), (311), (400), (511) & (440) [112, 167, 191].

Structural parameters obtained using Scherers formula given in equation 2.1 are shown in table 4.1 [188]. MgNi ferrite has an inverse spinel structure [167]. In this ferrite the Mg^{2+}, Ni^{2+} and Fe^{3+} ions, occupy octahedral site-B whereas remaining Fe^{3+} ions occupy tetrahedral site-A [191]. The particle size (D) of produced nanoparticles increases from 66 nm to 94 nm as Mg^{2+} ion composition increases. The cation distribution over tetrahedral site-A and octahedral site-B has been used to explain the variation in D with increasing Mg^{2+} ions. The increase in D with Mg^{2+} ions is attributed to the replacement of smaller
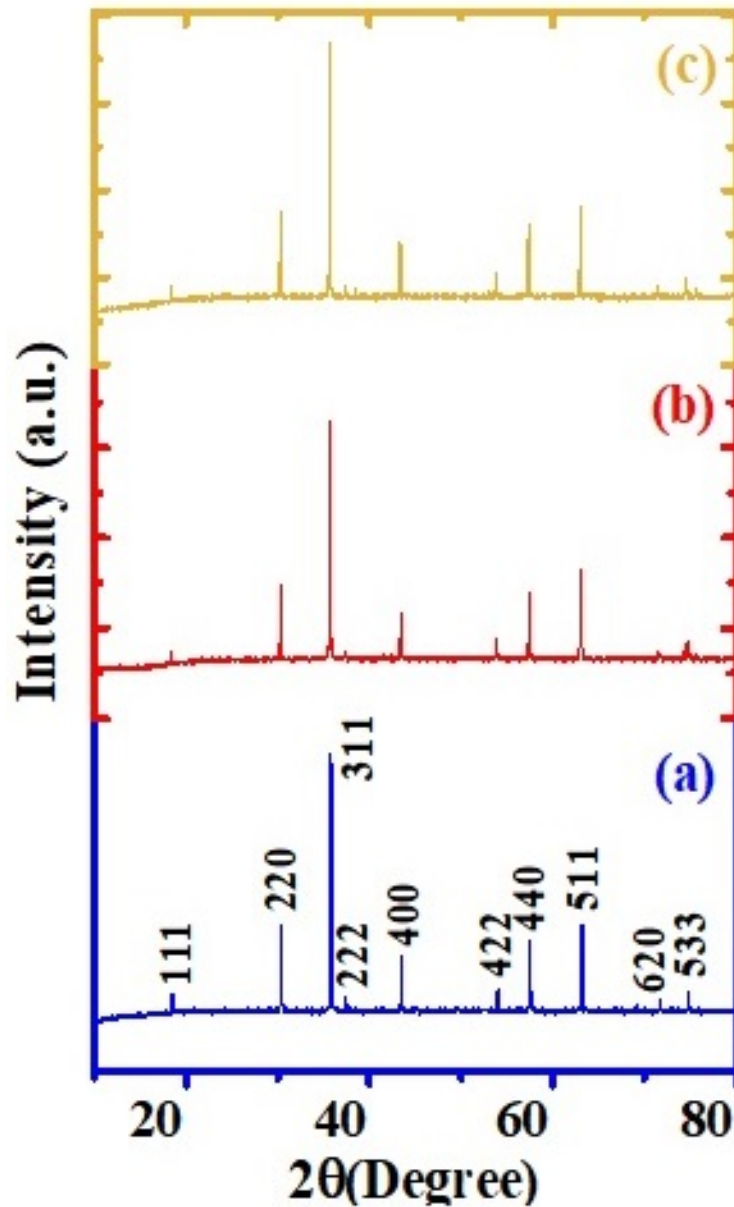
Figure 4.1: XRD Spectra of MgNi ferrite SNPs annealed at 1100°C

Ni^{2+} (ionic radii = 0.69) ions at site-B with bigger Mg^{2+} (ionic radii = 0.72) ions, resulting in unit cell size enlargement [191]. Further as the Mg^{2+} ions composition increases, more Mg^{2+} cations replace the Ni^{2+} cations at site-B and enlarges volume of more number of unit cells. The impact of variation of Mg^{2+} ions composition on values of structural parameters such as lattice spacing (d) [192], lattice parameter (a) [193] are mentioned in table 4.1. These values are calculated using the equation 2.2 and equation 2.3.

It has been noticed that in all prepared samples, the value of average lattice spacing (d) and lattice constant (a) rises with Mg $^{2+}$ ions concentration [190]. The Stocks-Wilson equation (2.4) is used to obtain the value of strain (ϵ) present in nanoparticles given in table 4.1 [194]. The strain (ϵ) present in nanoparticles is found to decrease with increase in Mg

49

Table 4.1: Prominent peak intensity, particle size (D), lattice spacing (d), lattice parameter (*a*) and strain (ϵ) of MgNi ferrite SNPs annealed at 1100°C

x (Mol.Frac.)	Prominent peak intensity (a.u.)	particle size (D) (nm)	lattice spacing (d) (Å)	lattice parameter (a) (Å)	Strain (ϵ)
(a) 0.1875	7773	66	2.05	8.31	0.00052
(b) 0.4375	7757	91	2.11	8.33	0.00044
(c) 0.8125	7572	94	2.13	8.34	0.00041

$^{2+}$ ions composition. The particle size D and kind of strain that contained in nanoparticles are approximated by applying Williamson-Hall (W-H) method using equation 2.5 and the obtained values are mentioned in table 4.1 [180]. The variation of D, (*a*) and (ϵ) in MgNi ferrite SNPs with Mg^{2+} ions composition is shown in figure 4.2. The W-H plots for three
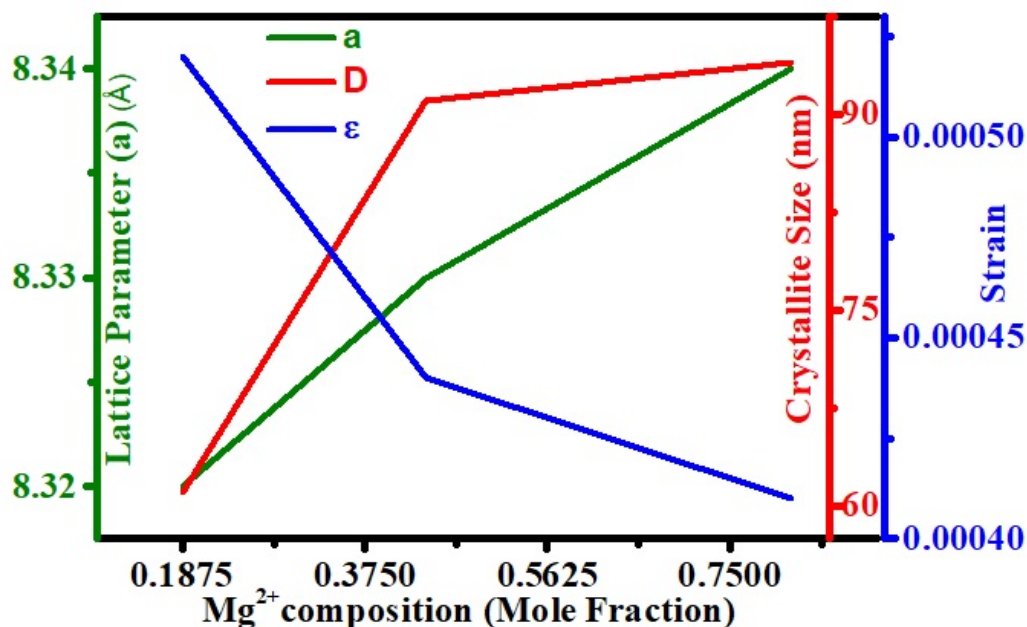
Figure 4.2: Variation of crystallite size (D), Lattice parameter(*a*) & strain (ϵ) in MgNi ferrite SNPs with Mg^{2+} ions composition

samples of $Mg_xNi_{1-x}Fe_2O_4$ are shown in figure 4.3. The crystallite size obtained from W-H plots (D $_{W-H}$) are in good agreement to that calculated from Scherers formula. It is also found that in the W-H plots of all the compositions the slope of the linear fit are positive confirming the presence of tensile strain in the nanoparticles [180]. The tenstile strain in these materials cause the expansion of the lattice. In the present study the lattice in all the three synthesized compositions of $Mg_xNi_{1-x}Fe_2O_4$ found to increase with the increase in Mg^{2+} ions composition.
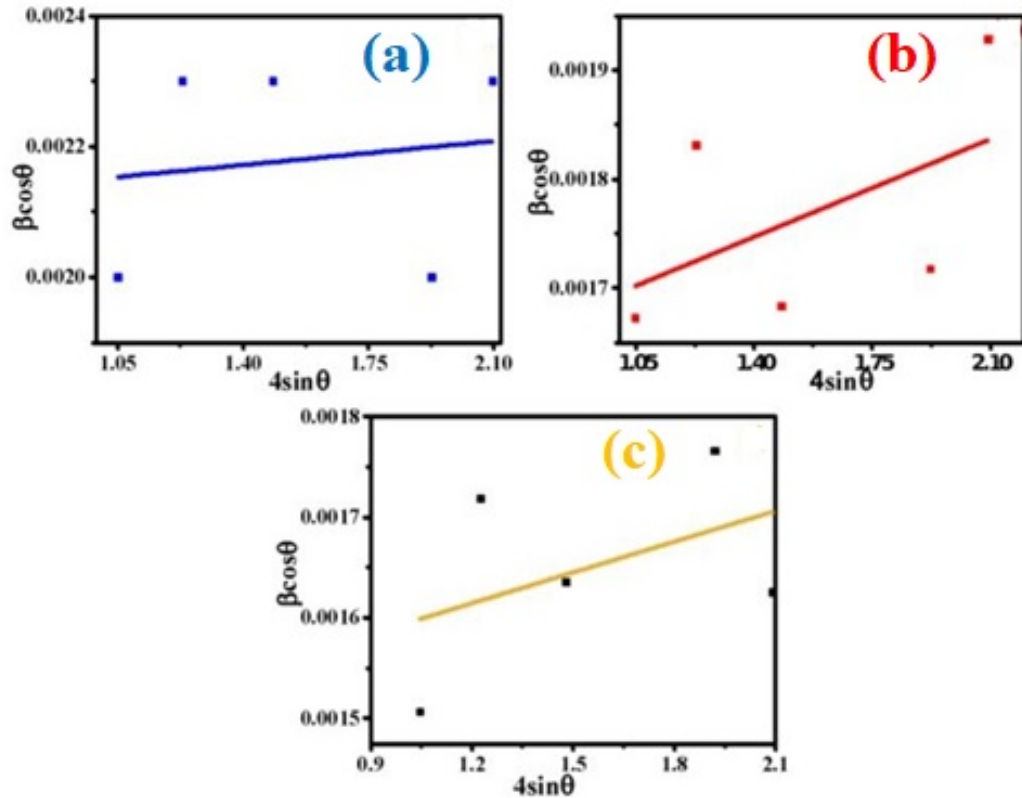
Figure 4.3: W-H plots of MgNi ferrite SNPs annealed at 1100°C

4.3.2   FESEM-EDX CHARACTERIZATION
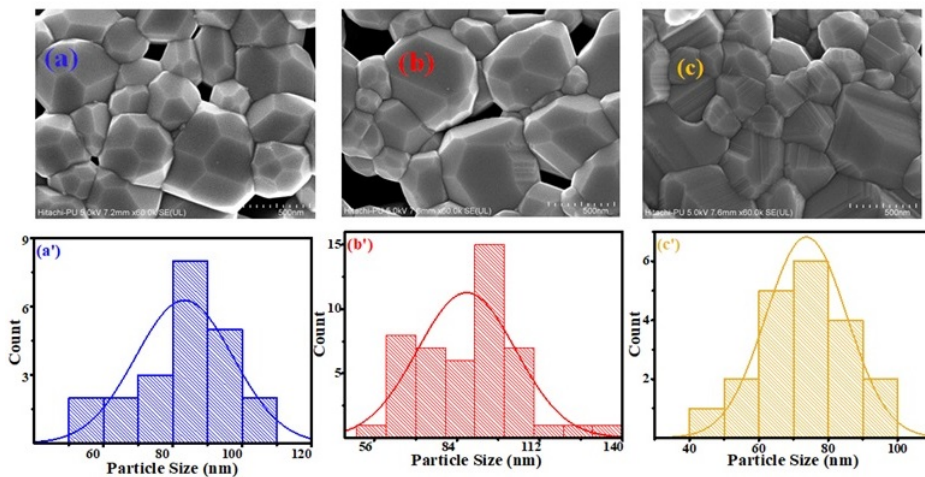
Figure 4.4: FESEM micrographs of MgNi ferrite SNPs annealed at 1100°C and corresponding histograms

The synthesized samples were also characterized for FESEM to study their morphology and elemental analysis. Figure 4.4 shows the FESEM micrographs of $Mg_xNi_{1-x}Fe_2O_4$ and their corresponding histograms to statistically estimate the size of particles. From the FE-SEM results, it is observed that the particle sizes are found in nano meter range.

51

Table 4.2: Elemental atomic percentage of MgNi ferrite SNPs annealed at 1100°C

Composition (x) (mol. frac.)	O (At. %)	Fe (At. %)	Ni (At. %)	Mg (At. %)
0.1875	38.3	43.36	16.7	1.65
0.4375	43.71	22.36	6.05	4.72
0.8125	46.46	53.1	0.26	0.18

The magnetic nature of nanoparticles causes agglomeration in samples. EDX is carried out for stoichiometry analysis of prepared samples. Figure 4.5 shows the EDX spectra of $Mg_{0.1875}Ni_{0.8125}Fe_2O_4$ and table 4.2 shows the atomic percentages of elements in the prepared nanoparticles. The results confirmed exactly that the elements in all the prepared samples are in stoichiometric ratio. The size of nano particles of the samples obtained from XRD analysis are verified from the particle size obtained from histogram created from FE-SEM micrograph by using Image J software. The EDAX analysis is carried out for all
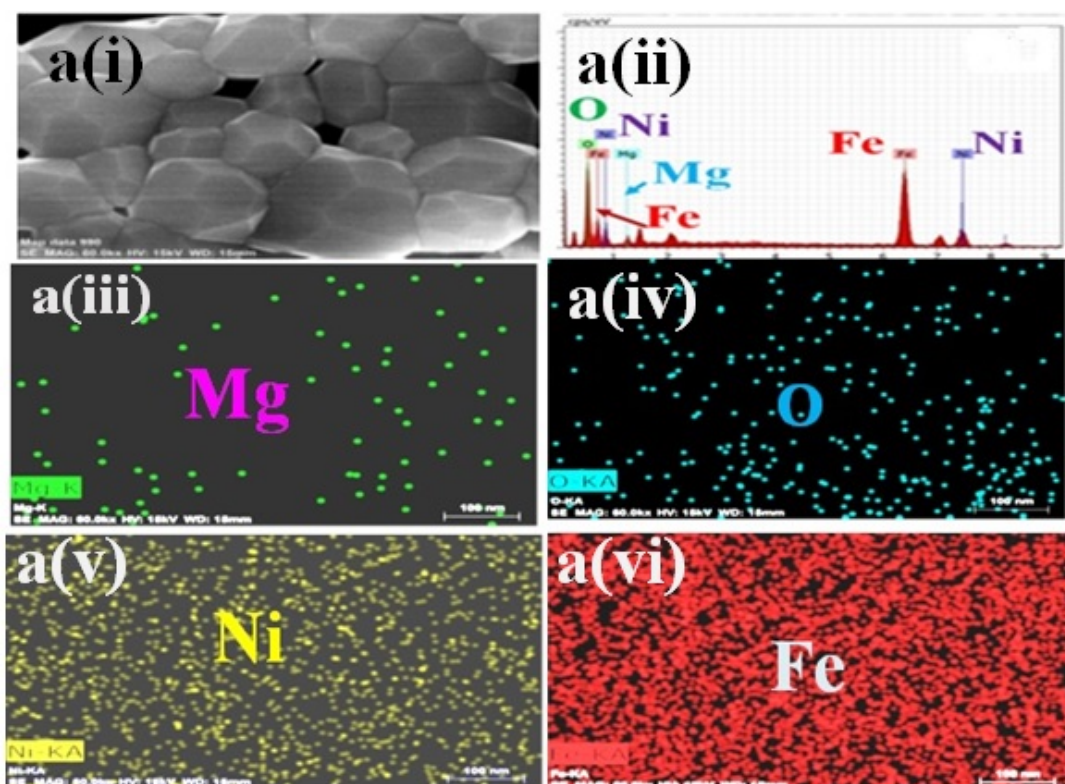
Figure 4.5: EDX spectra and corresponding elemental analysis of MgNi ferrite SNPs annealed at 1100°C

the three compositions of $Mg_xNi_{1-x}Fe_2O_4$ and are presented in the figure 4.6. From the micrographs, it is observed that all the synthesized compositions have elements under consideration with no impurities mark.

Figure 4.5 (a) (i) gives the micrographs of $Mg_{0.1875}Ni_{0.8125}Fe_2O_4$ characterized for EDAX
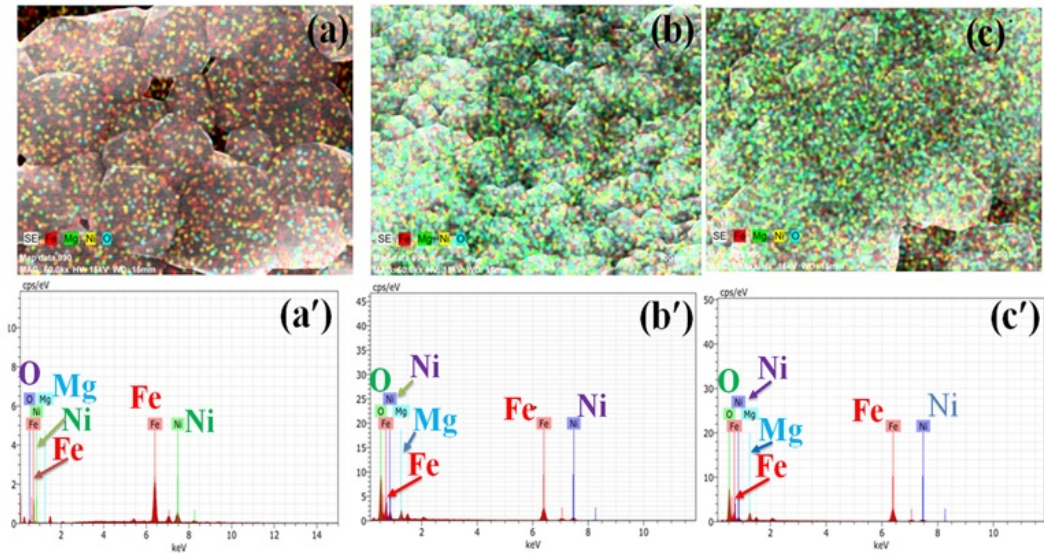
Figure 4.6: EDX spectra and corresponding elemental mapping of MgNi ferrite SNPs annealed at 1100°C

analysis, a(ii) gives the elements present in the sample, a(iii) is the micrographs representing the composition of magnesium, a(iv) is the micrographs representing the composition of oxygen, a(v) is the micrographs representing the composition of nickel and a(vi) is the micrographs representing the composition of iron in the synthesized sample.

4.3.3 HRTEM
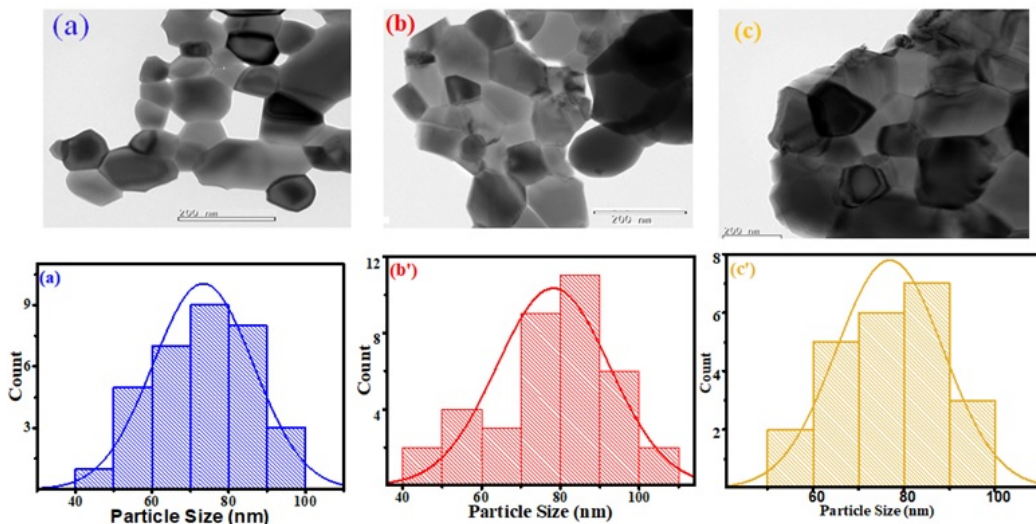
Figure 4.7: HRTEM spectra of MgNi ferrite SNPs annealed at 1100°C and corresponding histograms

To obtain the particle size, lattice spacing and morphology of the synthesized samples of $Mg_xNi_{1-x}Fe_2O_4$ annealed at 1100°C ferrites were characterized by HRTEM. The HRTEM

micrographs and corresponding histograms of the $Mg_xNi_{1-x}Fe_2O_4$ are presented in figure 4.7. It is clearly seen from the micrographs that the particles are homogeneously distributed and are separated with sharp edges. The micrographs for all the three compositions shows some agglomeration in nanoparticles which are attributed to their respective magnetic nature [43]. The micrographs also confirm the nano size of the synthesized particles.
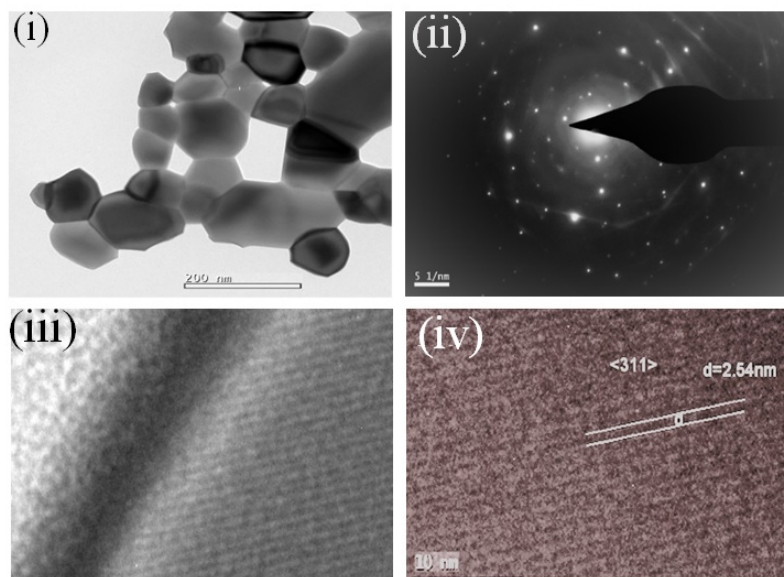
Figure 4.8: HRTEM image of MgNi ferrite SNPs annealed at 1100°C, (a1) Lattice planes in SAED pattern and (a2) lattice spacing from HRTEM image

Table 4.3: lattice spacing values measured from HRTEM image of MgNi ferrite SNPs annealed at 1100°C

Ring	lattice spacing (dhkl) Calculated from SAED TEM Image	lattice spacing (dhkl) Calculated from (W-H) XRD analysis	Plane < h k l >
R1	2.769	2.937	220
R2	2.518	2.535	311
R3	1.832	2.078	400
R4	1.637	1.697	422
R5	1.494	1.6	511
R6	1.388	1.47	440
R7	1.288	1.315	640
R8	1.192	1.268	533

The particles are observed as the uniform grains visible in these HRTEM micrographs without any impurity. Moreover, this further confirms their crystalline structure which are in great agreement with the results of the XRD studies [43]. The size of particles obtained from HRTEM images are also in agreement with that obtained from FESEM and as well

as the data obtained from W-H/XRD analysis. The values of lattice spacing related to each ring was measured with ImageJ software and are mentioned in the table 4.3 along with the lattice spacing values obtained from XRD analysis corresponding to each plane for the same sample.
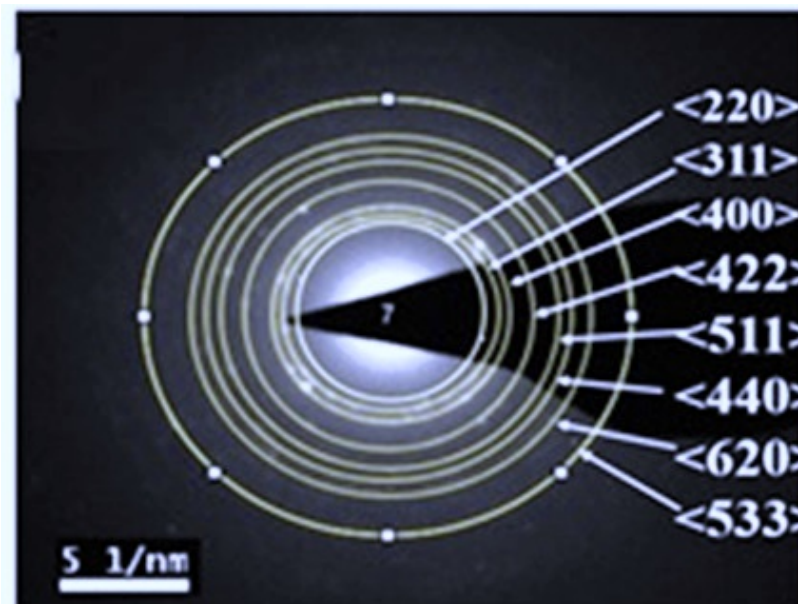
Figure 4.9: Identification of rings and lattice spacing measurement of MgNi ferrite SNPs annealed at 1100°C

For $Mg_{0.1875}Ni_{0.8125}Fe_2O_4$ samples, diffraction patterns of <220>, <311>, <400>, <422>, <511>, <440>, <620> and <533> planes were observed by selected area electron diffraction (SAED) and presented in figure 4.9. It is observed from the table 4.3 that lattice spacing values measured from TEM images strongly agrees with the values obtained from XRD analysis. The lattice spacing of the synthesized materials was also investigated with HR-TEM analysis given in figure 4.8. The measured lattice spacing was 2.54 nm for <311> plane which provides further confirmation from SAED analysis.

4.3.4 FTIR SPECTROSCOPY

FTIR plots of $Mg_xNi_{1-x}Fe_2O_4$ annealed at 1100°C are shown in figure 4.10. It shows that very first two bands 431-438 cm^{-1} and 579-687 cm^{-1} correspond to the octahedral and the tetrahedral sites respectively. Further it also confirms the formation of single phase cubic spinel nanoparticles. Variations in the cation-oxygen (A-O) bond lengths can cause variations in the band positions of MgNi ferrite [172, 209]. Ferrites include four metal-oxide ions (MO_4). Three of the linkages are octahedral oxide bonds (o-O), while fourth is a tetrahedral oxide link (τ-O). The three oxide ions will vibrate in any direction with consistent frequencies in this isotropic zone only if there are no tetrahedral connections in the area.

55

However, tetrahedral bonds are present and they enhance the frequency of vibrations (ν_τ) along the τ-O axis greatly. The frequency of vibration (ν_o) vary (increase or decrease) only if bending force constants are perpendicular to the τ-O axis [172] .
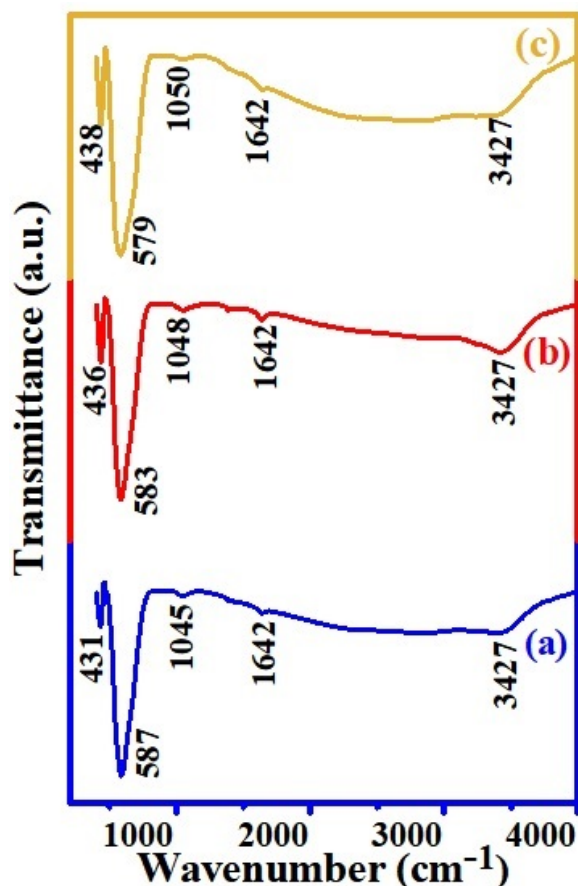
Figure 4.10: FTIR plots of MgNi ferrite SNPs annealed at 1100°C

Further when IR radiation impinge on the ferrite, the τ-O and o-O bonds absorb their distinctive energy radiations and oscillate. There are two types of oscillations they may have;

i.) Oscillation along the metal-oxide bond axis;

ii) Oscillation in the M-O bond's perpendicular direction.

The oxide ions only travel along the τ-O axis when vibrations occur along the M-O axis, resulting in linear force constants. However, when oxide ions vibrate perpendicularly to the M-O axis, a bending-like condition occurs, in which the oscillating oxide ion bends the o-O bond about its mean direction, resulting in bending force constants. The isotropic force field environments surrounding metal ion complexes at tetrahedral or octahedral sites, (known as n_3 and n_4 modes) oscillate as well. These vibration modes (n_3) and (n_4) were not observed in the current study for any of the three compositions. The first primary band appears to be splitting in all the three compositions shown in figure 4.10 by the FTIR spectrum. The presence of Fe^{2+} ion in ferrites causes John-Teller distortion which causes the split-

56

ting [196]. The existence of Mg^{2+}- O^{2-} complexes may explain the high frequency bands around the octahedral site-B. The C=O stretching vibration characteristic peak for the material $Mg_xNi_{1-x}Fe_2O_4$ is located at 1633 cm^{-1} [195] for all three formulations [42, 195, 197] and may be due to the stretching of the O-H bond of water molecules absorbed by nanoparticles. The C-O group vibration modes are characterized by a band about 1027 -1050 cm^{-1}, while a band representing -CH$_3$ bending around 1383 cm^{-1} is almost absent [195].

4.3.5 RAMAN SPECTRA

The spinel unit cell comprises 56 atoms, yet the simplest primitive cell requires only 14 atoms. At k = 0, a group theory research predicts 42 vibrational modes in the spinels, 3 acoustic modes and 39 visual modes. In spinel ferrites, only five modes have been reported: $A_{1g} + E_g + 3T_{2g}$. The three Raman active T_{2g} modes are T_{2g} (1), T_{2g} (2), and T_{2g} (3) denoting the lowest Raman shift and $T_{2g}(3)$ denotes the Raman T_{2g} symmetry mode at the highest wavenumber [198]. Raman spectra of these MgNi ferrite nanoparticles observed in 200-800 cm^{-1} range is presented in figure 4.11. Table 4.4 shows the characteristic bands observed in magnesium nickel ferrite samples which are are in good agreement with the FTIR results and other recorded values from literature [195].
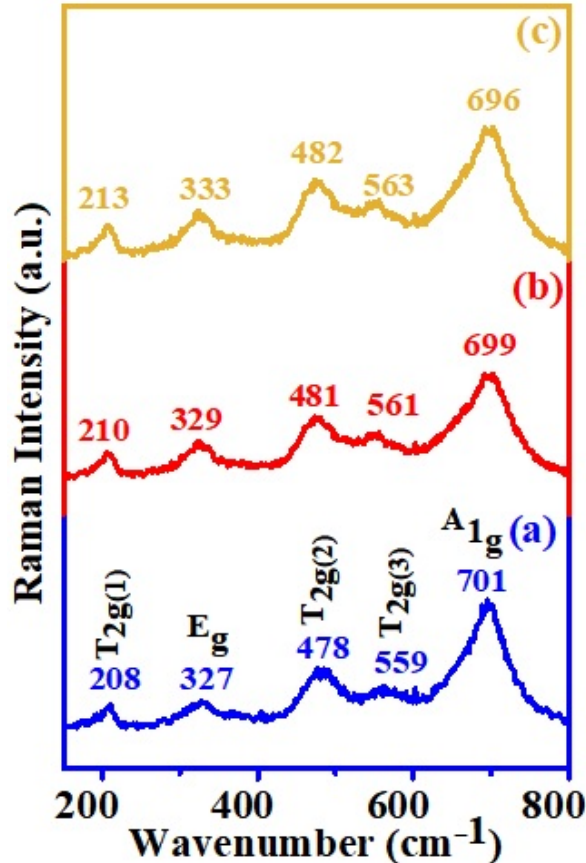
Figure 4.11: Raman plots of MgNi ferrite SNPs annealed at 1100°C

In the AB_2O_4 inverse spinel structure of ferrites, the broad band about 464 - 482 cm^{-1} for all three samples is allocated to tetrahedral (Fe^{3+}) at site-A and octahedral (Mg^{2+}, Ni^{2+}, Fe^{3+}) at site-B respectively [195, 197]. Table 4.4 shows the various Raman modes corresponding to these three samples.

Table 4.4: The variation of different Raman modes of MgNi ferrite SNPs annealed at 1100°C

Assignment	Origin of Mode	Raman Modes (cm^{-1})		
		(a) 0.1875	(b) 0.4375	(c) 0.8125
$T_{2g}(1)$	"The symmetric bending of oxygen atom with respect to the metal ion in AO_4 unit"	208	210	213
E_g	"Due to the asymmetric bending of oxygen"	327	329	333
$T_{2g}(2)$	"Due to asymmetric stretching of (Fe/Ni)O bond"	478	481	482
$T_{2g}(3)$	"Attributed to the translational movement of the tetrahedron (metal ion at tetrahedral site together with four oxygen atoms)"	559	561	563
A_{1g}	"Assigned as the symmetric breathing mode of the AO_4 unit with spinel lattice (highest frequency)"	701	699	696

4.3.6 MAGNETIC CHARACTERIZATION

The magnetic properties of $Mg_xNi_{1-x}Fe_2O_4$ were investigated using a VSM at room temperature and the hysteresis loops plotted are shown in figure 4.12. Table 4.5 present the data of the magnetic parameters *viz:* saturation magnetization (M_S), retentivity (M_R), coercivity (H_C) and squareness ratio (M_R/M_S). The magnetization of spinel ferrite material is greatly influenced by the super-exchange interaction between magnetic ions at the site-B and site-A. The spinel system's net magnetic moment is the difference between the magnetic moments of the site-B and site-A [210]. The Mg^{2+}, Ni^{2+} and Fe^{3+} ions have standard magnetic moment values of 0BM, $2\sqrt{2}$BM and 6 BM respectively. The obtained value of M_S and the magnetic moment (μ_B) were calculated for $Mg_xNi_{1-x}Fe_2O_4$ using equation 2.12 and are shown in table 4.5 [211].

It is found that M_S, M_R and H_C all decreased with the increase in Mg^{2+} ions composition [170, 199]. When Mg^{2+} ions composition increases, these non-magnetic Mg^{2+} ions replace magnetic Ni^{2+} ions from the site-B thereby decreasing the magnetic moment of site-B. Hence, the net magnetic moment of the crystallite decreases. The decrease in value of H_C with increase in Mg^{2+} ions composition is attributed to increase in particle size. This is because, large particle size pave less resistance to demagnetize a particle which is called coercivity [162]. It is also clear from the table 4.5 that the value of ratio of M_R to M_s lies in the range of 0 to 0.5 indicating the magneto static interaction between the prepared
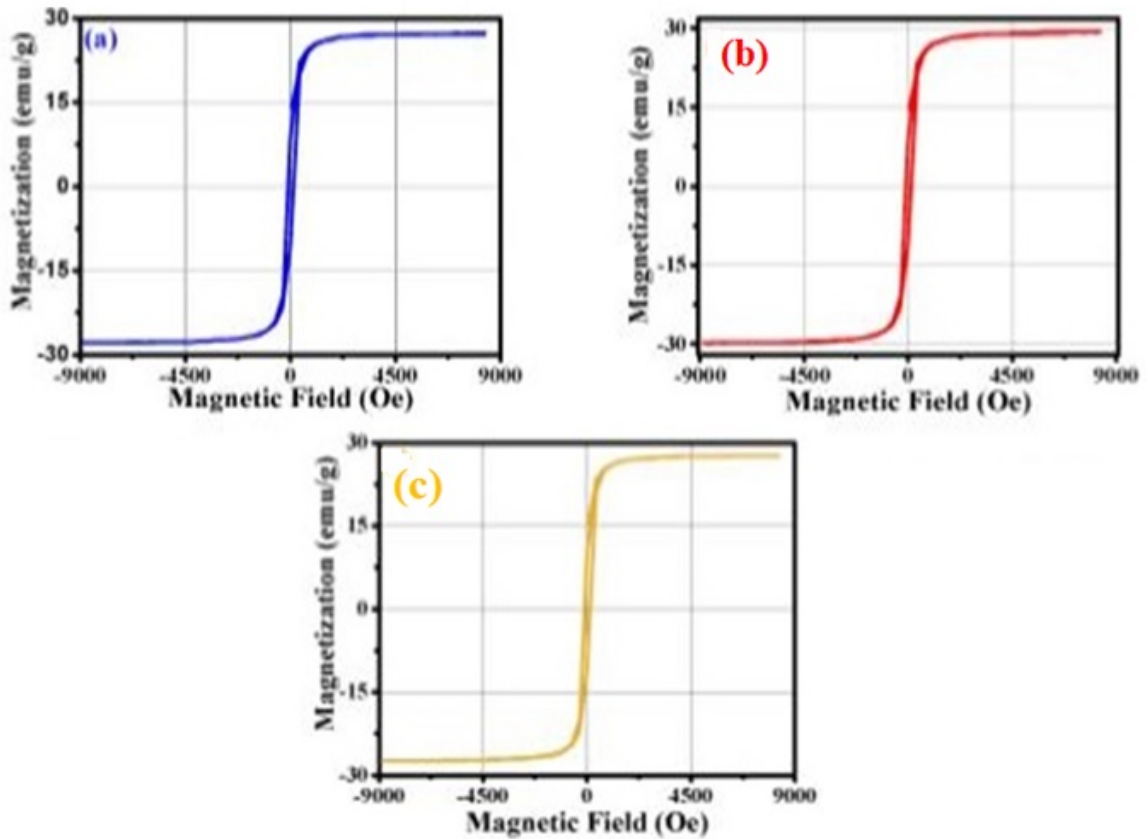
Figure 4.12: Hysteresis loops of MgNi ferrite SNPs annealed at 1100°C at room temperature (300K)

Table 4.5: Values of M_S, H_C, M_R, μ_B, M_R/M_S and anisotropy constant K of MgNi ferrites annealed at 1100°C

x(mol.frac.)	M_S (emu/g)	μ_B (emu/g)	M_R (emu/g)	Hc(Oe)	M_R/M_S	K (erg/cm3
0.1875	28.45	1.16	9.91	115	0.3483	3408
0.4375	27.41	1.08	9.45	110	0.3448	3141
0.8125	27.22	0.01	9.33	1.01	0.3428	2977

nanoparticles. Moreover, these particles also exhibit superparamagntic nature. The decrease in magneto crystalline anisotropy energy (K) value with increase in Mg^{2+} ions composition is again attributed to increase in particle size. This is because large paricle size pave less magnetocrystalline anisotropy. The value of K is obtained using relation 2.11 [112, 212] and is also presented in table 4.5.

Thus the afore mentioned data reveal that all synthesized powder samples are magnetically soft, with the high saturation magnetization value. Finally it is suggested that synthesized nanoparticles could be used as an EMI shielding material [196].

4.3.7 UV-VIS SPECTROSCOPY
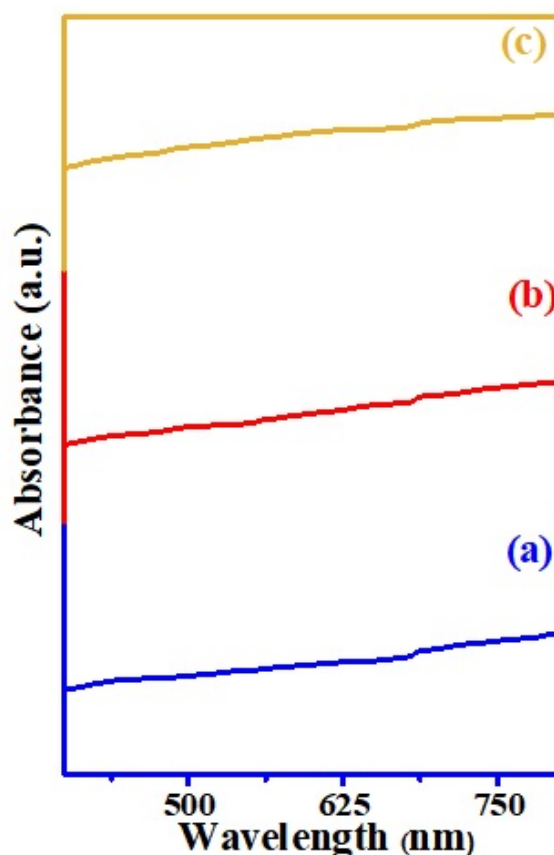
Figure 4.13: The UV-Vis plots for MgNi ferrite SNPs annealed at 1100°C

The optical properties of the magnesium nickel ferrite nanoparticles of $Mg_xNi_{1-x}Fe_2O_4$, x= (a) 0.1875-0, (b) 0.4375 and (c) 0.8125 nanoparticles synthesized by sol-gel method were studied by UV-Vis spectrophotometer (Model: V670 Jasco, International) in the wavelength range 200 nm to 800 nm. Figure 4.13 reveals the absence of absorption band edges in the wavelength range 200 nm to 800 nm confirming the synthesized materials do have very high optical band gap. Thus the synthesized nano materials are insulators. The electrical properties of ferrite nanoparticles are indeed related to the variation of their energy band gap. As a result, the band gap is a critical parameter in determining the electrical conductivity of materials. Due to the fact that the energy band gap in ferrites is compared to that of semiconductor materials, enable them significantly operate at higher temperatures under normal conditions [205].

4.4 CONCLUSION

This study demonstrated the structural, morphological, optical and magnetic properties of $Mg_xNi_{1-x}Fe_2O_4$ with x = (a) 0.1875, (b) 0.4375 and (c) 0.8125 synthesized via the sol-gel

route and annealed at 1100°C. XRD analysis revealed that all three samples have a spinel cubic structure with single phase. The secondary hematite phase (α-Fe$_2$O$_3$) is found absent for all the samples. Since Mg^{2+} ions have greater ionic radii than Ni^{2+} ions, the particle size (D) increases with Mg^{2+} ion composition. The presence of tensile strain in all prepared nanoparticles is indicated by the positive slope of linear W-H plots. FESEM was used to investigate how Mg^{2+} increases the crystalline of prepared samples. All elements present in the samples investigated by FESEM and EDAX. The samples were found to be in stoichiometric ratio, according to an EDX analysis. The HRTEM analysis reveals that these SNPs are in nano-metre range and have spinel cubic structure. The lattice plane and d-pacing acquired from TEM images, as well as SAED patterns, are quite close to the values obtained from XRD analysis. According to VSM analysis, the saturation magnetization (M$_S$) decreases with Mg^{2+} ion composition. The VSM results shows that the synthesized materials are soft magnetic materials and exhibit superparamagnetic nature. The experimentally obtained findings are in strong agreement with the theoretically determined structural and magnetic parameters from proposed cations distribution models. Thus these materials may be beneficial in EMI shielding due to their single phase spinel cubic structure and higher saturation magnetization (M$_S$).

CHAPTER 5

COMPARISION OF STRUCTURAL, MAGNETIC AND ELASTIC PROPERTIES OF MgNi FERRITE NANOPARTICLES ANNEALED AT 900°C & 1100°C TEMPERATURES

5.1 INTRODUCTION

The demand of technologically advanced SNPs is growing very fast. This demand paved the large market opportunity in all parts of the world in various fields such as magnetic storage devices, recording media, telecasting, telecommunication and many more [208]. These SNPs provide their outstanding electrical, magnetic, optical and catalytic properties in medical and other industries. Industry sector has the option to develop the product with these SNPs by altering their characteristic properties such as magnetic, optical and electrical [213]. Researches have shown that these goals are often achieved by altering the crucial factors like size of the ferrite particles, cation distribution of metal ions and the temperature of the manufacturing process or annealing [214]. The other major benefits of synthesizing these ferrites at different annealing temperature is to develop the SNPs for application in devices operating at higher temperature essentially required to know their elastic properties and stability at different temperatures. The density of states and band structure of these synthesized nanoparticles annealed at two different temperatures can be investigated using first principal calculations to have energetically more favorable material [36]. $Mg_xNi_{1-x}Fe_2O_4$ were synthesized via sol-gel route and annealed at two different temperatures 900°C and 1100°C respectively. Therefore, in the present chapter a comparative study of various parameters of these SNPs like structural, magnetic and elastic properties were estimated. Various analysis were carried out like morphological, structural and functional, elastic parameters *viz:* elastic velocity, elastic constants and their compliances, Young's modulus, shear modulus, Bulk's modulus, Poisson's ratio and Debye temperature. Various models were implemented such as Uniform Deformation Model (UDM), Uniform Stress Deformation Model (USDM) and Uniform Energy Deformation Model (UEDM) to estimate and address various parameters. Moreover, on the basis of detailed comparative interpretation for the prepared magnetic nanoferrites, magnetic properties such as magnetic saturation, remanant field, coercivity,

magnetic moment, squareness ratio, anisotropy constant, susceptibility [24, 54] and other allied parameters were studied.

5.2 EXPERIMENTAL DETAILS

5.2.1 SYNTHESIS

The proposed material in the present study *i.e.* $Mg_xNi_{1-x}Fe_2O_4$ was synthesized via aqueous sol-gel route [26]. The synthesized SNPs were annealed at two different temperatures *i.e.* 900°C and 1100°C. The synthesis procedure of these nanoparticles has already been discussed in chapter 3, section 3.2.1 for the material annealed at 900°C and section 4.2.1 at 1100°C [167].

5.2.2 CHARACTERIZATION

Both the sets of prepared nano materials are subjected to the similar characterizations to sudy the structural, morphological, optical and magnetic properties already been discussed in section 3.2.2 of chapter 3 for the NPs annealed at 900°C and in section 4.2.2 of chapter 4 for the material annealed at 1100°C.

5.3 RESULTS AND DISCUSSIONS

5.3.1 X-RAY DIFFRACTION ANALYSIS

The XRD patterns of $Mg_xNi_{1-x}Fe_2O_4$ nanoparticles annealed at 900°C is presented in figure 3.1 and for the materials annealed at 1100°C is presented in figure 4.1. The nanostructure formation of the prepared samples annealed at 900°C and 1100°C have been verified with the standard data of magnesium doped nickel ferrite [19] JCPDS data card No. 10-325, 86-2267 and 74-2081 [20]. It has been revealed from the XRD patterns that the synthesized Mg-Ni-Ferrite nanoparticles contains no impurity peaks, as found earlier in the similar material synthesized through solid state route [23]. The values of 2θ, normalized peak value, FWHM (β), crystallite size from Scherer's formula (D), lattice spacing (d), lattice plane <hkl>, lattice parameter (a) and lattice strainn (ϵ) for all three compositions of $Mg_xNi_{1-x}Fe_2O_4$ nanoparticles annealed at 900°C and 1100°C are shown in table 5.1.

The lattice parameter (a) is found in the range of 8.31 Å to 8.34 Å for the SNPs annealed at 900°C whereas it varies from 8.32 Å to 8.34 Å for SNPs annealed at 1100°C which are in line with the previously obtained results for the similar composition annealed at 500°C [182]. The disparity in lattice parameter values is due to difference in annealing temperature. The crystal structural parametric values *viz:* most abundant peak intensity, crystallite size

Table 5.1: The values of 2θ, normalized peak values, (FWHM) (β), crytallite size (D), lattice spacing (d), lattice plane <hkl>, lattice parameter (a) and lattice strainn (ε) of MgNi ferrite SNPs annealed at 900°C and 1100°C

Composition	Annealed at 900°C								Annealed at 1100°C							
	2θ (Degree)	Norm. Peak Value	FWHM (β) (Degree)	Cryst. Size (D) (nm)	Lattice Spacing (d_obs) (nm)	Lattice Plane <hkl>	Lattice Constant (a)(Å)	Strain (ε) (x10⁻⁴)	2θ (Degree)	Norm. Peak Value	FWHM (β) (Degree)	Cryst. Size (D) (nm)	Lattice Spacing (d_obs) (nm)	Lattice Plane <hkl>	Lattice Constant (a)(Å)	Strain (ε) (x10⁻⁴)
(a)Mg$_{0.1875}$Ni$_{0.8125}$Fe$_2$O$_4$	18.46	5.92	0.131	61.27	4.80	111	8.32	5.66	18.51	7.01	0.115	69.87	4.79	111	8.30	5.00
	30.41	33.53	0.154	53.47	2.94	220	8.31	6.48	30.41	33.61	0.119	69.4	2.94	220	8.31	5.00
	35.78	100	0.372	22.41	2.51	311	8.32	15.50	35.81	100	0.139	60.2	2.51	311	8.31	5.75
	37.45	5.14	0.183	45.87	2.40	222	8.31	7.56	37.47	6.40	0.089	94.43	2.40	222	8.31	3.75
	43.52	22.11	0.393	21.77	2.08	400	8.31	15.90	43.52	21.71	0.142	60.18	2.08	400	8.31	5.75
	53.97	8.50	0.199	44.89	1.70	422	8.32	7.72	54	9.97	0.134	66.20	1.70	422	8.31	5.25
	57.54	28.39	0.163	55.44	1.60	511	8.32	6.25	57.55	28.56	0.13	69.98	1.60	511	8.31	5.00
	63.18	36	0.193	48.43	1.47	440	8.32	7.16	63.2	34.79	0.155	60.28	1.47	440	8.32	5.75
	71.70	3.86	0.144	67.99	1.32	620	8.32	5.10	71.73	3.35	0.108	90.98	1.31	620	8.32	3.75
	74.75	7.37	0.35	28.57	1.27	533	8.32	12.10	74.8	6.17	0.129	77.55	1.27	533	8.32	4.50
(b)Mg$_{0.4375}$Ni$_{0.5625}$Fe$_2$O$_4$	18.46	6.72	0.103	78.16	4.79	111	8.31	4.43	18.46	5.23	0.117	68.74	4.80	111	8.31	5.04
	30.39	32.85	0.164	50.22	2.94	220	8.31	6.90	30.34	30.41	0.127	64.55	2.94	220	8.32	5.37
	35.71	100	0.203	41.03	2.51	311	8.31	8.45	35.73	100	0.11	75.69	2.51	311	8.31	4.58
	37.44	3.27	0.214	39.23	2.40	222	8.31	8.83	37.39	1.44	0.086	97.46	2.40	222	8.31	3.56
	43.46	20.54	0.175	48.89	2.08	400	8.31	7.09	43.43	18.6	0.112	76.16	2.08	400	8.32	4.55
	53.92	9.73	0.169	52.71	1.70	422	8.31	6.58	53.89	7.44	0.13	68.72	1.70	422	8.33	5.04
	57.47	26.41	0.206	43.99	1.60	511	8.31	7.88	57.45	24.18	0.116	78.35	1.60	511	8.32	4.42
	63.13	36.73	0.201	46.26	1.47	440	8.32	7.49	63.10	33.18	0.127	73.22	1.47	440	8.32	4.73
	71.63	1.33	0.337	29.04	1.31	620	8.32	11.9	71.54	1.49	0.103	95.27	1.32	620	8.35	3.64
	74.73	6.67	0.263	38.01	1.27	533	8.32	9.12	74.69	6.10	0.102	97.71	1.27	533	8.32	3.55
(c)Mg$_{0.8125}$Ni$_{0.1875}$Fe$_2$O$_4$	18.47	7.19	0.169	47.72	4.80	111	8.31	7.25	18.44	6.51	0.088	91.71	4.81	111	8.33	3.78
	30.35	32.6	0.211	38.94	2.94	220	8.32	9.00	30.31	34.02	0.112	73.77	2.95	220	8.34	4.70
	35.74	100	0.224	37.33	2.51	311	8.33	9.25	35.7	100	0.124	67.53	2.51	311	8.33	5.13
	37.36	3.22	0.184	45.53	2.40	222	8.33	7.50	37.35	3.16	0.063	133.3	2.41	222	8.34	2.60
	43.42	20.00	0.249	34.37	2.08	400	8.33	10	43.38	14.28	0.148	57.57	2.08	400	8.32	6.02
	53.92	7.69	0.186	48.03	1.70	422	8.32	7.25	53.82	8.60	0.106	83.88	1.70	422	8.33	4.13
	57.41	25.40	0.285	31.72	1.60	511	8.33	11	57.37	41.95	0.14	64.46	1.60	511	8.31	5.38
	63.05	35.30	0.332	28.04	1.47	440	8.33	12.30	63.01	32.75	0.152	61.26	1.47	440	8.32	5.66
	71.55	2.03	0.382	25.61	1.32	620	8.33	13.50	71.50	3.49	0.075	129.70	1.32	620	8.34	2.67
	74.6	7.44	0.379	26.33	1.27	533	8.34	13.30	74.55	6.08	0.078	127.9	1.27	533	8.33	2.71

(calculated from W-H analysis), crystal lattice spacing (d), lattice constant (*a*) and strain (ϵ_{RMS}) are listed in table 3.1 for all the three compositions of $Mg_xNi_{1-x}Fe_2O_4$.

Table 5.2: Important parameters of MgNi ferrite SNPs obtained using Rietveld refinement analysis

| Sample | Annealing temperature of 900°C | | | | | Annealing temperature of 1100°C | | | | |
	Lattice parameter (a) Å	Cell volume $(a^3)Å^3$	R_B	R_F	χ^2	Lattice parameter (a) Å	Cell volume $(a^3)Å^3$	R_B	R_F	χ^2
(a)	8.3267	577.32	2.57	1.68	1.20	8.3215	576.24	6.46	2.30	2.84
(b)	8.3364	579.34	2.49	1.90	1.33	8.3086	573.57	6.31	2.18	2.72
(c)	8.3436	580.85	6.07	1.70	1.35	8.3412	580.34	6.21	2.21	2.83

The XRD data of all the three compositions of $Mg_xNi_{1-x}Fe_2O_4$ (SNPs) have been refined for Rietveld refinement using Fullprof suit software and presented in figure 5.1.

In these synthesized ferrites, the lattice parameter (*a*) determined through Rietveld refinement corresponds well with the values calculated from XRD. For all spinel cubic ferrites with the space group of Fd-3m, the experimental data is well matched with the revised data points. For all of the samples, the goodness of fit (GOF) value was found to be very close to 1, indicating good fitting of data points [215]. The presence of any form of contaminant in the produced nanostructures was ruled out by Rietveld refinement analysis. The value of χ^2 in the Rietveld data is observed close to 1 further indicates the excellent fit with the experimental data. The results of the Rietveld refinement analysis are shown in table 5.2. After fitting, all of the results lead to the synthesis of defect-free ferrite nanoparticles [112, 167]. The comparative values of structural parameters for $Mg_{0.1875}Ni_{0.8125}Fe_2O_4$ SNPs annealed at (a) 900°C and (b) 1100°C obtained from X-Ray Diffraction and Rietveld refinement are mentioned in table 5.3.

The particle sizes of prepared SNPs as calculated from the most prominent peak (311) for $Mg_xNi_{1-x}Fe_2O_4$ annealed at 900°C ranges from 35 nm to 61 nm (table 3.1) and 66 nm to 94 nm for the same material annealed at 1100°C (table 4.1) confirms the nano range of prepared SNPs. The size of synthesized nanoparticles was found to be increased when annealed at 1100°C as compared to particles annealed at 900°C, may be attributed for increase in the values of lattice parameter and lattice spacing when the same material precursor annealed at higher temperature 1100°C. The value of ϵ_{RMS} for nanoparticles annealed at 900°C and 1100° C are 12.9×10^{-04} to 5.2×10^{-04} respectively indicating that the atoms have more access to fit in their most preferable position in the lattice during the nucleation process and have less value of strain. The value of strain may be positive or negative [25]. Compressive stress causes negative strain, while tensile tension causes positive strain. The strain discovered in this investigation is positive and is termed as tensile strain responsible for lattice expansion.
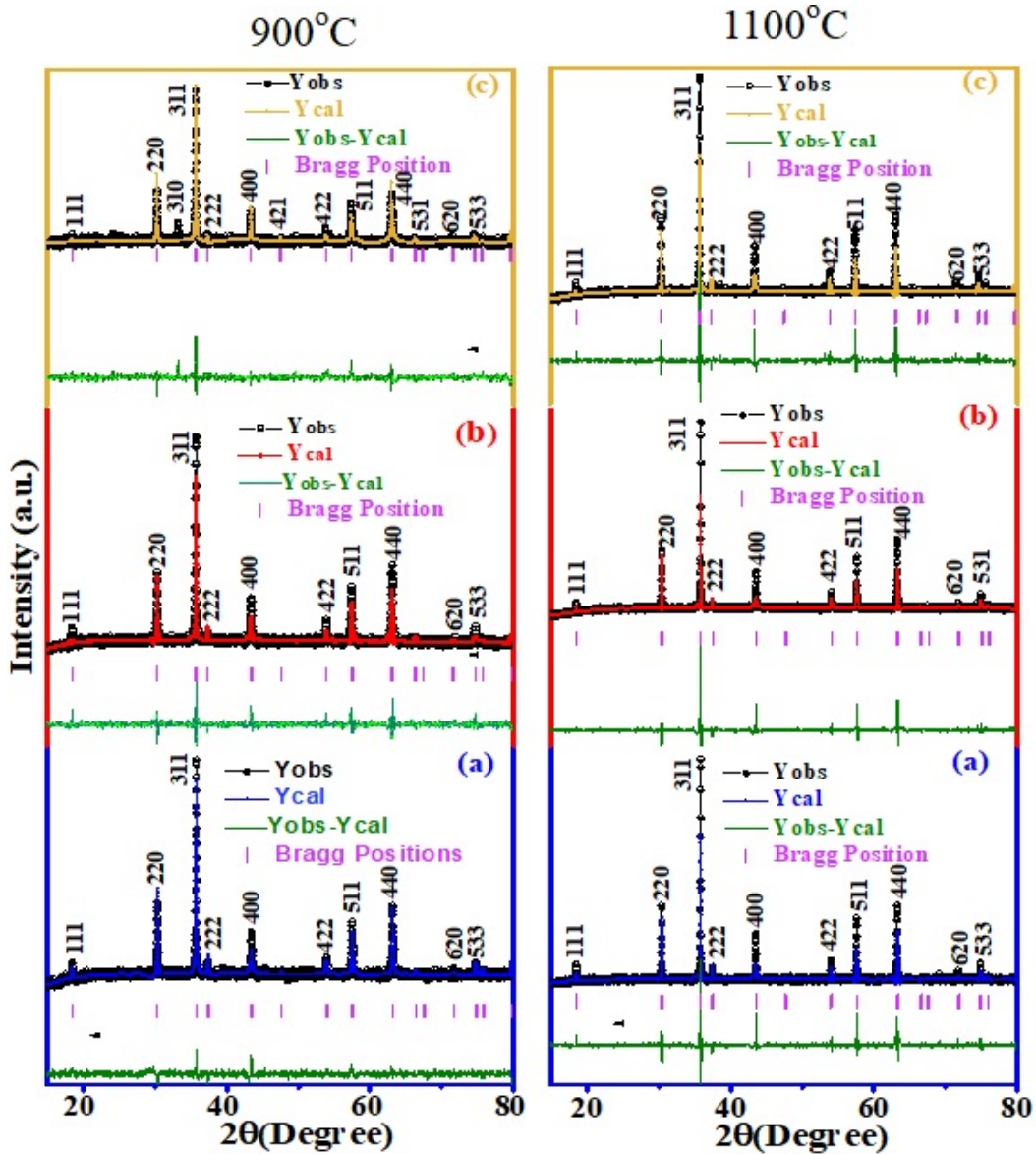
Figure 5.1: Reitveld ftted XRD profles of MgNi ferrite SNPs annealed at 900°C and at 1100°C

This hypothesis is supported by the findings in investigations of the current research. Furthermore, several essential structural characteristics may be computed using XRD results [26] of noncrystalline Mg-Ni- ferrite annealed at 900°C and 1100°C using the equation 2.1 - equation 2.9 described in chapter 2.

The crystal structure of the ferrite nano material $Mg_{0.8125}Ni_{0.1875}Fe_2O_4$ annealed at 1100 °C is drawn with the help of "vesta" software using Rietveld refinement data is presented in figure 5.2.

The theoretical x-ray density (ρ_x) was estimated using equation 2.6 the bulk density (ρ) was determined using equation 2.7 and the pore fraction (f) was calculated using equation 2.8. The values of these parameters are mentioned in the table 5.4 for both the sets of annealed samples. The results are quite similar to those obtained at an annealing tempera-

Table 5.3: Structural parameters of MgNi ferrite SNPs annealed at 900°C and 1100°C obtained from XRD and Rietveld refinement

Annealing Temp.	900°C						1100°C					
Sample	(a) 0.1875		(b) 0.4375		(c) 0.8125		(a) 0.1875		(b) 0.4375		(c) 0.8125	
	XRD	Rietveld	XRD	Rietveld	XRD	Rietveld	XRD	Rietveld	XRD	Rietveld	XRD	Rietveld
Lattice Parameter (Å)	8.31	8.32	8.33	8.34	8.34	8.34	8.32	8.32	8.33	8.34	8.34	8.34
Unit Cell Volume (Å³)	574	578	578	580	580	580	576	576	578	580	580	580
Crystallite Size D (nm)	35	-	48	-	61	-	66	-	91	-	94	-
Specific Area (S) m²/g	32.49	-	24.71	-	20.81	-	17.29	-	12.6	-	11.58	-
Disloc Density (d) x10^{16} lines/m²	21.9	-	14.2	-	9.81	-	4.58	-	2.81	-	2.53	-
a_{th}	8.35	8.35	8.35	8.36	8.37	8.37	8.35	8.35	8.35	8.36	8.37	8.37
a_{Exp}	8.31	8.32	8.33	8.34	8.34	8.34	8.32	8.32	8.33	8.34	8.34	8.34
u_{lit}	0.375	0.375	0.375	0.375	0.375	0.375	0.375	0.375	0.38	0.375	0.375	0.375
u_{Th}	0.3794	0.3794	0.3792	0.3792	0.379	0.379	0.379	0.3794	0.38	0.3795	0.379	0.379
u_{exp}	0.3799	0.3798	0.3796	0.3795	0.3795	0.3795	0.38	0.3797	0.38	0.3795	0.3795	0.3794
	0.0044	0.0044	0.0042	0.0042	0.004	0.004	0.004	0.0044	0	0.0045	0.004	0.004
d_{AL}	1.8697	1.8705	1.8699	1.8707	1.8707	1.8707	1.878	1.8694	1.87	1.8704	1.8707	1.8695
d_{BL}	2.0376	2.0408	2.0449	2.0482	2.0482	2.0482	2.047	2.042	2.05	2.0478	2.0559	2.0493
d_{AES}	3.0532	3.0545	3.0535	3.0548	3.0548	3.0548	3.054	3.0527	3.05	3.0543	3.0548	3.0529
d_{BES}	2.8229	2.8286	2.8367	2.8425	2.8425	2.8425	2.823	2.8315	2.83	2.842	2.8425	2.8453
d_{BEU}	2.9392	2.9426	2.9461	2.9496	2.9608	2.9496	2.952	2.9431	2.96	2.9491	2.9608	2.95
L_A	3.5983	3.6027	3.607	3.6113	3.6113	3.6113	3.599	3.6033	3.61	3.6107	3.6113	3.6118
L_B	2.938	2.9416	2.9451	2.9486	2.9486	2.9486	2.939	2.9421	2.94	2.9481	2.9486	2.9491
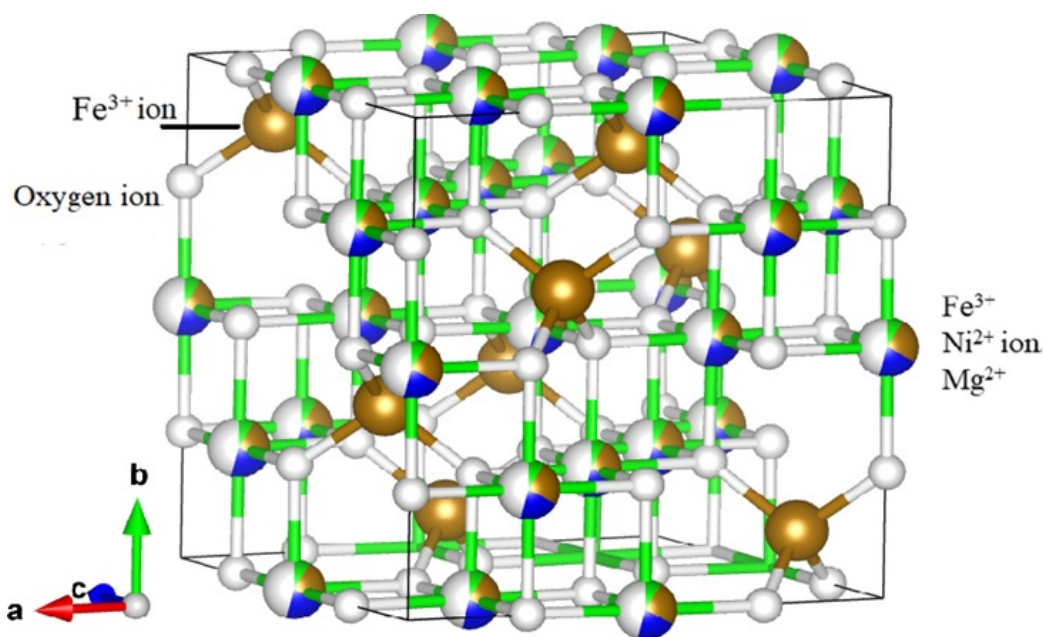
Figure 5.2: Crystal structure of $Mg_{0.8125}Ni_{0.1875}Fe_2O_4$ annealed at 1100°C

ture of 800 °C for a similar composition [28].

The Archemedes principle was used to calculate the bulk density. The values of bulk density (ρ) for noncrystalline $Mg_xNi_{1-x}Fe_2O_4$ powder at 1100°C annealing temperatures is higher in contrast to material annealed at 900°C. Due to a more systematic arrangement of atoms in the sample, the higher density of the sample at annealing temperature 1100 °C

Table 5.4: Values of X-ray density, bulk density and porosity of MgNi ferrite SNPs annealed at 900°C and 1100°C

	900 °C			**1100 °C**		
x (Mol. frac.)	X-Ray Density (ρ_x) Kg/m^3	Bulk Density (ρ) Kg/m^3	Porosity (P)	X-Ray Density (ρ_x) Kg/m^3	Bulk Density (ρ) Kg/m^3	Porosity (P)
0.1875	5268	4730	0.1021	5268	4920	0.0661
0.3125	5161	3740	0.2753	5260	4800	0.0875
0.4375	5074	3590	0.2925	5273	4610	0.1257
0.5625	4912	3290	0.3302	5207	4510	0.1339
0.1875	4783	3175	0.3362	5174	4370	0.1554
0.8125	4746	3080	0.351	5174	3680	0.2888

accounts for the higher degree of crystalline of the material [167]. These values are comparable to those obtained from a similar nanocrystalline ferrite powder synthesized via similar method. [26, 28]. The pore fraction values are high along with different bulk density values when compared to similar material synthesized using a different process [28]. Equation 2.9 - 2.10 are used to calculate the dislocation density (δ) and specific surface area (S) of spinel ferrites. The obtained values are mentioned in table 5.5.

The X-ray density and bulk density of the SNPs are also found to decrease with increasing Mg^{2+} ions composition for the samples annealed at 900°C and 1100°C as seen in table 5.4. This decrease in density is may be due to the large size of Mg^{2+} ions replacing the Ni^{2+} ions from site-B of crystal lattice. In the present study the observed experimental results agrees with theoretical concept.

The dislocation density (δ) for SNP's $Mg_xNi_{1-x}Fe_2O_4$ material is calculated using equation 2.9 for the materials annealed at 900°C and 1100°C and found to be 1.8 x 10^{14} and 9.2 x 10^{13} dislocation lines /m^2 respectively.

In comparison to other ferrites, these values of dislocation densities are very low [26, 29, 30] which shows that $Mg_xNi_{1-x}Fe_2O_4$ SNPs synthesized via sol-gel method have good degree of crystallanity. The data also show that the degree of crystallanity rises when synthesized at higher annealing temperatures, since dislocation density is lower in material annealed at 1100°C compared to 900°C.

The equation 2.10 was used to calculate specific surface area. The values of specific surface area and dislocation density for nanocrystalline $Mg_xNi_{1-x}Fe_2O_4$ are given in table 5.5 which is attributed to increase in particle size with increasing Mg^{2+} ion composition.

The table 5.1 shows the values of 2θ, β, particle size (D), lattice spacing (d) and lattice parameter a. However, the lattice parameter is found to be increasing with increasing Mg^{2+} ions attributed to large size of Mg^{2+} ions replacing comparatively smaller size Ni^{2+} ios from site-B of the ferrite lattice. Also lattice parameter and particle size increases with increase

in annealing temperature [167].

Table 5.5: Dislocation density & specific surface area of MgNi ferrite SNPs annealed at 900°C & 1100°C

Sample	900°C		1100°C	
	Dislocation Density (δ) ($\times 10^{13}$) lines/m^2	Specific Surface Area m^2/g	Dislocation Density (δ) ($\times 10^{14}$) lines/m^2	Specific Surface Area m^2/g
(a)	2.33	32.39	1.55	17.23
(b)	2.99	24.73	0.26	12.96
(c)	5.18	20.88	1.98	12.31

5.3.2 CATION DISTRIBUTION

In $Mg_xNi_{1-x}Fe_2O_4$, Magnesium (Mg) and Nickel (Ni) are non-transitional and transitional metals respectively [31–33]. The Mg^{2+} ions has strong tendency to occupy the octahedral site-B. Since Ni^{2+} ions have d^8 electronic configuration and has large value of legand field stabilization energy (LFSE) for octahedral site-B, they also occupy octahedral site-B [38, 66, 216]. Fe^{3+} ions are pushed from the octahedral site-B to the tetrahedral site-A by both the Mg^{2+} and Ni^{2+} ions . However, Fe^{3+} ions with a d^5 electronic configuration can occupy any lattice site [33, 34, 38, 39]. Therefore, Fe^{3+} ions occupied both octahedral site-B and tetrahedral site-A. As a result, the examined material should have the inverse spinel structure [31, 38, 40]. Equation 2.14 presents the cation distribution for this material. The theoretical values of ionic radii of tetrahedral site-A and octahedral site-B have been derived using the equation 2.15 & equation 2.16.

At octahedral site-B, the value of r $^{(Ni2+)}$ of Ni^{2+} ions is 0.69Å, r $^{(Mg2+)}$ is 0.72Å, ionic radii r (Fe^{3+}) at tetrahedral site-A is 0.49Å and Fe^{3+} ions have ionic radii r$^{(Fe^{3+})}$ at octahedral site-A is 0.67Å. The ionic radii of the oxygen ion O^{2-} have been taken as 0.138Å[169, 180].

5.3.3 MICROSTRUCTURAL PARAMETERS

The detailed study of the structural information has been carried out by obtaining the microstructural parameters. The combined impact of crystallite size (β_D) and crystallite strain (β_ϵ) that causes the broadening of the XRD peaks is investigated to estimate the average crystallite size using Scherer's method, given by equation 2.20 and equation 2.21.The average crystallite size (D) is calculated by linear fitting of the Williamson-Hall plot using the relation 2.23 for $Mg_xNi_{1-x}Fe_2O_4$ ferrite nanoparticles annealed at 900°C & 1100°C respectively.

Williamson-Hall plots of the corresponding structures are shown in figure 5.3.
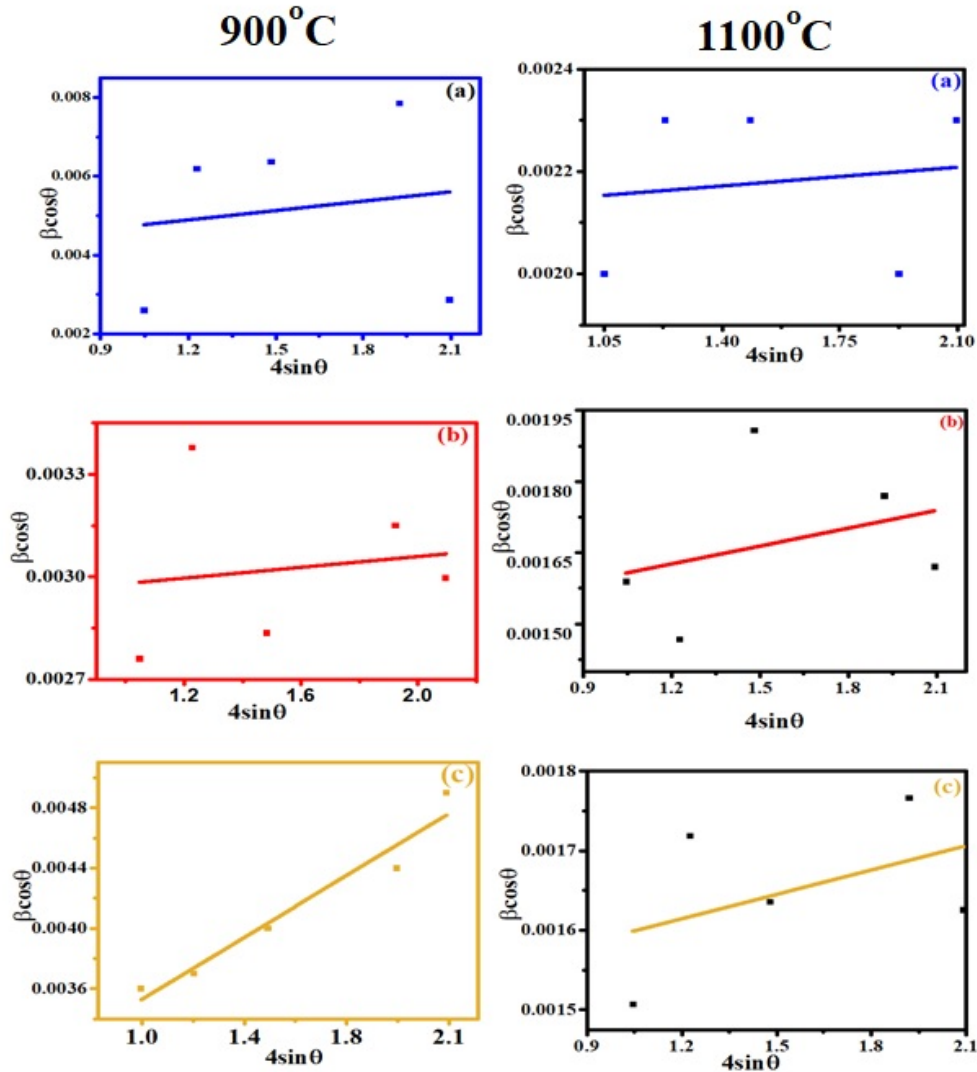
Figure 5.3: W-H plots of MgNi ferrite SNPs annealed at 900°C & 1100°C in UDM

From the figure 5.3 of W-H plots of MgNi ferrites nanoparticles the slope of the plots for both the samples was found to be positive indicating that during the annealing, the material is under the tensile strains which controls the crystallite size. The tensile strain of the ferrite particle annealed a 1100°C is greater than for the same composition annealed at 900°C (mentioned in the table 5.1).

5.3.4 RAMAN SPECTROSCOPY

Raman spectroscopy is a sensitive tool for observing the structural insight of material by investigating the phonon vibration of crystallite solids [217]. In the present study, Raman spectra is obtained for MgNi ferrites for all compositions synthesized at 900°C and 1100°C. Raman spectra of these MgNi ferrites is recorded in the range of 100 cm^{-1} - 800 cm^{-1} and

are presented in figure 3.10. Tables 3.5 and 4.4 show the characteristic bands observed for ferrite samples annealed at 900°C and 1100°C respectively, which are in good agreement with the published values [44,45,53, 218].

Table 5.6: Values of different Raman modes in MgNi ferrite SNPs annealed at 900°C and 1100°C

		Raman Modes (cm^{-1})					
	Annealing Temp.	**900**°C			**1100**°C		
Assignment	Origin of Mode	(a)	(b)	(c)	(a)	(b)	(c)
A$_{1g}$	Symmetric stretch of Oxygen atoms along Fe-O bonds	702	700	697	701	699	696
T$_{2g}$(1)	The symmetric bending of oxygen atom with respect to the metal ion in AO$_4$ unit	207	211	213	208	210	213
E$_g$	Due to the asymmetric bending of oxygen	329	330	233	327	329	333
T$_{2g}$(2)	Due to asymmetric stretching of (Fe/Ni/Mg)–O bond	479	481	483	478	481	482
T$_{2g}$(3)	Attributed to the translational movement of the tetrahedron (metal ion at tetrahedral site-B together with four oxygen atoms)	554	558	568	559	561	563

On comparison, it is clear from the table 5.6 that both the synthesized nano particles exhibit tetrahedral and octahedral bands hence got spinel structure. Also the observed bands in case of samples annealed at 1100°C suffers a blue shift as compared to the bands observed in case of samples prepared by 900°C annealing temperature. This may be attributed to more ordered structure of these ferrites at higher annealing temperature.

5.3.5   FTIR SPECTROSCOPY

The FTIR plots of MgNi ferrite SNPs are presented in figure 3.9 and figure 4.10 respectively. For material synthesized at two different annealing temperature, the various observed band positions are given in table 5.7 [15]. The band positions of various functional groups *viz:* presence of of C-O bond is observed at around 1045 cm^{-1}, -CH$_3$ bending is observed at around 1384 cm^{-1} for the material annealed at 900°C. However, this band is absent in the material when annealed at 1100°C and presence of C=O is observed at around 3430 cm^{-1} [15]. The tetrahedral band is around 583-568 cm^{-1} and 579-587 cm^{-1} for materials annealed at 900°C & 1100°C respectively. The octahedral band positions are found around 428-535 cm^{-1} and 431-438 cm^{-1} for materials annealed at 900°C & 1100°C respectively. The cations in MgNi ferrite are Fe^{3+} at tetrahedral site-A and Mg^{2+}, Ni^{2+}, Fe^{3+} at octahedral site-B.

Table 5.7: Various FTIR band positions of MgNi ferrite SNPs annealed at 900°C and 1100°C

		Band Position (cm^{-1})					
	Annealing Temperature	900°C			1100°C		
S.No.	Assignment	(a)	(b)	(c)	(a)	(b)	(c)
		0.1875	0.4375	0.8125	0.1875	0.4375	0.8125
1	Fe-O bond (Octahedral band)	428	432	435	431	436	438
2	Mg/Ni/Fe-O bond (Tetrahedral band)	583	578	568	587	583	579
3	Presence of C-O bond	1043	1050	1055	1045	1048	1050
4	-CH$_3$ bending	1383	1383	1384	-	-	-
5	Presence of C=O bond	1633	1633	1635	1642	1642	1642
6	-OH bond (Presence of water molecule)	3430	3430	3430	3427	3427	3427

Table 5.8: Elastic parameters from FTIR spectroscopy of MgNi ferrite SNPs annealed at 900°C & 1100°C

| Annealing Temperature | 900°C | | | 1100°C | | |
Composition (x)	0.1875	0.4375	0.8125	0.1875	0.4375	0.8125
Tetra. band position $\nu_1 \times 10^2$ (m^{-1})	583	578	568	587	583	579
Octa. band position $\nu_2 \times 10^2$ (m^{-1})	428	432	435	431	436	438
Tetra. force constant k$_\tau \times 10^2$ (Nm^{-1})	249	245	237	253	249	246
Octa. force constant k$_o \times 10^2$ (Nm^{-1})	151	151	151	153	155	152
Avg. force constant k$_{avg} \times 10^2$ (Nm^{-1})	200	198	194	203	202	199
Long. Elastic wave velocity v$_L$ (ms^{-1})	6752	6865	6708	6807	6787	6767
Trans. Elastic wave velocity v$_T$ (ms^{-1}))	4085	6218	7715	3867	4334	6129
Mean Elastic wave velocity v$_m$ (ms^{-1})	4515	6406	7448	4299	4763	6315
Mean atomic volume v$_A \times 10^{-6}$ (m^3)	6.18	6.18	6.21	6.19	5.94	5.65
Bulk modulus B (Gpa)	146	125	119	151	144	127
Rigidity modulus R (GPa)	71	84	85	70	74	84
Youngs modulus Y (GPa)	184	206	206	181	190	206
Poisson ratio	0.29	0.23	0.21	0.3	0.28	0.23
Debye temp. D (K)	463	462	459	466	466	466

From table 5.7 it is observed that tetrahedral band position show blue shift with increasing Mg^{2+} composition and annealing temperature whereas octahedral band position shows a red shift. With increasing Mg^{2+} composition, lattice parameter and particle size also increases which signifies that tetrahedral and octahedral bond lengths increase. Also the reduced mass of ions decreases at octahedral site-B. The band position is inversely proportional to bond length and reduce mass of ions at site-A. In the present case $Mg_xNi_{1-x}Fe_2O_4$ has inverse spinel structure therefore, increase in Mg^{2+} ions only decrease the reduce mass of site-B, because lighter Mg^{2+} ions replacing heavier Ni^{2+} ions at site-B. Therefore, it may be concluded that

1. In case of tetrahedral site-A, due to increase in τ-O bond length, band position shifts towards lower wave number *i.e.* blue shift.

2. In case of octahedral site-B, due to increase in o-O bond length, band position shifts towards lower wave number (blue shift) and due to decrease in reduced mass, band position shift towards higher wave number side *i.e.* (red shift). Here the later shift dominates the former resulting to net red shift in the band position .

Using the values of band positions from table 5.7 the values of the force constants K_τ and K_o are computed using equation 2.27 & 2.28 for all the three compositions of $Mg_xNi_{1-x}Fe_2O_4$ and are placed in table 5.8. It has been discovered that the value of K_τ is higher than the value of K_o. This is because the ionic radii of ions at tetrahedral site-A is less than that at octahedral site-B which means that the tetrahedral bond length is less than octahedral bond length and force constant is inversely proportional to the bond length.
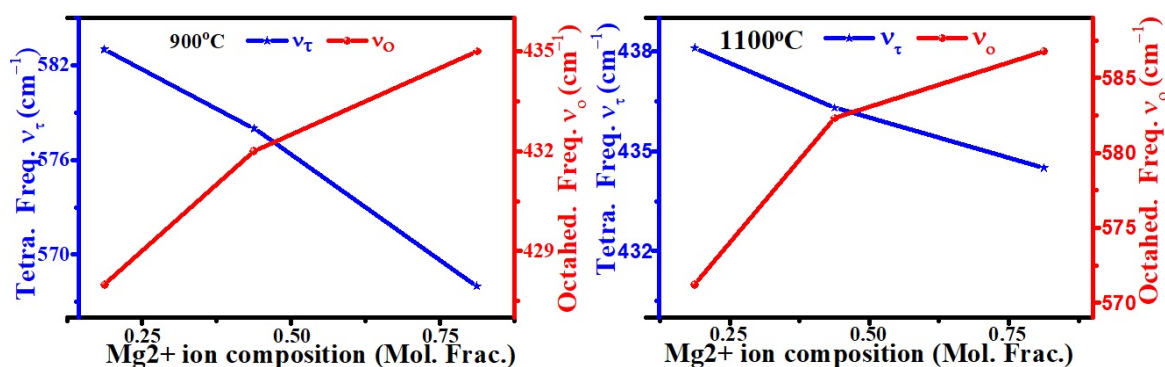
Figure 5.4: Values of tetrahedral and octahedral frequencies of MgNiFO annealed at 900°C and 1100°C at different compositions of Mg^{2+} ions

The variation in the values of force constants may be explained analogous to that explained in case of shift in tetrahedral and octahedral frequencies. [39]. The variation of tetrahedral and octahedral band positions with Mg^{2+} ions of ferrite SNPs annealed at 900°C and 1100°C temperatures are shown in figure 5.4.

5.3.6 MAGNETIC MEASUREMENT

At room temperature, magnetic measurements of MgNi ferrite nanoparticles were recorded using VSM. The hysteresis loops plotted from the VSM data of these samples are shown in figure 3.11 for materials annealed at 900°C and in figure 4.3 for the material annealed at 1100°C respectively. The values of various magnetic parameters *viz:* saturation magnetization (M_S), remanence magnetization (M_R), coercivity (Hc) for the material are tabulated in table 5.9.

Table 5.9: Magnetic parameters of MgNi ferrite SNPs annealed at 900°C and 1100°C

Annealing Temp.	**900°C**			**1100°C**		
Mg^{2+} ion Compo.	M_S	M_R	H_C	M_S	M_R	Hc
(x)	(emu/g)	(emu/g)	(Oe)	(emu/g)	(emu/g)	(Oe)
0.1875	28.45	9.91	115	30.32	10.8	135
0.4375	27.41	9.45	110	29.1	10.11	127
0.8125	27.22	9.33	105	23.32	6.65	78

The magnetic parameters of the synthesized materials are same as typical for spinel ferrites [59]. The synthesized SNPs have low value of squareness ratio well below 0.5, low hysteresis loop area results in low eddy current losses. This indicates that the synthesized nanoparticles are superparamagnetic (SPM) in nature. The magnetic moment per unit formula unit μ_B, the value of the anisotropy constant K, M_S, H_C and M_R are calculated by equations 2.11, 2.12 and 2.13 and are listed in table 3.6.
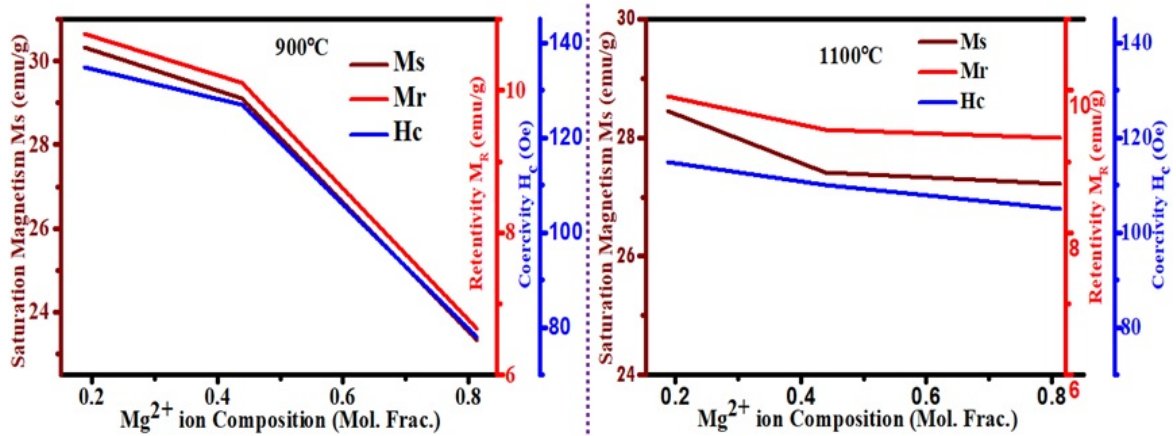
Figure 5.5: The values of saturation magnetization, coercivity and retentivity of MgNi ferrite SNPs annealed at 900°C and 1100°C

The anisotropy constant (K) value for the samples decreases with increase in Mg^{2+} composition. The decrease in K value is attributed to an increase in grain size with an increase in Mg^{2+} ions [167].

The magneto-crystalline anisotropy energy, which functions as an energy barrier to change in magnetizing direction, is connected to the anisotropic constant K. On the other hand, thermal agitation can be used to overcome this barrier. The association between magnetic characteristics and cationic distribution could explain the decline in magnetic parameters of $Mg_xNi_{1-x}Fe_2O_4$ [60, 60]. These findings are consistent with previous research on the same substance [20, 26]. The decrease in values of M_S, H_C and M_R of ferrite SNPs have already been discussed in chapter 3 section 3.5 and in chapter 4 section 4.5 respectively.

It is pertinent to mention here that the decrease in saturation magnetization, coercivity and retentivity is abrupt at higher composition of Mg^{2+} in materials annealed at 900°C may be attributed to presence of α-hematite phase. However, no such change is observed in the materials annealed at 1100°C because of absence of α-hematite phase.

5.3.7 ELASTIC PROPERTIES

The structural stability of crystal structures and the phase transitions that occurs are related to the physical quantity known as elasticity. Elasticity is the function of internal energy and binding forces between the molecules. Because of this, elastic coefficients are playing significant role in interpreting structural stability of crystalline materials. A contribution of C_{11} is required for the uniaxial strain, while for the biaxial strain, both the elastic components C_{11} and C_{12} are needed. However, for the zero diagonal strain tensor, only C_{44} is needed. For example, the elastic constants C_{11}, C_{12} denote elasticity in length and area respectively. When pressure is applied, the elastic constants grow monotonically, whereas C_{44} initially increases and then drops [27]. In general, cubic structures are regarded isotropic, meaning that elastic constants in three dimensions, namely C_{11}, C_{12} and C_{44} where ($C_{11} \sim C_{12}$) do not contribute to the cubic crystal structure. However, this approximation is only true if the synthesized particle has a low order or a very small crystallite size. In the present study of $Mg_xNi_{1-x}Fe_2O_4$, both have crystallite sizes ranging from 30 nm to 100 nm. Therefore the elastic constants C_{11}, C_{12} and C_{44} are determined using the equations 2.31, 2.32 & 2.33 and the values are tabulated in table 5.10 [10, 19, 42, 47, 50].

The elastic moduli of ferrite SNPs are calculated with their respective equations [10, 48, 52] *viz:* Young's modulus (Y) by equation (2.38), modulus of rigidity (G) by equation 2.39, Bulk modulus (B) by equation (2.40), poisson's ratio by equation 2.34 and Debye temperature by equation 2.47. The obtained values of these parameters are presented in table 5.8. The variation of Y, B and G with composition of Mg^{2+} ions in $Mg_xNi_{1-x}Fe_2O_4$ SNPs are shown in figure 5.7.

The value of Poisson's ratio is found to increase with higher Mg^{2+} composition and also increase with annealing temperature. This increase is attributed to the materials becoming more rigid at higher compositions of Mg^{2+} and higher annealing temperature as well. The Young's modulus and shear modulus found to increase with Mg^{2+} composition. However,
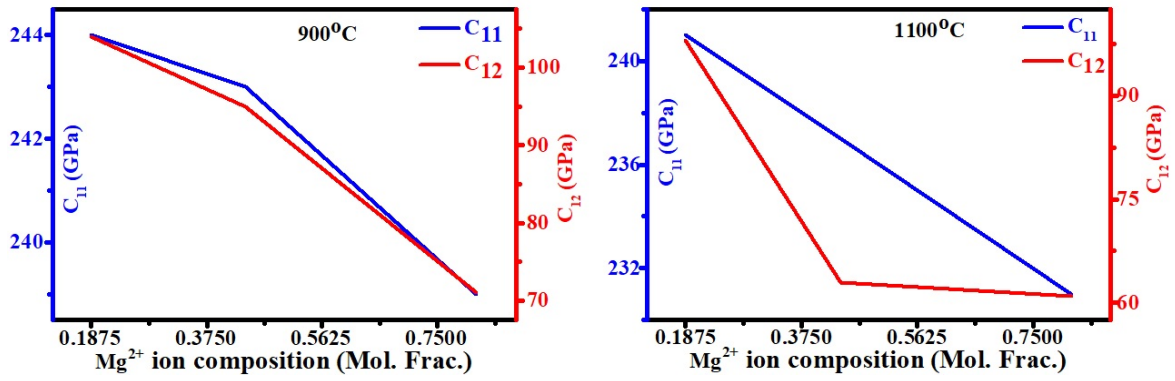
Figure 5.6: Variation of C_{11} and C_{12} with Mg^{2+} ion Composition in MgNi Ferrite at 900°C and 1100° C
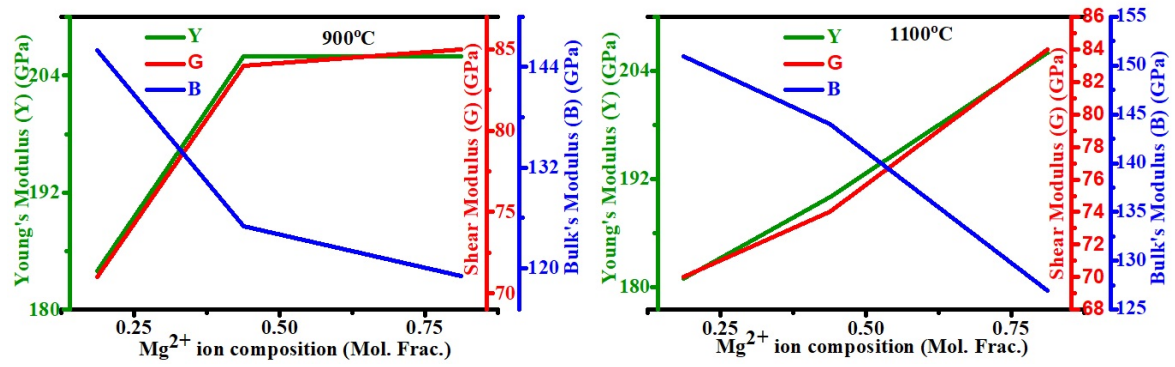
Figure 5.7: Values of Young's modulus (Y), shear modulus (G) & Bulk's modulus (B) v/s variation of MgNi ferrite SNPs annealed at 900°C and 1100 °C

Bulk's modulus decreases which may be attributed to the fact that volume of the material increases with Mg^{2+} composition abruptly. With an increase in annealing temperature, the bulk density also increases, indicating an increase in the crystallanity. The synthesized material is mechanically stable if the values of elastic constants obtained for the cubic crystal satisfies the following condition:

C_{11} - C_{12} > 0, C_{11} > 0, C_{44} > 0, C_{11} + 2C_{12} > 0

In the present study for ferrite SNPs, the above condition holds good for all synthesized samples. Hence the synthesized materials are elastically stable.

The longitudinal wave velocity (V_L) and transverse wave velocity (V_τ) in $Mg_xNi_{1-x}Fe_2O_4$ are estimated by equations 2.41, 2.42 & 2.43 respectively [9, 42]. The mean velocity (V_m) was estimated with the equation (2.46). The Anderson's relation [44] given in equation (2.43) used to find Debye temperature (θ_D). The value of V_A for $Mg_xNi_{1-x}Fe_2O_4$ SNPs annealed at 900°C, is 6.19×10^{-6} m^3 whereas it is 6.17×10^{-6} m^3 for sample annealed at 1100°C. The atomic volume of $Mg_xNi_{1-x}Fe_2O_4$ decreases for samples annealed at temperature of 1100 °C as compared to its value for sample annealed at 900 °C. Thus crystallanity of the synthesized material increased when they are annealed at higher temperature. In general,

77

as the annealing temperature increases, there occur a decay in the value of force constant (force constant is inversely proportional to bond length) attributed to increase in the τ-O and o-O bond lengths.

The W-H plots were linearly fitted using the equation 2.5, assuming that spinel cubic structure is always isotropic, *i.e.*, elastic strain produced in the crystallite is same in all direction of the crystallite known as the Uniform Deformation Model (UDM). In actual practice crystal structure is always anisotropic, meaning that elastic characteristics vary depending on the direction in which the crystal is oriented. This implies that even when applying a homogeneous deforming stress to a nanoparticle, different strains are produced in different directions due to a uniform deforming stress to produce variable strains in crystallographic directions [8]. This model is known as uniform stress deformation model (USDM). The equation 2.23 describes the anisotropic strain in this case. In this way, the Williamson-Hall equation has been reworked provided in equation 2.49, where in the cubic system Young's modulus of elasticity Y_{hkl} is modified to equation 2.50.

The elastic compliances namely S_{11}, S_{12} and S_{44} may be estimated from their elastic constants C_{11}, C_{12} & C_{44} using the relation 2.35, 2.36 & 2.37 and their values for both the SNPs are mentioned in table 5.10. The variation of elastic compliances S_{11} &, S_{12} are shown in figure 5.8.
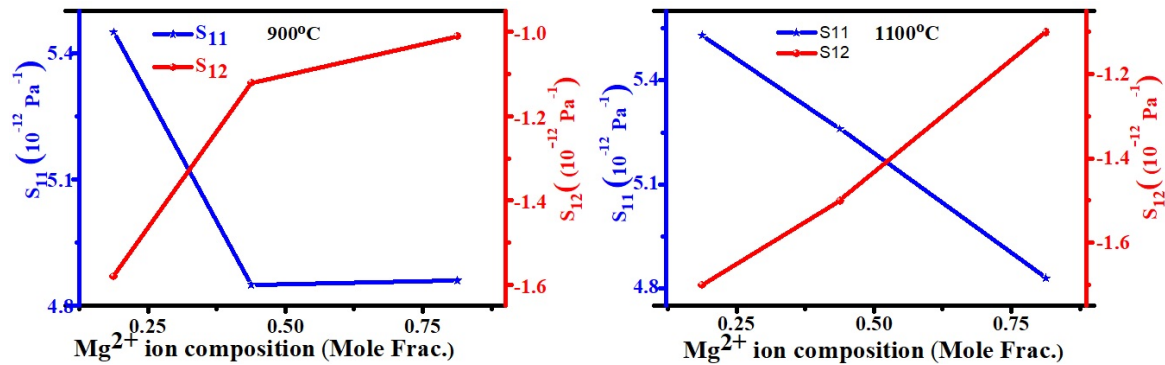
Figure 5.8: The values of S_{11} & S_{12} of MgNi ferrite SNPs annealed at 900°C and 1100°C

The saturation in values of S_{11} and S_{12} is attributed to the presence of α-hematite phase in the material having higher compositions of Mg^{2+} ions. The W-H plots plotted using USDM are shown in figure 5.9.

Anisotropic elastic modulus and lattice strain are considered in the uniform energy deformation model (UEDM). Although in this model, the density of deformation energy (u) is believed to be the cause of anisotropic lattice strain ϵ_{hkl}. The modified W-H equation in uniform energy deformation model (UEDM) is given by equation 2.51 and energy density is obtained by equation 2.52, with Hooke's law assuming homogeneity. On the basis of these equations, the W-H plots are shown in figure 5.10.

These values have been derived from the slope and intercept of the regression line in the
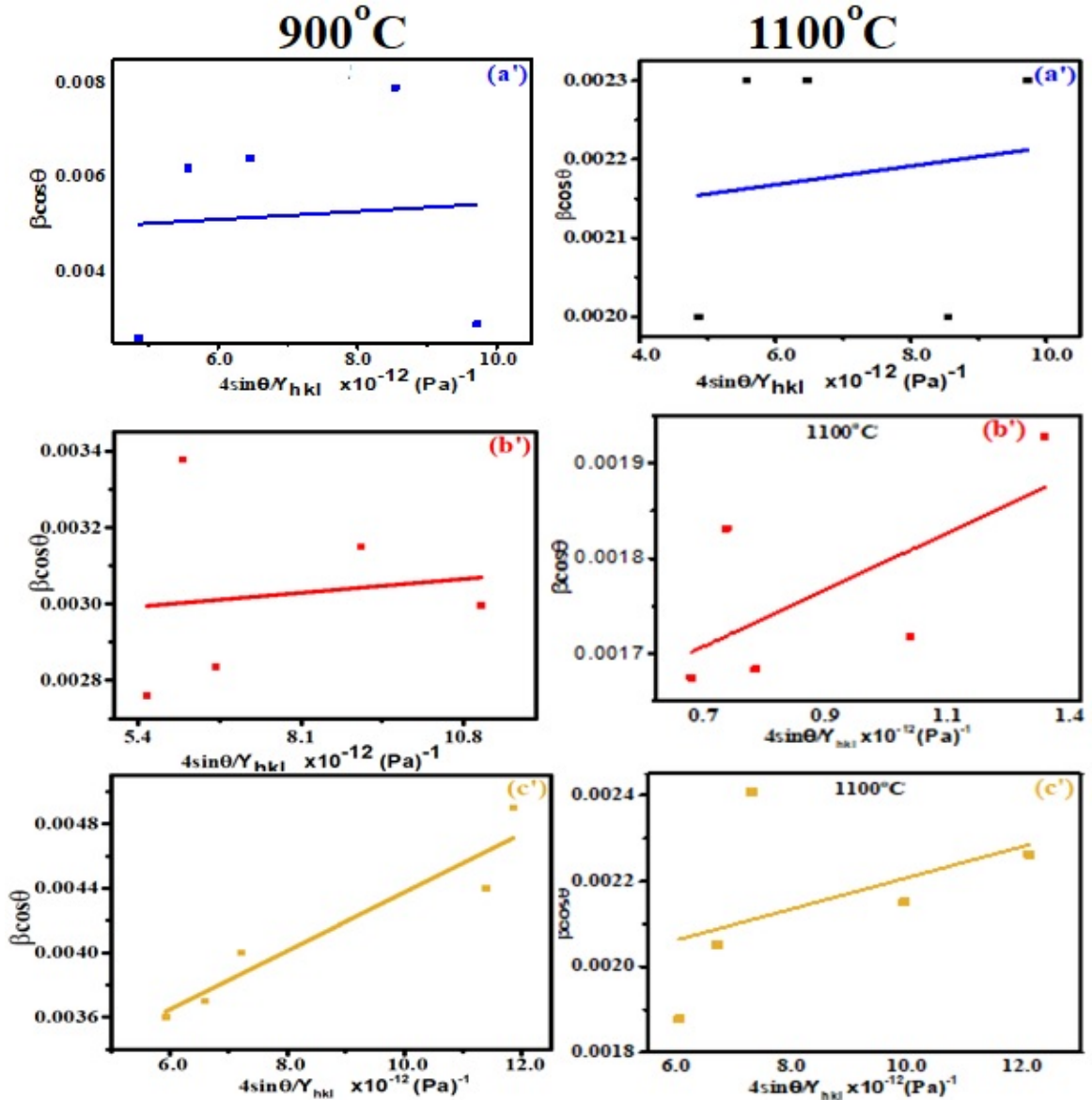
Figure 5.9: W-H plots for the MgNi ferrite SNPs annealed at 900° &1100°C in USDM

UEDM plots and their estimated values and corresponding strain values ϵ_{hkl} are listed in table 5.12 for SNPs $Mg_xNi_{1-x} Fe_2O_4$. For example, according to equation 2.53, the deformation stress and the deformation energy density are both inversely related. In the same material, the Young's modulus of elasticity of $Mg_xNi_{1-x}Fe_2O_4$ is lower at 900°C than at 1100°C. The lattice strain in $Mg_xNi_{1-x} Fe_2O_4$ annealed at 900°C is 6.08×10^{-4}ă and 5.34×10^{-5} for the same material annealed at 1100°C, respectively. W-H plots can be used to compare three of the aforementioned models used to investigate the XRD peak broadening of nanocrystalline $Mg_xNi_{1-x} Fe_2O_4$. The W-H plots from the considered three models yield non-zero slopes and intercepts. This observation advocates the co-existence of both size and strain broadening in the diffraction peaks of the synthesized ferrite nanoparticles. The combustion process involves a gas producing, self-propagating, exothermic redox reaction [8] between the metal

79
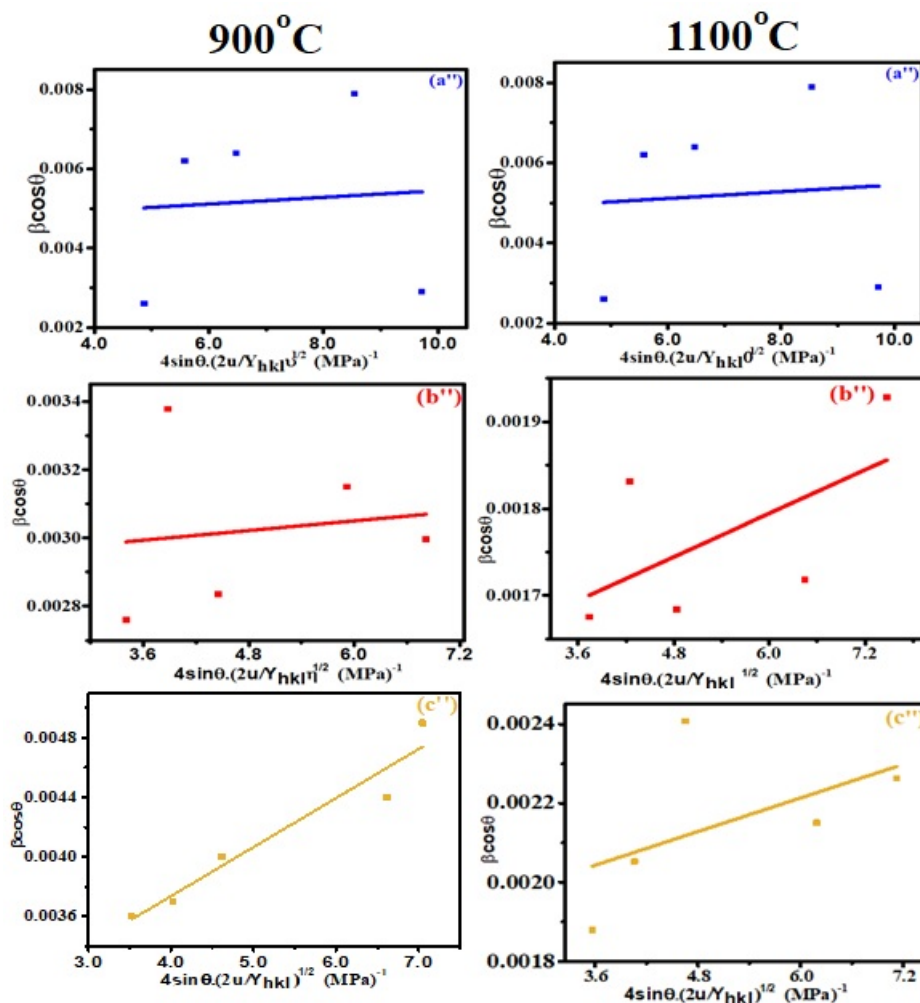
Figure 5.10: W-H plots for the MgNi ferrite SNPs annealed at 900° &1100°C in UEDM

Table 5.10: Values of elastic constants, elastic compliances, Pugh's ratio and porosity of MgNi ferrite SNPs annealed at 900°C and 1100°C

Annealing Temp.	**900°C**			**1100°C**		
Composition (x)	0.1875	0.4375	0.8125	0.1875	0.4375	0.8125
C_{11} (Gpa)	241	237	231	244	243	239
C_{12} (Gpa)	98	63	61	104	95	71
C_{44} (Gpa)	64	76	76	63	67	75
S_{11} $(\times 10^{-12})$Pa^{-1}	5.45	4.86	4.85	5.53	5.26	4.85
$S_{12}(\times 10^{-12})$Pa^{-1}	-1.58	-1.12	-1.01	-1.7	-1.5	-1.1
$S_{44}(\times 10^{-12})$Pa^{-1}	15.6	13.3	13	16	15	13.3
Porosity	0.1	0.29	0.35	0.06	0.13	0.29
Pughs Ratio	2.05	1.52	1.39	2.17	1.84	1.52

nitrate and fuel used. The lattice strain in Mg$_x$Ni$_{1-x}$Fe$_2$O$_4$ is caused due to the sudden thermal fluctuations. This may be due to the abrupt release of heat due to the decomposition of the precursor-mixture and the concurrent quenching of the product by the swift evolution

of gases during the auto-ignited combustion-reaction. Further this reaction runs for a very short duration and may be attributed to segregation of nanoparticles. The presence of tensile strain in the crystal lattice is indicated by a positive slope in the W-H plot, while the presence of compressive strain in the crystal lattice is indicated by a negative slope of the fitted line. However, the absence of any slope in the W-H plot indicates that the sample is strain free [54]. Because of the varying assumptions used for these three models, the equations for UDM, USDM, and UEDM are fundamentally different. As a result, W-H plots based on these three models for a given sample are expected to yield a wide range of crystallite size and lattice strain values. All of the W-H graphs in this study show positive slopes, indicating that all these SNPs have tenstile strain and expanded during their synthesis. It's also worth noting that the crystallite sizes computed from the intercepts of all the W-H plots are of comparable sizes. Positive slopes of W-H plots and various [24, 54] crystallite size values have been obtained from each of these three models and are shown in table 5.12.

Another important parameter which affects the diffraction peak broadening is dislocation density [55]. The dislocation density also influences the physical properties of poly crystalline material. It is used to find the internal strain and deforming stresses in the crystallites. Dislocations are estimated in the nano crystallite ferrite materials using Williamson-Hall relation 2.54.

The resultant dislocation density for $Mg_xNi_{1-x}Fe_2O_4$ for sample prepared at 900°C annealing temperature is 6.73×10^{13} m^{-2}. The particles in a nanoparticle system are held together by high adhesion [30], which causes welding between contacting surfaces.

The interaction between the particles causes them to stick together, increasing the necking-surface and decreasing the free surface area, resulting in significant strains and stresses in the necking-contact zones [56]. By considering the opening between particles, as well as the welded region, the Griffith model of stresses in strained fractures [52, 219] may be applied to nanoparticles. A stressed crack tip, according to Griffith's model, generates inhomogeneous strain and stress fields, can be inferred as the deformation field formed by super-dislocations with Burgers vector b. On the basis of some simple assumptions, the following correlation developed by Ungar et al. [47, 220] given by equation 2.55.

Table 5.11: Values of Youngs modulus, strain using USDM & UEDM models annealed at 900°C and 1100°C

Composition	<hkl>	900°C			1100°C		
		Y_{hkl}	ϵ (No. of Units x 10^{-5})		Y_{hkl}	ϵ (No. of Units x 10^{-5})	
		(GPa)	USDM	UEDM	(GPa)	USDM	UEDM
	111	211.45	39.9155	61.7343	206.55	5.6223	5.431
	220	215.64	39.1384	61.1304	210.78	5.5094	5.3762
	311	220.53	38.2715	60.4496	215.72	5.3833	5.3143
	222	211.45	39.9155	61.7343	206.55	5.6223	5.431
	400	229.3	36.8073	59.282	224.6	5.1704	5.2082
(a) x=0.1875	422	215.64	39.1384	61.1304	210.78	5.5094	5.3762
	511	225.31	37.4596	59.805	220.56	5.2653	5.2557
	440	215.64	39.1384	61.1304	210.78	5.5094	5.3762
	620	224.19	37.6465	59.954	219.42	5.2924	5.2693
	533	213.75	39.4851	61.4006	208.87	5.5598	5.4007
	111	180.08	7.4597	7.8555	149.14	41.5754	15.3022
	220	188.88	7.1121	7.6703	157.33	39.4123	14.8988
	311	199.78	6.7242	7.4582	167.59	36.9988	14.4354
	222	180.08	7.4597	7.8555	149.14	41.5754	15.3022
	400	221.34	6.0692	7.0857	188.34	32.9228	13.6171
(b) x=0.4375	422	188.88	7.1121	7.6703	157.33	39.4123	14.8988
	511	211.18	6.361	7.254	178.49	34.7388	13.9876
	440	188.88	7.1121	7.6703	157.33	39.4123	14.8988
	620	208.44	6.4447	7.3015	175.86	35.259	14.0919
	533	184.85	7.2672	7.7535	153.57	40.3775	15.0801
	111	168.68	107.8297	113.4127	165.19	22.125	24.6664
	220	176.51	103.048	110.8695	173.27	21.0939	24.0848
	311	186.14	97.713	107.9614	183.26	19.9436	23.4189
	222	168.68	107.8297	113.4127	165.19	22.125	24.6664
	400	205.05	88.7028	102.8634	203.04	18.0008	22.249
(c) x=0.8125	422	176.51	103.048	110.8695	173.27	21.0939	24.0848
	511	168.68	107.8297	113.4127	193.73	18.8663	22.7776
	440	176.51	103.048	110.8695	173.27	21.0939	24.0848
	620	193.77	93.867	105.8154	191.21	19.1143	22.9268
	533	172.92	105.1815	112.0114	169.57	21.554	24.346

Internal-stress and internal-strain degrees, represented by ρ_0 and ρbD, respectively, were calculated using equation 2.55. Table 5.12 shows the Griffith strain and stress values obtained for the nano crystallite $Mg_xNi_{1-x}Fe_2O_4$. The hydrostatic pressure created on the nanoparticle's surface by the intrinsic surface stress was calculated using the modified Laplace rule for solids, using equation 2.56 [8, 57, 221].

A tensile surface stress pulls the surface in and makes the curve of a particle surface more concave, whereas a compressive surface stress makes the curvature more convex. Based on these curvature measurements, surface stress was calculated experimentally.

A compressive surface stress (where $\Gamma_s < 0$) causes the particles to have tensile stress, which leads to lattice expansion. The current study's findings also support the theory of negative surface stress. The experimentally estimated surface stress for $Mg_xNi_{1-x}Fe_2O_4$ (x = 0.1875) nanoparticles annealed at 900°C is -14.21 Nm^{-1}. For the identical nanoparticle annealed at 1100°C the values -34.83 Nm^{-1}. Because the order of value is so near, the difference in surface stress estimated at a given temperature (900°C or 1100°C) noted in table 5.12. This surface stress is attributed solely to the assumptions made in the experimental estimates of force constants of site- A and site-B. The surface stress of $Mg_xNi_{1-x}Fe_2O_4$ nanoparticles is higher than that of the same particle annealed at (900°C), implying that tensile stress is higher for the particle annealed at higher temperature. While the particle size of $Mg_xNi_{1-x}Fe_2O_4$ annealed at 1100°C is 66.03 nm, the particle size of the same material annealed at 900°C is 35.19 nm.

Table 5.12: Micro structural parameters obtained for nanocrystalline MgNi ferrite SNPs annealed at 900°C & 1100°C

Method		Parameter (unit), x=	900° C			1100°C		
			(a) 0.1875	(b) 0.4375	(c) 0.8125	(a) 0.1875	(b) 0.4375	(c) 0.8125
W-H Analysis	UDM	D (nm)	35.19	47.81	60.55	66.03	94	93
		ϵ(no. unit)x10^{-4}	7.93	0.791	1.75	5.45	4.18	4.13
	USDM	D (nm)	30.08	47.48	54.16	66.03	90.61	75.36
		σ(Mpa)	84.4	13.43	181.89	11.61	62.01	36.55
	UDEM	D (nm)	32.54	47.65	57.3	66.03	90.01	72.44
		u (kJm^{-3})	40.29	0.56	108.46	0.3	1.75	5.03
Grifth Model		P_o(GPa)	0.28	2.62	6.71	0.19	0.15	0.15
		ρbD (no. unit)x10^{-3}	5.51	44.8	125.06	3.79	2.91	2.87
		Γ_s (Nm^{-1})	-14.21	-22.79	-12.05	-34.83	-27.86	-22.04
Laplace Approach		ϵ_s (no. unit)x10^{-2}	-1.83	-0.72	-3.67	-0.17	-0.32	-0.48
		γ (Jm^{-2})	1.92	3.06	1.13	8.62	5.68	4.68
		P (GPa)	-1.89	-1.92	-0.89	-2.11	-1.23	-1.17

The expression for surface energy is given by equation 2.59 using the relation 2.58 to 2.62. Surface strain, surface stress, and surface energy values for nanocrystalline $Mg_xNi_{1-x}Fe_2O_4$ have been determined using the afore mentioned relations and are presented in table 5.12. In the literature, there is no credible experimental measurement of surface stress of $Mg_xNi_{1-x}Fe_2O_4$. In the table 5.12, the values of crystallite size (D)calculated from UDM, USDM and UEDM models are presented. The crystallite size in all three models are in good agreement at both

annealing temperature and respective composition [42].

Table 5.12 shows the value of surface energy for $Mg_xNi_{1-x}Fe_2O_4$ SNPs. The surface energy is higher for samples annealed at higher temperatures [167, 222–224]. Also as the Mg^{2+} ion concentration increases, the surface energy increases as well.

5.4 CONCLUSION

All the three compositions of the $Mg_xNi_{1-x}Fe_2O_4$ were successfully synthesized using the sol-gel route annealed at 900°C & 1100°C have single phase. At 900°C annealing temperature secondary hematite phase is observed at higher compositions of Mg^{2+} ions. Both the SNPs are in manometer range. The size of SNPs annealed at 1100°C have large size (66-94 nm), whereas SNPs prepared at 900°C annealing temperature have particle in the size range (35-61 nm). Elastic parameters are found improved at higher annealing temperature. Rietveld refinement and spectroscopic studies indicates that the synthesized particles have inverse spinel structure. Magnetic parameters slightly improves their values however coercivity slightly decreases with higher annealing temperature. The synthesized materials are found to be superparamagnetic in nature. The elastic properties of synthesized particles shows that they are elastically stable. The stability increases with increase in annealing temperature. The morphological studies shows that the SNPs annealed at 900°C and 1100°C have cubical structure.

CHAPTER 6

SUMMARY & CONCLUSION

MgNi ferrites are soft magnetic material and very important from technological point of view. The unique properties of MgNi ferrite nanoparticles such as low coercivity, low magnetic losses, high resistivity (10^6 Ω-cm), moderate saturation magnetization, good mechanical hardness, chemical stability over wide range of temperature, high magnetic permeability and superparamagnetism in nature makes it promising candidates for electrical, electronic and bio-medical applications. In this work we have enhanced the magnetic properties of MgNi ferrite system in terms of substituting Mg^{2+} ions, synthesis methods and annealing temperature. Mg^{2+} ions have been used to replace the Ni^{2+} ions. As Mg^{2+} ion are non-magnetic the net magnetic moment of the lattice decreases with increase in Mg^{2+} ion composition consequently decreases the coercivity, saturation magnetization and retentivity of the synthesized material. In order to synthesize the MgNi ferrite particles in the nano range, sol-gel method has been used because this method has control over the size of synthesized particles. In order to visualize the effect of annealing temperature, the synthesized material is annealed at two temperatures *i.e.*, 900°C and 1100°C. The structural, morphological, magnetic and elastic properties of all the prepared samples have been analyzed using XRD, FESEM, EDX, FTIR, Raman, UV-Vis and VSM respectively. The variation in structural, morphological and magnetic properties have been explained in terms of variation of Mg^{2+} ion composition, distribution of cations in different sub-lattices, synthesis methods and annealing temperatures.

In first objective, all the samples have been processed by sol-gel method annealed at 900°C temperature. The variations in structural, morphological and magnetic properties have been explained in terms of Mg^{2+} ion composition. From XRD analysis it has been found that the prepared samples at x = 0.1875 and 0.4375 of Mg^{2+} ion composition has single phase spinel cubic structure. However, at x= 0.8125 the traces of less magnetic α-hematite phase also observed which is found to affect the structural and magnetic properties of ferrites adversely. The crystallite size (D) of all prepared samples has been calculated using Scherer formula and found to increase with Mg^{2+} ion composition because of its cation distribution in octahedral sites having larger size as compared to replaced Ni^{2+} ions. The confirmation of crystallite size and type of strain present in prepared nanoparticles has been carried out by Williamson-Hall (W-H) method using XRD data. The calculated crystallite size D from W-H method is in good agreement to that calculated from Scherer's formula in nm range and also a positive slop of linear fitted W-H plots shows tensile strain presented in all the prepared nanoparticles. The morphology of prepared samples gets changed with increasing Mg^{2+} ion composition with agglomeration of particles as investigated by FESEM.

85

FESEM micrographs also shows the porous nature of samples. EDX study revealed that in prepared samples, all elements are present in proper atomic percentage. The magnetic properties measurement from VSM shows that the saturation magnetization (M_S) decreased with increasing Mg^{2+} ion composition. The reduced value of (M_S) is due to replacement of magnetic Ni^{2+} ions from the octahedral siteB by non-magnetic Mg^{2+} ions. At higher composition of Mg^{2+} ion, the decrease in the value of (M_S) is due to spin canting effect caused by prominent secondary phase. The obtained values of retentivity (Mr) as well as coercivity(H_C) continuously decreases with Mg^{2+} analogous to the decrease in the value of (M_S) because of its positive magneto-crystalline anisotropy energy. The value of squareness ratio lies well below 0.5 indicate the superparamagnetic nature of the material. The theoretical and experimental results have good agreement with each other according to proposed cations distribution. The single phase spinel cubic structure and higher value of M_S indicates the usefulness of these material in EMI shielding.

In second objective, MgNi ferrite nanoparticles were again synthesized by sol-gel method and annealed at 1100°C. XRD study revealed that when samples annealed at high temperature, most of the hematite phase diminished and single phase spinel cubic structure nanoparticles has formed. The morphology of prepared samples gets changed with increasing Mg^{2+} ion composition with agglomeration of particles as investigated by FESEM. FESEM micrographs also shows the porous nature of samples. EDX study revealed that in prepared samples, all elements are present in atomic percentage. The magnetic properties measurement from VSM shows that the M_S decreases with increasing Mg^{2+} ion composition. The reduced value of M_S is due to replacement of magnetic Ni^{2+} ions from the octahedral site-B by non-magnetic Mg^{2+} ions. The obtained values of M_R as well as H_C continuously decreases with Mg^{2+} analogous to the decrease in the value of M_S because of its positive magneto-crystalline anisotropy energy. The value of squareness ratio lies below 0.5 indicates that the synthesized materials are superparamagnetic in nature. Further the low value of H_C and squareness ratio show that the synthesized materials are suitable for targeted drug delivery application. The theoretical and experimental results have good agreement with each other according to proposed cations distribution. The single phase spinel cubic structure and higher value of M_S indicates the usefulness of these material in EMI shielding. The theoretical lattice constant (a_{th}), Neel magnetic moment (N) and other parameters calculated from proposed cations distribution also have good agreement with results obtained from experimental data.

In third objective a comparative study of various parameters of these SNPs *viz:* structural, magnetic and elastic properties were estimated. Various analysis were carried out like morphological, structural and elastic parameters *viz:* elastic velocity, elastic constants and their compliances, Young's modulus, shear modulus, Bulk's modulus, Poissons ratio and Debye temperature. Various models were introduced such as Uniform Deformation Model

(UDM), Uniform Stress Deformation Model (USDM) and Uniform Energy Deformation Model(UEDM) to estimate and address the various parameters. Moreover, on the basis of detailed comparative interpretation for the prepared magnetic nano ferrites, magnetic properties such as magnetic saturation, remnant field, coercivity, magnetic moment, squareness ratio, anisotropy constant and other allied parameters were studied. The XRD data of all the three compositions of $Mg_xNi_{1-x}Fe_2O_4$ (SNPs) have been refined for Rietveld refinement using Fullprof suit software. For all of the samples, the goodness of fit (GOF) value was found to very close to 1, indicating good fitting of data points. The presence of any form of contaminant in the produced nanostructures was ruled out by Rietveld refinement analysis. The value of χ^2 in the Rietveld data is observed close to 1 further indicates the excellent fit with the experimental data.

On comparing it is observed that the synthesized materials annealed at 900 °C and 1100°C have single cubical phase. However, in material synthesized at 900°C, traces of secondary hematite phase are observed at higher Mg^{2+} ion composition. The lattice parameter obtained from Sherer's formula and from W-H analysis shows that crystallite sizes are in nano meter range and found to increase at higher annealing temperature. The particle size obtained from HRTEM and FESEM are also in good agreement with the crystallite size calculated from XRD data. The materials shows exhibiting superparamagnetic nature and magnetic properties got improved at higher annealing temperature. The comparative analysis of the materials annealed at two temperature show that these synthesized materials are elastically stable and stability increases with increase in annealing temperature. The variation in M_S, M_R and H_C with Mg^{2+} ion composition are due to cations distribution effect. Low value of coercivity H_C indicates that prepared samples are magnetically soft in nature. Thus nanoparticles are successfully prepared by aqueous sol-gel method have their usefulness in targeted drug delivery, hyperthermia, MRI, EMI shielding and magnetic recording device, etc. From these results it can be concluded that

1. MgNi Ferrites are successfully synthesized in nano range at annealing temperature of 900°C and 1100°C.

2. Both the synthesized MgNi ferrite nanoparticles exhibits superparamagnetism.

3. Synthesized SNPs are elastically stable at both annealing temperature and elasticity rises with rise in annealing temperature.

On the basis of above findings it is concluded that

MgNi Ferrite nanoparticles are more stable at 1100°C annealing temperature and suitable for targeted drug delivery and electrocatalysis of water.

Future scope

Based on the findings of the work done in the thesis further research is possible. Following are the possible future plans related to the current research:

- More characterizations of the synthesized particles can be performed *viz:* dielectric studies, mossabaur, etc., to study the electrical properties along with more structural inputs.

- Furthermore, the synthesized nano particles can be doped with suitable elements to improvise the existing properties of nanoparticles.

Bibliography

[1] R. Valenzuela, "Novel applications of ferrites," *Physics Research International*, 2012. [Online]. Available: https://doi.org/10.1155/2012/591839

[2] J. Haspers, "Ferrites-their properties and applications," in *Modern Materials*. Elsevier, 1962, vol. 3, pp. 259–341. [Online]. Available: https://doi.org/10.1016/B978-1-4831-9657-2.50009-7

[3] M. Pardavi-Horvath, "Microwave applications of soft ferrites," *Journal of Magnetism and Magnetic Materials*, vol. 215, pp. 171–183, 2000. [Online]. Available: https://doi.org/10.1016/S0304-8853(00)00106-2

[4] J. Wei, K. Niikura, T. Higuchi, T. Kimura, H. Mitomo, H. Jinnai, Y. Joti, Y. Bessho, Y. Nishino, Y. Matsuo *et al.*, "Yolk/shell assembly of gold nanoparticles by size segregation in solution," *Journal of the American Chemical Society*, vol. 138, no. 10, pp. 3274–3277, 2016.

[5] H. Schafer, K. Kupper, and J. Wollschlager, "Oxidized mild steel an efficient anode for electrocatalytically initiated water splitting," *ChemSusChem*, vol. 8, pp. 3099–3110, 2015.

[6] G. F. Dionne, D. E. Oates, D. H. Temme, and J. A. Weiss, "Ferrite-superconductor devices for advanced microwave applications," *IEEE Transactions on Microwave theory and Techniques*, vol. 44, pp. 1361–1368, 1996.

[7] A. Verma, M. Alam, R. Chatterjee, T. Goel, and R. Mendiratta, "Development of a new soft ferrite core for power applications," *Journal of Magnetism and Magnetic Materials*, vol. 300, pp. 500–505, 2006. [Online]. Available: https://doi.org/10.1016/j.jmmm.2005.05.040

[8] G. Stojanovic, M. Damnjanovic, V. Desnica, L. Zivanov, R. Raghavendra, P. Bellew, and N. Mcloughlin, "High-performance zig-zag and meander inductors embedded in ferrite material," *Journal of Magnetism and Magnetic Materials*, vol. 297, pp. 76–83, 2006. [Online]. Available: https://doi.org/10.1016/j.jmmm.2005.02.058

[9] G. I. Likhtenshtein, J. Yamauchi, S. i. Nakatsuji, A. Smirnov, and R. Tamura, *Nitroxides*. Springer, 2020. [Online]. Available: https://doi.org/10.1007/978-3-030-34822-9

[10] T. Thomson, L. Abelmann, and H. Groenland, "Magnetic data storage-past present and future." Springer, 2008, pp. 237–306.

[11] M. E. F. Brollo, R. López-Ruiz, D. Muraca, S. J. Figueroa, K. R. Pirota, and M. Knobel, "Compact ag@ fe3o4 core-shell nanoparticles by means of single-step thermal decomposition reaction," *Scientific reports*, vol. 4, no. 1, pp. 1–6, 2014.

[12] R. Popovtzer, A. Agrawal, N. A. Kotov, A. Popovtzer, J. Balter, T. E. Carey, and R. Kopelman, "Targeted gold nanoparticles enable molecular ct imaging of cancer," *Nano letters*, vol. 8, no. 12, pp. 4593–4596, 2008.

[13] I. Carmeli, I. Lieberman, L. Kraversky, Z. Fan, A. O. Govorov, G. Markovich, and S. Richter, "Broad band enhancement of light absorption in photosystem i by metal nanoparticle antennas," *Nano letters*, vol. 10, no. 6, pp. 2069–2074, 2010.

[14] R. Valenzuela, *Magnetic ceramics*. Cambridge university press, 2005. [Online]. Available: https://doi.org/10.1039/9781788010375

[15] S. H. Bossmann and H. Wang, *Magnetic nanomaterials- applications in catalysis and life sciences*. Royal Society of Chemistry, 2017. [Online]. Available: https://doi.org/10.1039/9781788010375

[16] A.-H. Lu, E. e. Salabas, and F. Schuth, "Magnetic nanoparticles synthesis, protection, functionalization, and application," *Angewandte Chemie International Edition*, vol. 46, pp. 1222–1244, 2007. [Online]. Available: https://doi.org/10.1002/anie.200602866

[17] M. Tadic, S. Kralj, M. Jagodic, D. Hanzel, and D. Makovec, "Magnetic properties of novel superparamagnetic iron oxide nanoclusters," *Applied Surface Science*, vol. 322, pp. 255–264, 2014. [Online]. Available: https://doi.org/10.1016/j.apsusc.2014.09.181

[18] K. Buschow, "New developments in hard magnetic materials," *Reports on Progress in Physics*, vol. 54, p. 1123, 1991. [Online]. Available: https://doi.org/10.1088/0034-4885/54/9/001

[19] P. M. Mendes, Y. Chen, and o. Palmer, "Nanostructures from nanoparticles," *Journal of Physics- Condensed Matter*, vol. 15, p. S3047, 2003. [Online]. Available: https://doi.org/10.1088/0953-8984/15/42/005

[20] Y. Yafet and C. Kittel, "Antiferromagnetic arrangements in ferrites," *Physical Review*, vol. 87, 1952. [Online]. Available: https://doi.org/10.1103/PhysRev.87.290

[21] P. Kumar, N. Rajesh Kumar, S. Chander Katyal, S. Kumar Khah *et al.*, "Magnetic thin film formation on the surface of solution induced via island growth of nanoparticles," *Advanced Materials Letters*, vol. 4, no. 1, pp. 74–77, 2013.

[22] D. Bruns, I. Kiesel, S. Jentsch, S. Lindemann, C. Otte, T. Schemme, T. Kuschel, and J. Wollschläger, "Structural analysis of feo (1 1 1)/ag (0 0 1): undulation of hexagonal oxide monolayers due to square lattice metal substrates," *Journal of Physics: Condensed Matter*, vol. 26, no. 31, p. 315001, 2014.

[23] Z. Ullah, S. Atiq, and S. Naseem, "Influence of pb doping on structural, electrical and magnetic properties of sr-hexaferrites," *Journal of Alloys and Compounds*, vol. 555, pp. 263–267, 2013. [Online]. Available: https://doi.org/10.1016/j.jallcom.2012.12.061

[24] D. Rawat, P. B. Barman, and R. R. Singh, "Multifunctional magneto-fluorescent niznfe@ cds core-shell nanostructures for multimodal applications," *Materials Chemistry and Physics*, vol. 231, pp. 388–396, 2019. [Online]. Available: https://doi.org/10.1016/j.matchemphys.2019.04.028

[25] H. A. Lowenstam, "Magnetite in denticle capping in recent chitons (polyplacophora)," *Geological Society of America Bulletin*, vol. 73, pp. 435–438, 1962. [Online]. Available: https://doi.org/10.1130/0016-7606(1962)73

[26] I. SafarikMirka and Safarikova, "Magnetic nanoparticles and biosciences," *nanostructured materials*, pp. 1–23, 2002.

[27] A. Moitra, S. Kim, S.-G. Kim, S. Erwin, Y.-K. Hong, and J. Park, "Defect formation energy and magnetic properties of aluminum-substituted m-type barium hexaferrite," *Computational Condensed Matter*, vol. 1, pp. 45–50, 2014. [Online]. Available: https://doi.org/10.1016/j.cocom.2014.11.001

[28] S. P. Gubin, Y. A. Koksharov, G. Khomutov, and G. Y. Yurkov, "Magnetic nanoparticles-preparation, structure and properties," *Russian Chemical Reviews*, vol. 74, p. 489, 2005. [Online]. Available: https://doi.org/10.1070/RC2005v074n06ABEH000897

[29] Z. Li, L. Guoqing, L. Chen, W. Yuping, and C. Ong, "Co 2+ ti 4+ substituted z-type barium ferrite with enhanced imaginary permeability and resonance frequency," *Journal of applied Physics*, vol. 99, p. 063905, 2006. [Online]. Available: https://doi.org/10.1063/1.2180431

[30] B.-W. Li, Y. Shen, Z.-X. Yue, and C.-W. Nan, "Enhanced microwave absorption in nickel/hexagonal-ferrite/polymer composites," *Applied Physics Letters*, vol. 89, p. 132504, 2006. [Online]. Available: https://doi.org/10.1063/1.2357565

[31] C. Xiang, Y. Pan, X. Liu, X. Sun, X. Shi, and J. Guo, "Microwave attenuation of multiwalled carbon nanotube-fused silica composites," *Applied physics letters*, vol. 87, p. 123103, 2005. [Online]. Available: https://doi.org/10.1063/1.2051806

[32] Y.-B. Feng, T. Qiu, C.-Y. Shen, and X.-Y. Li, "Electromagnetic and absorption properties of carbonyl iron/rubber radar absorbing materials," *IEEE Transactions on Magnetics*, vol. 42, pp. 363–368, 2006. [Online]. Available: https://doi.org/10.1109/TMAG.2005.862763

[33] R. Che, C. Zhi, C. Liang, and X. Zhou, "Fabrication and microwave absorption of carbon nanotubes/ cofe 2 o 4 spinel nanocomposite," *Applied Physics Letters*, vol. 88, p. 033105, 2006. [Online]. Available: https://doi.org/10.1063/1.2165276

[34] A. Goldman, *Modern ferrite technology*. Springer Science and Business Media, 2006.

[35] S. Patange, S. E. Shirsath, S. Jadhav, K. Lohar, D. Mane, and K. Jadhav, "Rietveld refinement and switching properties of cr3+ substituted nife2o4 ferrites," *Materials Letters*, vol. 64, no. 6, pp. 722–724, 2010.

[36] N. K. Jaiswal and P. Srivastava, "Fe-doped armchair graphene nanoribbons for spintronic/interconnect applications," *IEEE transactions on nanotechnology*, vol. 12, no. 5, pp. 685–691, 2013.

[37] Ü. Özgür, Y. Alivov, and H. Morkoç, "Microwave ferrites, part 1: fundamental properties," *Journal of materials science: Materials in electronics*, vol. 20, no. 9, pp. 789–834, 2009.

[38] C. T. Brock and S. Teeter, "Precious gems of the appalachian mountains," *General Article*, 2010.

[39] R. Jotania, "Crystal structure, magnetic properties and advances in hexaferrites: A brief review," in *AIP Conference Proceedings*, vol. 1621. American Institute of Physics, 2014, pp. 596–599. [Online]. Available: https://doi.org/10.1063/1.4898528

[40] K. Nadeem, S. Rahman, and M. Mumtaz, "Effect of annealing on properties of mg doped zn-ferrite nanoparticles," *Progress in Natural Science: Materials International*, vol. 25, pp. 111–116, 2015. [Online]. Available: https://doi.org/10.1016/j.pnsc.2015.02.001

[41] Z. Zhang, "Study on the influence of magnesium doping on the magnetic properties of spinel zn-mg ferrite," *Materials Today Communications*, vol. 26, p. 101734, 2021. [Online]. Available: https://doi.org/10.1016/j.mtcomm.2020.101734

[42] H. Moradmard, S. F. Shayesteh, P. Tohidi, Z. Abbas, and M. Khaleghi, "Structural, magnetic and dielectric properties of magnesium doped nickel ferrite nanoparticles," *Journal of Alloys and Compounds*, vol. 650, pp. 116–122, 2015. [Online]. Available: https://doi.org/10.1016/j.jallcom.2015.07.269

[43] E. E. Ateia, A. A. El-Bassuony, G. Abdellatif, and A. T. Mohamed, "The impact of ni substitution on the structural and magnetic properties of mg nano-ferrite," *Silicon*, vol. 10, pp. 1687–1696, 2018. [Online]. Available: https://doi.org/10.1007/s12633-017-9653-7

[44] M. Eltabey, A. Massoud, and C. Radu, "Microstructure and superparamagnetic properties of mg-ni-cd ferrites nanoparticles," *Journal of Nanomaterials*, vol. 2014, 2014. [Online]. Available: https://doi.org/10.1155/2014/492832

[45] S. Thakur, S. C. Katyal, A. Gupta, V. Reddy, S. Sharma, M. Knobel, and M. Singh, "Nickel- zinc ferrite from reverse micelle process: Structural and magnetic properties," *The Journal of Physical Chemistry C*, vol. 113, pp. 20 785–20 794, 2009. [Online]. Available: https://doi.org/10.1021/jp9050287

[46] P. Kumar, S. Sharma, M. Knobel, and M. Singh, "Effect of la3+ doping on the electric, dielectric and magnetic properties of cobalt ferrite," *Journal of Alloys and Compounds*, vol. 508, pp. 115–118, 2010. [Online]. Available: https://doi.org/10.1016/j.jallcom.2010.08.007

[47] V. Mittal, S. Bera, R. Nithya, M. Srinivasan, S. Velmurugan, and S. Narasimhan, "Solid state synthesis of mg-ni ferrite and characterization by xrd and xps," *Journal of nuclear materials*, vol. 335, pp. 302–310, 2004. [Online]. Available: https://doi.org/10.1016/j.jnucmat.2004.05.010

[48] M. Shobana, K. Kim, and J.-H. Kim, "Impact of magnesium substitution in nickel ferrite: Optical and electrochemical studies," *Physica E Low-dimensional Systems and Nanostructures*, vol. 108, pp. 100–104, 2019. [Online]. Available: https://doi.org/10.1016/j.physe.2018.12.013

[49] P. Chavan and L. Naik, "X-ray diffraction studies and dielectric properties of ni doped mg ferrites," *Vacuum*, vol. 152, pp. 47–49, 2018. [Online]. Available: https://doi.org/10.1016/j.vacuum.2018.03.007

[50] C. Anumol, M. Chithra, S. Rout, and S. C. Sahoo, "Effect of magnesium substitution on structural and magnetic properties of nickel ferrite nanoparticles," *Journal of Superconductivity and Novel Magnetism*, vol. 33, pp. 1611–1617, 2020. [Online]. Available: https://doi.org/10.1007/s10948-019-05192-8

[51] P. Thakur, D. Chahar, S. Taneja, N. Bhalla, and A. Thakur, "A review on mnzn ferrites: Synthesis, characterization and applications," *Ceramics international*, 2020. [Online]. Available: https://doi.org/10.1016/j.ceramint.2020.03.287

[52] S. Thankachan, S. Xavier, B. Jacob, and E. Mohammed, "A comparative study of structural, electrical and magnetic properties of magnesium ferrites," *Journal of experimental Nanoscience*, vol. 8, pp. 347–357, 2013. [Online]. Available: https://doi.org/10.1007/s10854-018-9398-0

[53] W. Ye, Y. Yang, X. Fang, and o. Arif, "2d cocrystallized metal-organic nanosheet array," *ACS Sustainable Chemistry and Engineering*, vol. 7, pp. 18 085–18 092, 2019. [Online]. Available: https://doi.org/10.1021/acssuschemeng.9b05126

[54] D. Rawat, P. Barman, and R. R. Singh, "Corroboration and efficacy of magneto-fluorescent (niznfe/cds) nanostructures prepared using differently processed core," *Scientific reports*, vol. 9, pp. 1–12, 2019. [Online]. Available: https://doi.org/10.1038/s41598-019-51631-w

[55] N. Sulaiman, M. Ghazali, B. Majlis, J. Yunas, and M. Razali, "Superparamagnetic calcium ferrite nanoparticles synthesized using a simple sol-gel method for targeted drug delivery," *Bio-medical materials and engineering*, vol. 26, pp. S103–S110, 2015. [Online]. Available: https://doi.org/10.3233/BME-151295

[56] K. Jayasankar, A. Pandey, B. Mishra, and S. Das, "Evaluation of microstructural parameters of nanocrystalline y2o3 by x-ray diffraction peak broadening analysis," *Materials Chemistry and Physics*, vol. 171, pp. 195–200, 2016. [Online]. Available: https://doi.org/10.1016/j.matchemphys.2016.01.005

[57] A. Chatterjee, D. Das, S. Pradhan, and D. Chakravorty, "Synthesis of nanocrystalline nickel-zinc ferrite by the sol-gel method," *Journal of magnetism and magnetic materials*, vol. 127, pp. 214–218, 1993. [Online]. Available: https://doi.org/10.1016/0304-8853(93)90217-P

[58] E. De Grave, A. Govaert, D. Chambaere, and G. Robbrecht, "A mossbauer effect study of mgfe2o4," *Physica B+ C*, vol. 96, pp. 103–110, 1979. [Online]. Available: https://doi.org/10.1016/0378-4363(79)90104-9

[59] J. Jakubovics, "Magnetic domain structure of thin uniaxial crystals," *Philosophical Magazine*, vol. 14, pp. 881–899, 1966. [Online]. Available: https://doi.org/10.1080/14786436608244760

[60] M. Kus, T. Y. Alic, C. Kirbiyik, C. Baslak, K. Kara, and D. A. Kara, "Synthesis of nanoparticles," in *Handbook of Nanomaterials for Industrial Applications*. Elsevier, 2018, pp. 392–429. [Online]. Available: https://doi.org/10.1016/B978-0-12-813351-4.00025-0

[61] S. Hashmi, *Comprehensive materials processing*. Newnes, 2014.

[62] A. A. Gaikwad and S. Kulkarni, "Enhanced magnetic and permeability properties of mn-substituted nicuzn nanoparticles for ferrite core application," *Journal of Superconductivity and Novel Magnetism*, pp. 1–10, 2021. [Online]. Available: https://doi.org/10.1007/s10948-021-05941-8

[63] C. B. Carter and M. G. Norton, "Ceramics in biology and medicine," *Ceramic Materials: Science and Engineering*, pp. 635–651, 2007. [Online]. Available: https://doi.org/10.1007/978-1-4614-3523-5

[64] E. Bruck, *Handbook of Magnetic Materials*. Elsevier, 2017.

[65] O. Kahn, "Molecular magnetism," *VCH Publishers, Inc.(USA), 1993*, p. 393, 1993.

[66] A. Goldman, "Handbook of modern ferromagnetic materials," *Pub Boston USA*, 1999.

[67] S. Saini, R. Frankel, D. Stark, and J. Ferrucci Jr, "Magnetism: a primer and review," *American Journal of Roentgenology*, vol. 150, pp. 735–743, 1988. [Online]. Available: https://www.ajronline.org/doi/pdf/10.2214/ajr.150.4.735

[68] M. Forrester and F. Kusmartsev, "The nano-mechanics and magnetic properties of high moment synthetic antiferromagnetic particles," *physica status solidi (a)*, vol. 211, pp. 884–889, 2014. [Online]. Available: https://doi.org/10.1002/pssa.201330122

[69] R. E. Hummel, "Electrical properties of polymers, ceramics, dielectrics, and amorphous materials," in *Electronic properties of materials*. Springer, 2011, pp. 181–211.

[70] N. A. Spaldin and N. D. Mathur, "Magnetic materials: fundamentals and device applications," *Physics Today*, vol. 56, pp. 62–63, 2003. [Online]. Available: https://doi.org/10.1063/1.1650232

[71] B. Cullity, "Introduction to magnetic materials, addison-wesley publishing co." *Inc. Reading MA*, 1972. [Online]. Available: ISBN:978-0-471-47741-9

[72] N. A. Spaldin, *Magnetic materials: fundamentals and applications*. Cambridge university press, 2010.

[73] G. Daalderop, P. Kelly, and M. Schuurmans, "First-principles calculation of the magnetocrystalline anisotropy energy of iron, cobalt, and nickel," *Physical Review B*, vol. 41, p. 11919, 1990. [Online]. Available: https://doi.org/10.1103/PhysRevB.41.11919

[74] R. D. James and M. Wuttig, "Magnetostriction of martensite," *Philosophical magazine A*, vol. 77, pp. 1273–1299, 1998. [Online]. Available: https://doi.org/10.1080/01418619808214252

[75] L. Neel, "Proprietes magnetiques des ferrites- ferrimagnetisme et antiferromagnetisme," in *Annales de physique*, vol. 12, 1948, pp. 137–198. [Online]. Available: https://doi.org/10.1051/anphys/194812030137

[76] V. Nandwana, R. Zhou, J. Mohapatra, S. Kim, P. V. Prasad, J. Liu, and V. P. Dravid, "Exchange coupling in soft magnetic nanostructures and its direct effect on their theranostic properties," *ACS applied materials and interfaces*, vol. 10, pp. 27 233–27 243, 2018. [Online]. Available: https://doi.org/10.1021/acsami.8b09346

[77] R. Chantrell and K. O'Grady, "Magnetic characterization of recording media," *Journal of Physics D: Applied Physics*, vol. 25, p. 1, 1992. [Online]. Available: https://doi.org/10.1016/0304-8853(91)90231-X

[78] A. Sebt and M. Akhavan, "Switching field distribution of magnetic fine particles," *Journal of magnetism and magnetic materials*, vol. 237, pp. 111–118, 2001. [Online]. Available: https://doi.org/10.1016/S0304-8853(01)00440-1

[79] J. Lodder, "Magnetic recording hard disk thin film media," *Handbook of magnetic materials*, vol. 11, pp. 291–405, 1998. [Online]. Available: https://doi.org/10.1016/S1567-2719(98)11006-5

[80] S. F. Shaikh, M. Ubaidullah, R. S. Mane, and A. M. Al-Enizi, "Types, synthesis methods and applications of ferrites," *Spinel Ferrite Nanostructures for Energy Storage Devices*, p. 51, 2020. [Online]. Available: https://doi.org/10.1016/B978-0-12-819237-5.00004-3

[81] C. Prakash and J. Baijal, "Dielectric behaviour of tetravalent titanium-substituted ni-zn ferrites," *Journal of the Less Common Metals*, vol. 107, pp. 51–57, 1985. [Online]. Available: https://doi.org/10.1016/0022-5088(85)90240-1

[82] M. Khairy and M. Gouda, "Electrical and optical properties of nickel ferrite/polyaniline nanocomposite," *Journal of advanced research*, vol. 6, pp. 555–562, 2015. [Online]. Available: https://doi.org/10.1016/j.jare.2014.01.009

[83] M. Niederberger and o. Pinna, "A general soft-chemistry route to perovskites and related materials- synthesis of batio3, bazro3, and linbo3 nanoparticles," *Angewandte Chemie*, vol. 116, pp. 2320–2323, 2004. [Online]. Available: https://doi.org/10.1002/anie.200353300

[84] J.-K. Kim and M. Varenberg, "Contact splitting in dry adhesion and friction-reducing the influence of roughness," *Beilstein journal of nanotechnology*, vol. 10, pp. 1–8, 2019. [Online]. Available: https://doi.org/10.3762/bjnano.10.1

[85] K. K. Kefeni, T. A. Msagati, and B. B. Mamba, "Ferrite nanoparticles-synthesis, characterisation and applications in electronic device," *Materials Science and Engineering B*, vol. 215, pp. 37–55, 2017. [Online]. Available: https://doi.org/10.1016/j.mseb.2016.11.002

[86] A. Jilani, M. S. Abdel-Wahab, and A. H. Hammad, "Advance deposition techniques for thin film and coating," *Modern Technologies for Creating the Thin-film Systems and Coatings*, vol. 2, pp. 137–149, 2017. [Online]. Available: https://doi.org/10.5772/65702

[87] R. Srivastava and B. Yadav, "Ferrite materials: introduction, synthesis techniques, and applications as sensors," *International Journal of Green Nanotechnology*, vol. 4, pp. 141–154, 2012. [Online]. Available: https://doi.org/10.1080/19430892.2012. 676918

[88] A. Venkataraman, V. A. Hiremath, S. Date, and S. Kulkarni, "A new combustion route to gamma-fe 2 o 3 synthesis," *Bulletin of Materials Science*, vol. 24, pp. 617–621, 2001.

[89] G. Ennas, G. Marongiu, A. Musinu, A. Falqui, P. Ballirano, and R. Caminiti, "Characterization of nanocrystalline γ–fe 2 o 3 prepared by wet chemical method," *Journal of materials research*, vol. 14, pp. 1570–1575, 1999. [Online]. Available: https://doi.org/10.1557/JMR.1999.0210

[90] N. Mizutani, T. Iwasaki *et al.*, "Effect of ferrous ferric ions molar ratio on reaction mechanism," *Bulletin of Materials Science*, vol. 31, pp. 713–717, 2008. [Online]. Available: https://doi.org/10.1007/s12034-008-0112-3

[91] B. Narasimhan, S. Prabhakar, P. Manohar, and F. Gnanam, "Synthesis of gamma ferric oxide by direct thermal decomposition of ferrous carbonate," *Materials Letters*, vol. 52, pp. 295–300, 2002. [Online]. Available: https://doi.org/10.1016/S0167-577X(01)00409-8

[92] M. Zayat and D. Levy, "Blue coal2o4 particles prepared by the sol- gel and citrate-gel methods," *Chemistry of Materials*, vol. 12, pp. 2763–2769, 2000. [Online]. Available: https://doi.org/10.1021/cm001061z

[93] L. L. Hench and J. K. West, "The sol-gel process," *Chemical reviews*, vol. 90, pp. 33–72, 1990. [Online]. Available: https://doi.org/10.1021/cr00099a003

[94] W. B. Cross and L. o. Affleck, "Self-propagating high-temperature synthesis of ferrites mfe 2 o 4," *Journal of Materials Chemistry*, vol. 9, pp. 2545–2552, 1999. [Online]. Available: https://doi.org/10.1039/A904431K

[95] I. Gul, W. Ahmed, and A. Maqsood, "Electrical and magnetic characterization of nanocrystalline ni zn ferrite synthesis by co-precipitation route," *Journal of Magnetism and Magnetic Materials*, vol. 320, pp. 270–275, 2008. [Online]. Available: https://doi.org/10.1016/j.jmmm.2007.05.032

[96] F. Chen, M. Chen, and o. Yang, "Terbium-doped gadolinium oxide nanoparticles," *Physical Chemistry Chemical Physics*, vol. 17, pp. 1189–1196, 2015. [Online]. Available: https://doi.org/10.1039/C4CP04380D

[97] A. Kalam, A. G. Al-Sehemi *et al.*, "Modified solvothermal synthesis of cobalt ferrite (cofe2o4) magnetic nanoparticles," *Results in physics*, vol. 8, pp. 1046–1053, 2018. [Online]. Available: https://doi.org/10.1016/j.rinp.2018.01.045

[98] W. Wu, Q. He, and o. Chen, "Sonochemical synthesis, structure and magnetic properties of air-stable fe3o4/au nanoparticles," *Nanotechnology*, vol. 18, p. 145609, 2007. [Online]. Available: https://doi.org/10.1088/0957-4484/18/14/145609

[99] D. Langevin, "Micelles and microemulsions," *Annual Review of Physical Chemistry*, vol. 43, pp. 341–369, 1992. [Online]. Available: https://doi.org/10.1146/annurev.pc.43.100192.002013

[100] H. Zhang and G. Zhu, "One-step hydrothermal synthesis of magnetic fe3o4 nanoparticles immobilized on polyamide fabric," *Applied Surface Science*, vol. 258, pp. 4952–4959, 2012. [Online]. Available: https://doi.org/10.1016/j.apsusc.2012.01.127

[101] A. Hussain, T. Abbas, and S. B. Niazi, "Preparation of ni1- xmnxfe2o4 ferrites by sol–gel method and study of their cation distribution," *Ceramics International*, vol. 39, pp. 1221–1225, 2013. [Online]. Available: https://doi.org/10.1016/j.ceramint.2012.07.049

[102] L. Yao, Y. Xi, G. Xi, and Y. Feng, "Synthesis of cobalt ferrite with enhanced magnetostriction properties," *Journal of alloys and compounds*, vol. 680, pp. 73–79, 2016. [Online]. Available: https://doi.org/10.1016/j.jallcom.2016.04.092

[103] E. Manova, B. Kunev, and o. Paneva, "Mechano-synthesis, characterization, and magnetic properties of nanoparticles of cobalt ferrite, cofe2o4," *Chemistry of materials*, vol. 16, pp. 5689–5696, 2004. [Online]. Available: https://doi.org/10.1021/cm049189u

[104] M. Endo, K. Takeuchi *et al.*, "The production and structure of pyrolytic carbon nanotubes (pcnts)," *Journal of Physics and Chemistry of Solids*, vol. 54, pp. 1841–1848, 1993. [Online]. Available: https://doi.org/10.1016/0022-3697(93)90297-5

[105] Y. Flores-Arias *et al.*, "Magnetic phase transitions in ferrite nanoparticles characterized by electron spin resonance," *Journal of Applied Physics*, vol. 117, p. 17A503, 2015. [Online]. Available: https://doi.org/10.1063/1.4916935

[106] R. E. Hummel, "Fundamentals of thermal properties," in *Electronic Properties of Materials*. Springer, 2011, pp. 409–417. [Online]. Available: https://doi.org/10.1007/978-3-642-86538-1_19

[107] B. Cruz-Franco, T. Gaudisson, S. Ammar *et al.*, "Magnetic properties of nanostructured spinel ferrites," *IEEE transactions on magnetics*, vol. 50, pp. 1–6, 2014. [Online]. Available: https://doi.org/10.1109/TMAG.2013.2283875

[108] W. D. Callister Jr and D. G. Rethwisch, *Fundamentals of materials science and engineering: an integrated approach*. John Wiley and Sons, 2020. [Online]. Available: https://www.biblio.com/9781118061602

[109] D. S. Mathew and R.-S. Juang, "An overview of the structure and magnetism of spinel ferrite nanoparticles and their synthesis in microemulsions," *Chemical engineering journal*, vol. 129, pp. 51–65, 2007. [Online]. Available: https://doi.org/10.1016/j.cej.2006.11.001

[110] D. Jiles, "Recent advances and future directions in magnetic aterials," *Acta materialia*, vol. 51, pp. 5907–5939, 2003. [Online]. Available: https://doi.org/10.1016/j.actamat.2003.08.011

[111] D. L. Leslie-Pelecky and R. D. Rieke, "Magnetic properties of nanostructured materials," *Chemistry of materials*, vol. 8, pp. 1770–1783, 1996. [Online]. Available: https://doi.org/10.1021/cm960077f

[112] S. Kumar, R. R. Singh, and P. Barman, "Reitveld refinement and derivative spectroscopy of nanoparticles of soft ferrites (mgnife)," *Journal of Inorganic and Organometallic Polymers and Materials*, vol. 31, pp. 528–541, 2021. [Online]. Available: https://doi.org/10.1007/s10904-020-01764-7

[113] H. Jansen, G. Schneider, and H. Wang, "Calculation of magneto-crystalline anisotropy in transition metals," in *Electronic Structure and Magnetism of Complex Materials*. Springer, 2003, pp. 57–100. [Online]. Available: https://doi.org/10.1007/978-3-662-05310-2_2

[114] B. Hofmann and H. Kronmuller, "Stress-induced magnetic anisotropy in nanocrystalline fecunbsib alloy," *Journal of magnetism and magnetic materials*, vol. 152, pp. 91–98, 1996. [Online]. Available: https://doi.org/10.1016/0304-8853(95)00447-5

[115] V. S. Shinde, V. Vinayak, S. Jadhav, N. Shinde, A. V. Humbe, and K. Jadhav, "Structure, morphology, cation distribution and magnetic properties of cr 3+-substituted cofe 2 o 4 nanoparticles," *Journal of Superconductivity and Novel Magnetism*, vol. 32, pp. 945–955, 2019. [Online]. Available: https://doi.org/10.1007/s10948-018-4778-5

[116] H. Zhao, Z. Zheng, K. W. Wong, S. Wang, B. Huang, and D. Li, "Fabrication and electrochemical performance of nickel ferrite nanoparticles as anode material in lithium ion batteries," *Electrochemistry communications*, vol. 9, pp. 2606–2610, 2007. [Online]. Available: https://doi.org/10.1016/j.elecom.2007.08.007

[117] M. Banerjee, A. Mukherjee, S. Chakrabarty, S. Basu, and M. Pal, "Bismuth-doped nickel ferrite nanoparticles for room temperature memory devices," *ACS Applied Nano Materials*, vol. 2, pp. 7795–7802, 2019. [Online]. Available: https://doi.org/10.1021/acsanm.9b01828

[118] P. Kumar, R. Kumar, and H. N. Lee, "magnetic field induced one-dimensional nano micro structures growth on the surface of iron oxide thin film," *Thin Solid Films*, vol. 592, pp. 155–161, 2015. [Online]. Available: https://doi.org/10.1016/j.tsf.2015.08.047

[119] Y. Yang, M. C. Gupta *et al.*, "Novel carbon nanotube- polystyrene foam composites," *Nano letters*, vol. 5, pp. 2131–2134, 2005. [Online]. Available: https://doi.org/10.1021/nl051375r

[120] V. Zaspalis, V. Tsakaloudi *et al.*, "Development of a new mnzn-ferrite soft magnetic material for high temperature power applications," *Journal of Electroceramics*,

vol. 13, pp. 585–591, 2004. [Online]. Available: https://doi.org/10.1007/s10832-004-5162-3

[121] V. G. Harris, A. Geiler *et al.*, "Recent advances in processing and applications of microwave ferrites," *Journal of Magnetism and Magnetic Materials*, vol. 321, pp. 2035–2047, 2009. [Online]. Available: https://doi.org/10.1016/j.jmmm.2009.01.004

[122] Y. Aihara, J. Kuratomi, T. Bando, T. Iguchi, H. Yoshida, T. Ono, and K. Kuwana, "Investigation on solvent-free solid polymer electrolytes for advanced lithium batteries and their performance," *Journal of power sources*, vol. 114, pp. 96–104, 2003. [Online]. Available: https://doi.org/10.1016/S0378-7753(02)00529-3

[123] R. Dedryvere, D. Foix, S. Franger, S. Patoux, L. Daniel, and D. Gonbeau, "Electrode/electrolyte interface reactivity in high-voltage spinel limn1. 6ni0. 4o4/li4ti5o12 lithium-ion battery," *The Journal of Physical Chemistry C*, vol. 114, pp. 10 999–11 008, 2010. [Online]. Available: https://doi.org/10.1021/jp1026509

[124] L.-X. Yuan, Z.-H. Wang, W.-X. Zhang, X.-L. Hu, J.-T. Chen, Y.-H. Huang, and J. B. Goodenough, "Development and challenges of lifepo 4 cathode material for lithium-ion batteries," *Energy & Environmental Science*, vol. 4, pp. 269–284, 2011. [Online]. Available: https://doi.org/10.1039/C0EE00029A

[125] R. Fenner and E. Zdankiewicz, "Micromachined water vapor sensors - a review of sensing technologies," *IEEE Sensors Journal*, vol. 1, pp. 309–317, 2001. [Online]. Available: https://doi.org/10.1109/7361.983470

[126] C. G. Reddy, S. Manorama, and V. Rao, "Semiconducting gas sensor for chlorine based on inverse spinel nickel ferrite," *Sensors and Actuators B: Chemical*, vol. 55, pp. 90–95, 1999. [Online]. Available: https://doi.org/10.1016/S0925-4005(99)00112-4

[127] F. Kreitmeier, D. V. Chashin *et al.*, "Nonlinear magnetoelectric response of planar ferromagnetic-piezoelectric structures," *Sensors*, vol. 12, pp. 14 821–14 837, 2012. [Online]. Available: https://doi.org/10.3390/s121114821

[128] J. Giri, P. Pradhan, T. Sriharsha, and D. Bahadur, "Preparation and investigation of potentiality of different soft ferrites for hyperthermia applications," *Journal of Applied Physics*, vol. 97, p. 10Q916, 2005. [Online]. Available: https://doi.org/10.1063/1.1855131

[129] A. Jordan, R. Scholz *et al.*, "Presentation of a new magnetic field therapy system," *Journal of magnetism and magnetic materials*, vol. 225, pp. 118–126, 2001. [Online]. Available: https://doi.org/10.1016/S0304-8853(00)01239-7

[130] Y. K. Fetisov, A. A. Bush, K. E. Kamentsev, A. Y. Ostashchenko, and G. Srinivasan, "Ferrite-piezoelectric multilayers for magnetic field sensors," *IEEE Sensors Journal*, vol. 6, pp. 935–938, 2006. [Online]. Available: https://doi.org/10.1109/JSEN.2006.877989

[131] S. M. Ansari, B. B. Sinha *et al.*, "Particle size, morphology, and chemical composition," *ACS Applied Nano Materials*, vol. 2, pp. 1828–1843, 2019. [Online]. Available: https://doi.org/10.1021/acsanm.8b02009

[132] T. H. Chang, "Ferrite materials and applications," in *Electromagnetic Materials and Devices*. BoD–Books on Demand, 2020, p. 137. [Online]. Available: https://doi.org/10.5772/intechopen.84623

[133] P. R. Wilson, J. N. Ross, and A. D. Brown, "Modeling frequency-dependent losses in ferrite cores," *IEEE Transactions on Magnetics*, vol. 40, pp. 1537–1541, 2004. [Online]. Available: https://doi.org/10.1109/TMAG.2004.826910

[134] N.-S. Chen, X.-J. Yang, E.-S. Liu, and J.-L. Huang, "Reducing gas-sensing properties of ferrite compounds mfe2o4," *Sensors and Actuators B: Chemical*, vol. 66, pp. 178–180, 2000. [Online]. Available: https://doi.org/10.1016/S0925-4005(00)00368-3

[135] A. Kadu, S. Jagtap, and G. Chaudhari, "Studies on the preparation and ethanol gas sensing properties of spinel zn0. 6mn0. 4fe2o4 nanomaterials," *Current Applied Physics*, vol. 9, pp. 1246–1251, 2009. [Online]. Available: https://doi.org/10.1016/j.cap.2009.02.001

[136] R. Kotnala, J. Shah, B. Singh, S. Singh, S. Dhawan, A. Sengupta *et al.*, "Humidity response of li-substituted magnesium ferrite," *Sensors and Actuators B: Chemical*, vol. 129, pp. 909–914, 2008. [Online]. Available: https://doi.org/10.1016/j.snb.2007.10.002

[137] N. Rezlescu, E. Rezlescu, C. Doroftei, and P. Popa, "Study of some mg-based ferrites as humidity sensors," in *Journal of Physics: Conference Series*, vol. 15. IOP Publishing, 2005, p. 049. [Online]. Available: https://doi.org/10.1088/1742-6596/15/1/049

[138] A. B. Gadkari, T. J. Shinde, and P. N. Vasambekar, "Electrical and humidity sensing study of nanocrtsyallite mg-cd ferrites," *Sensors and Transducers*, vol. 137, p. 145, 2012. [Online]. Available: https://www.proquest.com/scholarly-journals/electrical-humidity-sensing-study-nanocrtsyallite/docview/931545911/se-2?accountid=136238

[139] M. D. Hernández-Alonso, F. Fresno, S. Suárez, and J. M. Coronado, "Development of alternative photocatalysts to tio 2: challenges and opportunities," *Energy & Environmental Science*, vol. 2, pp. 1231–1257, 2009. [Online]. Available: https://doi.org/10.1039/B907933E

[140] H. Dotan, A. Landman, S. W. Sheehan, K. D. Malviya, G. E. Shter, D. A. Grave, Z. Arzi, N. Yehudai, M. Halabi, N. Gal *et al.*, "Decoupled hydrogen and oxygen evolution by a two-step electrochemical–chemical cycle for efficient overall water splitting," *Nature Energy*, vol. 4, pp. 786–795, 2019. [Online]. Available: https://doi.org/10.1038/s41560-019-0462-7

[141] Y. Tamaura, N. Hasegawa, M. Kojima, Y. Ueda, H. Amano, and M. Tsuji, "Water splitting with the mn (ii)-ferrite–cao–h2o system at 1273k," *Energy*, vol. 23, pp. 879–886, 1998. [Online]. Available: https://doi.org/10.1016/S0360-5442(98)00030-9

[142] A. Steinfeld, P. Kuhn, A. Reller, R. Palumbo, J. Murray, and Y. Tamaura, "Solar-processed metals as clean energy carriers and water-splitters," *International Journal of Hydrogen Energy*, vol. 23, pp. 767–774, 1998. [Online]. Available: https://doi.org/10.1016/S0360-3199(97)00135-3

[143] D. Deng, H. Pang, J. Du, J. Deng, S. Li, J. Chen, and J. Zhang, "Fabrication of cobalt ferrite nanostructures and comparison of their electrochemical properties," *Crystal Research and Technology*, vol. 47, pp. 1032–1038, 2012. [Online]. Available: https://doi.org/10.1002/crat.201200161

[144] B. Sreedhar, A. S. Kumar, and D. Yada, "Cufe2o4 nanoparticles: a magnetically recoverable and reusable catalyst for the synthesis of 5-substituted 1h-tetrazoles," *Tetrahedron Letters*, vol. 52, pp. 3565–3569, 2011. [Online]. Available: https://doi.org/10.1016/j.cap.2009.02.001

[145] H. Yen, Y. Seo, R. Guillet-Nicolas, S. Kaliaguine, and F. Kleitz, "One-step-impregnation hard templating synthesis of high-surface-area nanostructured mixed metal oxides (nife 2 o 4, cufe 2 o 4 and cu/ceo 2)," *Chemical Communications*, vol. 47, pp. 10 473–10 475, 2011. [Online]. Available: https://doi.org/10.1039/c1cc13867g

[146] K. K. Kefeni and B. B. Mamba, "Photocatalytic application of spinel ferrite nanoparticles and nanocomposites in wastewater treatment," *Sustainable Materials and Technologies*, vol. 23, p. e00140, 2020. [Online]. Available: https://doi.org/10.1016/j.susmat.2019.e00140

[147] A. Elaissari, J. Chatterjee, M. Hamoudeh, and H. Fessi, "14 advances in the preparation and biomedical applications of magnetic colloids," *Structure and Functional Properties of Colloidal Systems*, vol. 146, p. 315, 2009. [Online]. Available: https://epdf.pub/colloidal-biomolecules-biomaterials-and-biomedical-applications.html

[148] L. Lenglet, P. Nikitin, and C. Péquignot, "Magnetic immunoassays: a new paradigm in poct," *IVD Technology, July/Aug*, pp. 43–49, 2008.

[149] F. Y. Gaffar and A. Koch, "Catch me if you can! rna silencing-based improvement of antiviral plant immunity," *Viruses*, vol. 11, p. 673, 2019. [Online]. Available: https://doi.org/10.3390/v11070673

[150] F. Panahi, F. Bahrami, and A. Khalafi-Nezhad, "Magnetic nanoparticles grafted l-carnosine dipeptide: remarkable catalytic activity in water at room temperature," *Journal of the Iranian Chemical Society*, vol. 14, pp. 2211–2220, 2017. [Online]. Available: https://doi.org/10.1007/s13738-017-1157-2

[151] T.-J. Yoon, W. Lee, Y.-S. Oh, and J.-K. Lee, "Magnetic nanoparticles as a catalyst vehicle for simple and easy recycling," *New Journal of Chemistry*, vol. 27, pp. 227–229, 2003. [Online]. Available: https://doi.org/10.1039/B209391J

[152] Q. Chen, P. Du, W. Huang, L. Jin, W. Weng, and G. Han, "Ferrite with extraordinary electric and dielectric properties prepared from self-combustion technique," *Applied physics letters*, vol. 90, p. 132907, 2007. [Online]. Available: https://doi.org/10.1063/1.2718482

[153] D. S. B. SHELKE, *EFFECT OF ISO AND ALIOVALENT SUBSTITUENTS ON THE PROPERTIES OF SPINEL FERRITE*.   BecomeShakespeare.com, 2021.

[154] H. Huili, B. Grindi, G. Viau, and L. B. Tahar, "Effect of cobalt substitution on the structure, electrical, and magnetic properties of nanorcrystalline ni0. 5zn0. 5fe2o4 prepared by the polyol process," *Ceramics International*, vol. 40, pp. 16 235–16 244, 2014. [Online]. Available: http://dx.doi.org/10.1007/s10971-011-2446-3

[155] K. Velmurugan, V. S. K. Venkatachalapathy, and S. Sendhilnathan, "Synthesis of nickel zinc iron nanoparticles by coprecipitation technique," *Materials Research*, vol. 13, pp. 299–303, 2010. [Online]. Available: https://doi.org/10.1590/S1516-14392010000300005

[156] Z. Beji, L. Smiri, N. Yaacoub, J.-M. Greneche, N. Menguy, S. Ammar, and F. Fiévet, "Annealing effect on the magnetic properties of polyol-made ni- zn ferrite nanoparticles," *Chemistry of materials*, vol. 22, pp. 1350–1366, 2010. [Online]. Available: https://doi.org/10.1021/cm901969c

[157] X. Shen, Y. Wang, X. Yang, L. Lu, and L. Huang, "0.3–3 ghz magneto-dielectric properties of nanostructured niznco ferrite from hydrothermal process," *Journal of Materials Science: Materials in Electronics*, vol. 21, pp. 630–634, 2010. [Online]. Available: http://dx.doi.org/10.1007/s10854-009-9968-2

[158] S. Komarneni, E. Fregeau, E. Breval, and R. Roy, "Hydrothermal preparation of ultrafine ferrites and their sintering," *Journal of the American Ceramic Society*, vol. 71, pp. C–26, 1988. [Online]. Available: https://doi.org/10.1111/j.1151-2916.1988.tb05773.x

[159] A. Ataie, M. Piramoon, I. Harris, and C. Ponton, "Effect of hydrothermal synthesis environment on the particle morphology, chemistry and magnetic properties of barium hexaferrite," *Journal of materials science*, vol. 30, pp. 5600–5606, 1995. [Online]. Available: https://doi.org/10.1007/BF00356692

[160] N. Chen and M. Gu, "Microstructure and microwave absorption properties of y-substituted ni-zn ferrites," *Open Journal of Metal*, vol. 2, pp. 37–41, 2012. [Online]. Available: http://dx.doi.org/10.4236/ojmetal.2012.22006

[161] G. Choudary, M. C. Varma, A. M. Kumar, K. Rao, and B. R. Kumar, "Enhancement of magnetic properties in cobalt substituted ni-zn nanoferrite system," in *AIP Conference Proceedings*, vol. 1347. American Institute of Physics, 2011, pp. 31–34. [Online]. Available: https://doi.org/10.1063/1.3601780

[162] S. B. Waje, M. Hashim, W. D. W. Yusoff, and Z. Abbas, "Room temperature measurements of physical and magnetic characteristics of," *Australian Journal of Basic and Applied Sciences*, vol. 3, pp. 2716–2723, 2009. [Online]. Available: http://www.ajbasweb.com/old/ajbas_july-september_2009.html

[163] A. R. West, *Solid state chemistry and its applications*. John Wiley and Sons, 2014. [Online]. Available: http://revistas.pucp.edu.pe/index.php/quimica/article/view/10414/10864

[164] R. Tholkappiyan and K. Vishista, "Influence of lanthanum on the optomagnetic properties of zinc ferrite prepared by combustion method," *Physica B: Condensed Matter*, vol. 448, pp. 177–183, 2014.

[165] N. Vasoya, L. Vanpariya, P. Sakariya, M. Timbadiya, T. Pathak, V. Lakhani, and K. Modi, "Synthesis of nanostructured material by mechanical milling and study on structural property modifications in ni0. 5zn0. 5fe2o4," *Ceramics International*, vol. 36, no. 3, pp. 947–954, 2010.

[166] A. Bajorek, C. Berger, M. Dulski, P. opadczak, M. Zubko, K. Prusik, M. Wojty-niak, A. Chrobak, F. Grasset, and N. Randrianantoandro, "Microstructural and magnetic characterization of ni0.5zn0.5fe2o4 ferrite nanoparticles," *Journal of Physics and Chemistry of Solids*, vol. 129, pp. 1–21, 2019.

[167] "Estimation and association of structural, elastic and magnetic properties of magnesium-nickel-ferrite," *Materials Science and Engineering: B*, vol. 272, p. 115362, 2021.

[168] M. Satalkar, S. Kane, A. Ghosh, and Franco, "Synthesis and soft magnetic properties of zn0. 8- xnixmg0. 1cu0. 1fe2o4 (x= 0.0- 0.8) ferrites prepared by sol–gel auto-combustion method," *Journal of alloys and compounds*, vol. 615, pp. S313–S316, 2014.

[169] M. Gabal, Y. Al Angari, and H. Zaki, "Structural, magnetic and electrical characterization of mg–ni nano-crystalline ferrites prepared through egg-white precursor," *Journal of magnetism and magnetic materials*, vol. 363, pp. 6–12, 2014. [Online]. Available: https://doi.org/10.1016/j.jmmm.2014.03.007

[170] T. R. Tatarchuk, N. D. Paliychuk, M. Bououdina *et al.*, "Effect of cobalt substitution on structural, elastic, magnetic and optical properties of zinc ferrite nanoparticles," *Journal of Alloys and Compounds*, vol. 731, pp. 1256–1266, 2018. [Online]. Available: https://doi.org/10.1016/j.jallcom.2017.10.103

[171] N. Ahmed, Khan *et al.*, "Influence of shape factor on flow of magneto-nanofluid squeezed between parallel disks," *Alexandria engineering journal*, vol. 57, no. 3, pp. 1893–1903, 2018.

[172] S. Mazen and N. Abu-Elsaad, "Ir spectra, elastic and dielectric properties of li–mn ferrite," *International Scholarly Research Notices*, vol. 2012, 2012. [Online]. Available: https://doi.org/10.5402/2012/907257

[173] G. Kumar, J. Shah, R. Kotnala, V. P. Singh *et al.*, "Superparamagnetic behaviour and evidence of weakening in super-exchange interactions with the substitution of gd3+ ions in the mg–mn nanoferrite matrix," *Materials Research Bulletin*, vol. 63, pp. 216–225, 2015. [Online]. Available: https://doi.org/10.1016/j.materresbull.2014.12.009

[174] S. Pugh, "Xcii. relations between the elastic moduli and the plastic properties of polycrystalline pure metals," *The London, Edinburgh, and Dublin Philosophical Magazine and Journal of Science*, vol. 45, pp. 823–843, 1954. [Online]. Available: https://doi.org/10.1080/14786440808520496

[175] K. Modi, U. Trivedi, P. Sharma, V. Lakhani, M. Chhantbar, and H. Joshi, "Study of elastic properties of fine particle copper-zinc ferrites through infrared spectroscopy," *Indian Journal of Pure and Applied Physics*, vol. 44, 2006. [Online]. Available: http://nopr.niscair.res.in/handle/123456789/8255

[176] E. Olsen and J. Thonstad, "Nickel ferrite as inert anodes in aluminium electrolysis: Part i material fabrication and preliminary testing," *Journal of Applied Electrochemistry*, vol. 29, pp. 293–299, 1999. [Online]. Available: https://doi.org/10.1023/A:1003460220418

[177] S. Gubbala, H. Nathani, K. Koizol, and R. Misra, "Magnetic properties of nanocrystalline ni–zn, zn–mn, and ni–mn ferrites synthesized by reverse micelle technique," *Physica B: Condensed Matter*, vol. 348, pp. 317–328, 2004. [Online]. Available: https://doi.org/10.1016/j.physb.2003.12.017

[178] B. P. Rao and K. Rao, "Initial permeability dependence on the microstructural and compositional changes in ni-zn-sc ferrites," *Le Journal de Physique IV*, pp. C1–239, 1997. [Online]. Available: https://doi.org/10.1051/jp4:1997191

[179] Z. Lazarevic, C. Jovalekic, A. Milutinovi *et al.*, "Preparation and characterization of nano ferrites." *Acta Physica Polonica, A.*, vol. 121, 2012. [Online]. Available: http://dx.doi.org/10.12693/APhysPolA.121.682

[180] T. Tatarchuk, M. Bououdina, N. Paliychuk *et al.*, "Structural characterization and antistructure modeling of cobalt-substituted zinc ferrites," *Journal of Alloys and Compounds*, vol. 694, pp. 777–791, 2017. [Online]. Available: https://doi.org/10.1016/j.jallcom.2016.10.067

[181] P. Sivakumar, R. Ramesh, A. Ramanand, S. Ponnusamy, and C. Muthamizhchelvan, "Synthesis and characterization of nickel ferrite magnetic nanoparticles," *Materials Research Bulletin*, vol. 46, pp. 2208–2211, 2011. [Online]. Available: https://doi.org/10.1016/j.materresbull.2011.09.009

[182] T. Vigneswari and P. Raji, "Structural and magnetic studies of magnesium substituted nickel ferrite nanoparticles by citrate precursor method," *Journal of Ceramic Processing Research*, vol. 17, pp. 999–1005, 2016. [Online]. Available: http://dx.doi.org/10.4028/www.scientific.net/AMR.938.128

[183] P. Chavan, L. Naik, P. Belavi, G. Chavan, C. Ramesha, and R. Kotnala, "Studies on electrical and magnetic properties of mg-substituted nickel ferrites," *Journal of Electronic Materials*, vol. 46, pp. 188–198, 2017. [Online]. Available: https://doi.org/10.1007/s11664-016-4886-6

[184] R. Gao, H. Zhang, and D. Yan, "Iron diselenide nanoplatelets: stable and efficient water-electrolysis catalysts," *Nano Energy*, vol. 31, pp. 90–95, 2017. [Online]. Available: https://doi.org/10.1016/j.nanoen.2016.11.021

[185] R. Gao and D. Yan, "Recent development of ni/fe-based micro/nanostructures toward photo/electrochemical water oxidation," *Advanced Energy Materials*, vol. 10, p. 1900954, 2020. [Online]. Available: https://doi.org/10.1002/aenm.201900954

[186] Y. Zhou, Y. Du, S. Xi, and Z. J. Xu, "Spinel manganese ferrites for oxygen electrocatalysis: effect of mn valency and occupation site," *Electrocatalysis*, vol. 9, pp. 287–292, 2018. [Online]. Available: https://doi.org/10.1007/s12678-017-0429-z

[187] M. Arif, G. Yasin, and o. Luo, "Hierarchical hollow nanotubes of nifev-layered double hydroxides," *Applied Catalysis B: Environmental*, vol. 265, p. 118559, 2020. [Online]. Available: https://doi.org/10.1016/j.apcatb.2019.118559

[188] M. Y. Lodhi, K. Mahmood *et al.*, "New mg0. 5coxzn0. 5- xfe2o4 nano-ferrites: structural elucidation and electromagnetic behavior evaluation," *Current Applied Physics*, vol. 14, pp. 716–720, 2014. [Online]. Available: https://doi.org/10.1016/j.cap.2014.02.021

[189] P. Hankare, S. Jadhav, U. Sankpal, S. Chavan, K. Waghmare, and B. Chougule, "Synthesis, characterization and effect of sintering temperature on magnetic properties of mgni ferrite prepared by co-precipitation method," *Journal of alloys and compounds*, vol. 475, pp. 926–929, 2009.

[190] H. Kumar, M. Kumar, P. Barman, and R. R. Singh, "Stable and luminescent wurtzite cds, zns and cds/zns core/shell quantum dots," *Applied Physics A*, vol. 117, pp. 1249–1258, 2014. [Online]. Available: https://doi.org/10.1007/s00339-014-8513-1

[191] M. George, S. S. Nair, A. M. John, P. Joy, and M. Anantharaman, "Structural, magnetic and electrical properties of the sol-gel prepared li0. 5fe2. 5o4 fine particles," *Journal of Physics D: Applied Physics*, vol. 39, p. 900, 2006. [Online]. Available: https://doi.org/10.1088/0022-3727/39/5/002

[192] A. Ahlawat, V. Sathe, V. Reddy, and A. Gupta, "Mossbauer, raman and x-ray diffraction studies of superparamagnetic nife2o4 nanoparticles," *Journal of Magnetism and Magnetic Materials*, vol. 323, pp. 2049–2054, 2011. [Online]. Available: https://doi.org/10.1016/j.jmmm.2011.03.017

[193] S. Prabahar and M. Dhanam, "Cds thin films from two different chemical bathsstructural and optical analysis," *Journal of Crystal growth*, vol. 285, pp. 41–48, 2005. [Online]. Available: https://doi.org/10.1016/j.jcrysgro.2005.08.008

[194] D. H. K. Reddy and Y.-S. Yun, "Spinel ferrite magnetic adsorbents: alternative future materials for water purification." *Coordination Chemistry Reviews*, vol. 315, pp. 90–111, 2016. [Online]. Available: https://doi.org/10.1016/j.ccr.2016.01.012

[195] A. Loganathan and K. Kumar, "Effects on structural, optical, and magnetic properties of pure and sr-substituted mgfe 2 o 4 nanoparticles at different calcination temperatures," *Applied Nanoscience*, vol. 6, pp. 629–639, 2016. [Online]. Available: https://doi.org/10.1007/s13204-015-0480-0

[196] S. Thakur, S. Katyal, A. Gupta, V. Reddy, and M. Singh, "Room temperature ferromagnetic ordering in indium substituted nano-nickel-zinc ferrite," *Journal of Applied Physics*, vol. 105, p. 07A521, 2009. [Online]. Available: https://doi.org/10.1063/1.3062956

[197] V. D'Ippolito, G. B. Andreozzi, D. Bersani, and P. P. Lottici, "Raman fingerprint of chromate, aluminate and ferrite spinels," *Journal of Raman Spectroscopy*, vol. 46, pp. 1255–1264, 2015. [Online]. Available: https://doi.org/10.1002/jrs.4764

[198] L. Neel, "Theorie du trainage magnetique de diffusion," *J. phys. radium*, vol. 13, pp. 249–264, 1952. [Online]. Available: https://dx.doi.org/10.1051/jphysrad:01952001305024900

[199] H. Moradmard and S. F. Shayesteh, "The variation of magnetic properties of nickel ferrite by annealing," *Manufacturing Science and Technology*, vol. 3, pp. 141–145, 2015. [Online]. Available: https://doi.org/10.13189/mst.2015.030411

[200] T. Pohlmann, P. Kuschel, J. Wollschlager, and K. Kupper, "Cation-and lattice-site-selective magnetic depth profiles of ultrathin fe 3 o 4 (001) films," *Physical Review B*, vol. 102, 2020.

[201] R. Waldron, "Infrared spectra of ferrites," *Physical review*, vol. 99, p. 1727, 1955. [Online]. Available: https://doi.org/10.1103/PhysRev.99.1727

[202] S. Munjal, N. Khare, C. Nehate, and V. Koul, "Water dispersible cofe2o4 nanoparticles with improved colloidal stability for biomedical applications," *Journal of Magnetism and Magnetic Materials*, vol. 404, pp. 166–169, 2016. [Online]. Available: https://doi.org/10.1016/j.jmmm.2015.12.017

[203] Y. Altin and A. Bedeloglu, "Nanomaterials with potential emi shielding properties," in *Materials for Potential EMI Shielding Applications*. Elsevier, 2020, pp. 179–199.

[204] P. Thakur, R. Sharma, M. Kumar, S. Katyal, N. Negi, N. Thakur, V. Sharma, and P. Sharma, "Superparamagnetic la doped mn–zn nano ferrites: dependence on

dopant content and crystallite size," *Materials Research Express*, vol. 3, p. 075001, 2016. [Online]. Available: https://doi.org/10.1088/2053-1591/3/7/075001

[205] J. Philip, G. Gnanaprakash, G. Panneerselvam, M. Antony, T. Jayakumar, and B. Raj, "Effect of thermal annealing under vacuum on the crystal structure, size, and magnetic properties of zn fe 2 o 4 nanoparticles," *Journal of Applied Physics*, vol. 102, p. 054305, 2007. [Online]. Available: https://doi.org/10.1063/1.2777168

[206] R. Rosnan, Z. Othaman, R. Hussin, A. A. Ati, A. Samavati, S. Dabagh, and S. Zare, "Effects of mg substitution on the structural and magnetic properties of co0. 5ni0. 5- x mg x fe2o4 nanoparticle ferrites," *Chinese Physics B*, vol. 25, p. 047501, 2016. [Online]. Available: https://doi.org/10.1088/1674-1056/25/4/047501

[207] S. Singh, N. Kumar, A. Jha, M. Sahni, R. Bhargava, A. Chawla, R. Chandra, S. Kumar, and S. Chaubey, "Effect of annealing temperature on the physical properties of zn-ferrite nanoparticles," *Journal of Superconductivity and Novel Magnetism*, vol. 27, pp. 821–826, 2014. [Online]. Available: https://doi.org/10.1007/s10948-013-2355-5

[208] R. Sharma, P. Thakur, P. Sharma, and V. Sharma, "Ferrimagnetic ni2+ doped mg-zn spinel ferrite nanoparticles for high density information storage," *Journal of Alloys and Compounds*, vol. 704, pp. 7–17, 2017. [Online]. Available: https://doi.org/10.1016/j.jallcom.2017.02.021

[209] D. Rawat, J. Sethi, S. Sahani, P. Barman, and R. R. Singh, "Pioneering and proficient magneto fluorescent nanostructures: Hard ferrite based hybrid structures," *Materials Science and Engineering: B*, vol. 265, p. 115017, 2021. [Online]. Available: https://doi.org/10.1016/j.mseb.2020.115017

[210] P. Chavan and L. Naik, "Investigation of energy band gap and conduction mechanism of magnesium substituted nickel ferrite nanoparticles," *physica status solidi (a)*, vol. 214, p. 1700077, 2017. [Online]. Available: https://doi.org/10.1002/pssa.201700077

[211] S. Chakrabarty, M. Pal, and A. Dutta, "Structural, optical and electrical properties of chemically derived nickel substituted zinc ferrite nanocrystals," *Materials Chemistry and Physics*, vol. 153, pp. 221–228, 2015. [Online]. Available: https://doi.org/10.1016/j.matchemphys.2015.01.006

[212] M. J. Iqbal and M. R. Siddiquah, "Structural, electrical and magnetic properties of zr–mg cobalt ferrite," *Journal of magnetism and magnetic materials*, vol. 320, pp. 845–850, 2008. [Online]. Available: https://doi.org/10.1016/j.jmmm.2007.09.009

[213] S. Joshi, M. Kumar, S. Chhoker, G. Srivastava, M. Jewariya, and V. Singh, "Structural, magnetic, dielectric and optical properties of nickel ferrite nanoparticles synthesized by co-precipitation method," *Journal of Molecular structure*, vol. 1076, pp. 55–62, 2014. [Online]. Available: https://doi.org/10.1016/j.molstruc.2014.07.048

[214] M. Amir, H. Gungunes, A. Baykal, and o. Almessiere, "Effect of annealing temperature on magnetic and mossbauer properties of znfe2o4 nanoparticles by sol-gel approach," *Journal of Superconductivity and Novel Magnetism*, vol. 31, pp. 3347–3356, 2018. [Online]. Available: https://doi.org/10.1016/j.molstruc.2014.07.048

[215] N. Sahu and S. Panigrahi, "Mathematical aspects of rietveld refinement and crystal structure studies on pbtio 3 ceramics," *Bulletin of Materials Science*, vol. 34, pp. 1495–1500, 2011.

[216] S. Patange, S. E. Shirsath, B. Toksha, S. S. Jadhav, S. Shukla, and K. Jadhav, "Cation distribution by rietveld, spectral and magnetic studies of chromium-substituted nickel ferrites," *Applied Physics A*, vol. 95, pp. 429–434, 2009. [Online]. Available: https://doi.org/10.1007/s00339-008-4897-0

[217] M. De and H. Tewari, "Structural characterization of mg substituted on a/b sites in nife 2 o 4 nanoparticles using autocombustion method," *Pramana*, vol. 89, pp. 1–4, 2017. [Online]. Available: https://doi.org/10.1007/s12043-017-1394-z

[218] O. N. Shebanova and P. Lazor, "Raman spectroscopic study of magnetite (fefe2o4): a new assignment for the vibrational spectrum," *Journal of Solid State Chemistry*, vol. 174, pp. 424–430, 2003. [Online]. Available: https://doi.org/10.1016/S0022-4596(03)00294-9

[219] V. Urbanova, M. Magro, A. Gedanken, D. Baratella, F. Vianello, and R. Zboril, "Nanocrystalline iron oxides, composites, and related materials as a platform for electrochemical, magnetic, and chemical biosensors," *Chemistry of Materials*, vol. 26, no. 23, pp. 6653–6673, 2014.

[220] R. Magisetty, A. Shukla, and B. Kandasubramanian, "Magnetodielectric microwave radiation, absorbent materials and their polymer composites," *Journal of Electronic Materials*, vol. 47, pp. 6335–6365, 2018. [Online]. Available: https://doi.org/10.1007/s11664-018-6580-3

[221] T. Sato, T. Maruo *et al.*, "Ionic liquids containing carbonate solvent as electrolytes for lithium ion cells," *Journal of Power Sources*, vol. 138, pp. 253–261, 2004. [Online]. Available: https://doi.org/10.1016/j.jpowsour.2004.06.027

[222] M. T. Yagub, T. K. Sen, S. Afroze, and H. M. Ang, "Dye and its removal from aqueous solution by adsorption: a review," *Advances in colloid and interface science*, vol. 209, pp. 172–184, 2014. [Online]. Available: https://doi.org/10.1016/j.cis.2014.04.002

[223] X. Meng, H. C. Seton, L. T. Lu, I. A. Prior, N. T. Thanh, and B. Song, "Magnetic copt nanoparticles as mri contrast agent for transplanted neural stem cells detection," *Nanoscale*, vol. 3, pp. 977–984, 2011. [Online]. Available: https://doi.org/10.1039/c0nr00846j

[224] B. Warren, "X-ray diffraction; courier corporation: 1969," *Google Scholar There is no corresponding record for this reference*, 2017.